ShawPittman

A Law Partnership Including Professional Corporations

PAUL A. GAUKLER
202.663.8304
paul.gaukler@shawpittman.com

January 3, 2001

By Electronic Filing and Mail Delivery

Emile L. Julian
Assistant for Rulemakings and Adjudications
Rulemakings and Adjudications Staff
Office of the Secretary of the Commission
U. S. Nuclear Regulatory Commission
11555 Rockville Pike, One White Flint North
Rockville, MD 20852-2738
Attn: Docketing & Services Branch

Re: Private Fuel Storage – Docket No. 72-22 – ASLBP No. 97-732-02

Dear Mr. Julian:

PFS is filing today Exhibit 2 to the Declaration of Dr. Kevin Coppersmith filed in support of Applicant's Motion for Summary Disposition of Utah Contention L. Exhibit 2 to Dr. Coppersmith's declaration is Volume 1, Final Report, Fault Evaluation Study and Seismic Hazard Assessment prepared by Geomatrix Consultants, Inc. for the Private Fuel Storage Facility, dated February 1999. In accordance with our earlier conversation with your office, we are enclosing two copies of the Geomatrix Report for the Secretary's office. Additionally, in accordance with the certificate of service filed with Applicant's Motion for Summary Disposition of Utah Contention L, we are providing copies of the Geomatrix Report to the three members of the Atomic Safety and Licensing Board and to lead counsel for the State and the NRC Staff.

If you have any questions, please contact me at (202) 663-8304.

Sincerely,

Paul Gaukler

Paul A. Gaukler

2300 N Street, NW Washington, DC 20037-1128   202.663.8000 Fax: 202.663.8007   *SECY-02*   www.shawpittman.com   Washington, DC
New York
London

ShawPittman

Emile L. Julian
January 3, 2001
Page 2

cc: G. Paul Bollwerk III, Esq. (By Hand Delivery)
        Dr. Jerry R. Kline (By Hand Delivery)
        Dr. Peter S. Lam (By Hand Delivery)
        Sherwin Turk, Esq. (By Hand Delivery)
        Denise Chancellor, Esq. (By Federal Express)
        Susan F. Shankman (without enclosure)
        Adjudicatory File, Atomic Safety and Licensing Board Panel (without enclosure)
        Diane Curran, Esq. (without enclosure)
        John Paul Kennedy, Esq. (without enclosure)
        Joro Walker, Esq. (without enclosure)
        Danny Quintana, Esq. (without enclosure)

EXHIBIT 2
COPPERSMITH DECLARATION

FINAL REPORT – VOLUME I of III

Fault Evaluation Study and Seismic Hazard Assessment

Private Fuel Storage Facility

Skull Valley, Utah

Prepared for:

Stone & Webster Engineering Corporation
P.O. Box 5406
Denver, Colorado 80217-5406

Prepared by:

Geomatrix Consultants, Inc.
100 Pine Street, 10th Floor
San Francisco, California 94111
(415) 434-9400

February 1999

Project No. 4790

Geomatrix Consultants

GEOMATRIX

FINAL REPORT – VOLUME I of III

Fault Evaluation Study and Seismic Hazard Assessment

Private Fuel Storage Facility

Skull Valley, Utah

Prepared for:

Stone & Webster Engineering Corporation
P.O. Box 5406
Denver, Colorado 80217-5406

Prepared by:

Geomatrix Consultants, Inc.
100 Pine Street, 10th Floor
San Francisco, California 94111
(415) 434-9400

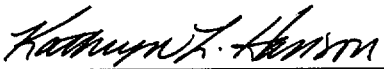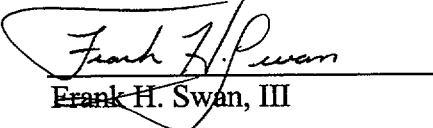February 1999

Project No. 4790

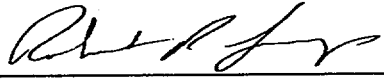**Geomatrix Consultants**

SWEC #0596602-18
GMX #4790 (REV. 0)

FAULT EVALUATION STUDY AND SEISMIC HAZARD ASSESSMENT
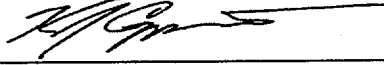
PRIVATE FUEL STORAGE FACILITY, SKULL VALLEY, UTAH

Prepared for:

Private Fuel Storage Facility
Private Fuel Storage, LLC

Prepared by: _Kathryn L. Hanson_   Date: _2/10/99_
Kathryn L. Hanson

Prepared by: _Frank H. Swan_   Date: _2/10/99_
Frank H. Swan, III

Prepared by: _Robert R. Youngs_   Date: _2/10/99_
Robert R. Youngs

Reviewed by: _Kevin J. Coppersmith_   Date: _2/10/99_
Kevin J. Coppersmith

Approved by: _Kevin J. Coppersmith_   Date: _2/10/99_
Kevin J. Coppersmith

Quality Assurance Category I
Geomatrix Consultants, Inc.
San Francisco, California

TABLE OF CONTENTS

TABLE OF CONTENTS
(Continued)

TABLES

FIGURES

PLATES

APPENDIXES

EXECUTIVE SUMMARY

This study was conducted to evaluate the potential for faults that could pose a fault-displacement and/or vibratory-ground-motion hazard at the proposed site for a Private Fuel Storage Facility (PFSF) in Skull Valley, Utah. This study was conducted for Stone and Webster Engineering Corporation under contract P.O. No. 0599602-018. In addition to review of existing literature, data and interpretations, and discussions with researchers familiar with the geology and neotectonic setting of the site region, extensive surface and subsurface investigations were completed for this study. Proprietary industry data, both gravity and seismic reflection data, were obtained and analyzed to constrain the locations of major faults in Skull Valley. Six kilometers of high-resolution seismic S-wave reflection data were collected to image reflectors in the upper part of the Tertiary and the overlying Quaternary section in the vicinity of the proposed storage area. Borings and trenches provided confirmation of the location and activity of faults identified from the seismic survey data. Geologic mapping investigations, including mapping of bedrock exposed in Hickman Hills, and mapping and surveying of Quaternary deposits and landforms in the site area and along the Stansbury fault zone to the east of the site provide additional data to evaluate the nature and timing of late Quaternary deformation in the site region. Based on the new data and results of these investigations, assessments are made of probabilistic vibratory ground motion and fault displacement hazard at the proposed PFSF site.

The proposed PFSF site is located in the approximate center of Skull Valley, a structural basin bounded on the west and east by the Cedar Mountains and Stansbury Mountains, respectively. The major structures in the region consist of pre-mid-Tertiary contractional structures that are no longer active, and which have been faulted and offset by younger post-mid-Tertiary normal faults and related extensional deformation. Three west-dipping normal faults and one east-dipping normal fault (East Cedar Mountains fault) are identified in the study area. The west-dipping faults include: (1) the Stansbury fault zone that lies 9 km east of the site along the western margin of the Stansbury Mountains; and (2) two unnamed faults in central Skull Valley that are informally referred to as the East and West faults. The latter two faults lie 0.9 km east and 2 km west of the site, respectively. The proposed storage area is located between the East and West faults in a postulated stepover zone characterized by secondary, distributed faulting. The Stansbury and the East and West faults are the most important structures with respect to the assessment of the potential for vibratory ground motion in the vicinity of the site.

The Stansbury fault is a major west-dipping normal fault that exhibits geomorphic evidence for late Quaternary activity. A cumulative late Quaternary slip rate of 0.39 ± 0.04 mm/yr is estimated for the Stansbury fault along the segment that lies closest to the proposed PFSF site. In this area, secondary traces in addition to the main trace have experienced multiple Pleistocene displacements. This slip rate value is faster than previously reported estimates, primarily because displacement across secondary traces was not included in previous estimates.

Alternate structural models that account for the observed style, location, and geometry of faulting within Skull Valley (mid-valley faults) are assessed. The mid-valley faults consist of the East fault, the West fault, and the postulated Springline fault in the northern part of Skull Valley. The East and West faults represent two strands of a fault system that extends northwest from The Dell, into Skull Valley basin. Seismic and gravity data indicate that these west-dipping faults form the eastern margin to an east-dipping, half-graben that underlies the central part of the Skull Valley Tertiary basin. These faults are not well exposed at the surface and have very subtle expression in the bedrock and surficial geology. Seismic reflection data north of the site indicate that the West fault lies within the basin and the East fault forms the basin-boundary fault along the eastern margin. South of the site, the West fault forms the eastern margin to the basin. Slip, therefore, is transferred from the East fault to the West fault in the vicinity of the site.

Evidence of late Pleistocene activity is indicated for the East and West faults. A preferred slip rate estimate of 0.2 ± 0.1 mm/yr is based on displacements across the East fault of three datums estimated to range in age from 12 ka to ≥ 160 ka. A slip rate of 0.05 to 0.07 mm/yr for the West fault is based on displacement of a single datum, the Stansbury bar, estimated to be 20 ka. This slip rate may be based on displacement during a single event.

Maximum magnitude for the Stansbury, East, and West faults are based on empirical relationships between magnitude and rupture length, magnitude and rupture area, magnitude and single event displacement and a relationship between magnitude, rupture length, and slip rate. The maximum magnitude distribution includes alternative maximum rupture scenarios for each fault. The mean maximum magnitudes for the three faults are: **M 6.5** for the East fault, **M 6.4** for the West fault, and **M 7.0** for the Stansbury fault.

Consistent with the requirements of Part 72, deterministic seismic hazard methodologies were used in the SAR to arrive at design basis ground motions. In light of recent changes to Part 100 (100.23) and anticipated changes to Part 72 (SECY-98-126), a probabilistic approach has been

implemented as part of this study. Probabilistic seismic hazard analyses were performed to evaluate the vibratory ground motion and fault displacement hazards at the proposed PFSF site. These analyses incorporate quantitatively the knowledge and uncertainties regarding seismic sources that might effect the site. The hazard results are in the form of hazard curves that express the annual probabilities or frequencies with which various levels of fault displacement and vibratory ground motion are expected to be exceeded in the proposed storage area. The activities performed to support these hazard analyses were: (1) evaluation and characterization of relevant seismic sources; (2) evaluation and characterization of vibratory ground motion attenuation, including earthquake source, wave propagation pate, and site effects; and (3) the performance of PSHAs for both fault displacement and vibratory ground motion. The hazard curves express the annual frequencies of exceedance for: (1) various amounts of fault displacement at three categories of locations within the proposed storage area; and (2) vibratory ground motion at two reference locations. A logic tree approach is used to represent uncertainties in various models and data sets incorporated into the assessment. The hazard results are presented as mean hazard curves that incorporate the uncertainty in input data and interpretations.

The seismic source model used in the probabilistic seismic hazard analysis includes 16 fault sources and four seismic source zones. Faults within 100 km of the proposed PFSF site that are judged to be capable of generating magnitude 5 or larger earthquakes and are inferred to have had multiple late Quaternary displacements were modeled as fault sources.

The probabilistic fault displacement hazard analysis is based on the methodology developed for the proposed Yucca Mountain repository. Hazards for three different categories of locations within the proposed storage area were calculated: (1) faults that appear to displace the Qp unconformity between the Promontory soil and the base of the Bonneville alloformation; (2) faults that appear to displace the unconformity at the top of the Tertiary Salt Lake Group (i.e., the Q/T unconformity) but do not extend to the Qp unconformity; and (3) zones between the mapped Quaternary faults that may experience distributed faulting and/or movements on faults too small to map.

The ground motion and fault displacement hazard analyses provide results for a range of probability levels. The selection of an appropriate probability level for the design of a dry cask storage system is based on a risk-informed graded approach, as supported by the NRC staff. Based on such an approach, we conclude that an appropriate design probability level for the proposed PFSF site is 5×10^{-4} per year (2,000-year return period). The design basis ground

motions presented in the SAR were based on a deterministic approach and did not incorporate the uncertainties associated with seismic sources and earthquake recurrence. The PSHA presented herein does include these uncertainties explicitly, including the findings of the fault studies. The deterministically defined design basis ground motions are compared with the 2,000-year ground motions derived from the probabilistic approach, and we conclude that the design basis ground motions in the SAR are conservative relative to this criterion. The design basis horizontal peak ground acceleration is 0.67 g compared to the 2,000-year return period peak acceleration of 0.5 g.

Because the consequences associated with the possible failure of the cask storage system due to fault displacement is comparable to that due to ground motions, the probability level of interest for fault displacement is also judged to be 5×10^{-4} per year (2,000-year return period). At these probability levels, the displacement associated with locations on Faults C, D, and F are less than 0.1 cm, and thus much lower than settlement displacements considered in the design.

FAULT EVALUATION STUDY AND SEISMIC HAZARD ASSESSMENT
Private Fuel Storage Facility
Skull Valley, Utah

1.0   INTRODUCTION

This report presents the results of investigations conducted to evaluate the potential for faults that could pose a fault-displacement and/or vibratory-ground-motion hazard at the proposed site for a Private Fuel Storage Facility (PFSF) in Skull Valley, Utah (Figure 1-1). This study was conducted for Stone & Webster Engineering Corporation (SWEC) under contract P. O No. 0599602-018.

The program provides further documentation and analysis to respond to questions/comments raised by the Nuclear Regulatory Commission (NRC) in their review of the Safety Analysis Report (SAR) submitted in April, 1998. (Request for Additional Information 2-5 and 2-7). In order to evaluate the significance of these findings to the seismic design basis, assessments are presented of the probabilistic vibratory ground motion and fault displacement hazard at the proposed facility based on the data and results of these investigations.

1.1   SCOPE

An eight-month program of field investigations and data analysis to evaluate the location and capability of faults at the proposed PFSF site was initiated in late May 1998. In addition to review of existing literature, data and interpretations, and discussions with researchers familiar with the geology and neotectonic setting of the site region, extensive surface and subsurface investigations were conducted. A compilation map at a scale of 1:12,000 showing the interpretation of identified bedrock faults, geologic contacts, landforms, and locations of geophysical surveys, drill holes, trenches, test pits, and topographic profiles is shown on Plate 1. The following sections describe the activities that were completed as part of this study.

1.1.1   Review of Existing Data/Discussions with Researchers

Professionals and researchers having knowledge of the region and data that pertain to the structural and stratigraphic setting of Skull Valley and the proposed PFSF site were contacted and interviewed during the initial stages of the project. Researchers contacted included: Drs. Robert B. Smith, Ronald Bruhn, and Walter Arabasz (Department of Geology and Geophysics, University of Utah); Ms. Jennifer M. Helm (currently employed by AGRA Earth & Environmental, Inc.); and Dr. J. Baer (Brigham Young University).

1.1.2   Structural Cross Sections

The structural geologic development of the study region was evaluated (Section 2.0). Construction of two cross sections, based on compilation and analysis of available geologic and geophysical data in the vicinity of Skull Valley provide constraints on the geometry and structural development of structures beneath Skull Valley in the site vicinity.

1.1.3   Aerial Photo Survey and Geologic Mapping

Figure 1-2 shows the extent and flight lines of 1:20,000-scale black and white aerial photographs obtained for this study. The Quaternary deposits and geomorphic features in the vicinity of the site were mapped based on photogeologic interpretation of aerial photographs and field checking (e.g., Figure 1-3). Descriptions of the Quaternary deposits and soil stratigraphy are provided in Section 3.0. A discussion of bedrock structure exposed at Hickman Knolls is provided in Section 4.0.

Photogeologic interpretation of 1:20,000 scale low-sun-angle black and white photos and reconnaissance field investigations along the southern segment of the Stansbury fault zone were conducted to evaluate the timing of most recent slip and major surface faulting earthquakes. The results of these investigations were used to modify the locations of active traces of the fault shown by Sack (1993) and Helm (1993). Field observations and data regarding the timing of recent surface faulting earthquakes along the Stansbury fault are provided in Section 5.1.

1.1.4   Geophysical Investigations

The following geophysical data and/or methods were used in this study.

- Gravity data previously collected by EDCON throughout most of Skull Valley in support of petroleum exploration efforts were obtained and analyzed. Proprietary data collected for 1033 gravity stations, spaced ¼ mile, along roads in Skull Valley were used to develop a detailed gravity contour map (Appendix E) and to provide input for gravity modeling to evaluate possible basin and fault geometries in the site vicinity.

- High resolution seismic shear wave reflection profiling. Six kilometers of high-resolution seismic S-wave reflection data were collected by Bay Geophysical Associates, Inc. (1999) along four profiles (Plate 1). Line A, which reoccupied and extended the P-wave seismic line 2 through the center of the proposed site area, extends from the center of Section 1, T5S, R9W to the eastern margin of Section 5, T5S, R8W. Line B, which was oriented perpendicular to the primary structural grain as inferred from the gravity data, extends from the center of the SW1/4 of Section 5, T5S, R8W through the western end of P-wave survey line 3 to the

western margin of Section 7, T5S, R8W. Lines C and D are east-trending lines that lie along the northern and southern boundaries, respectively of the proposed storage area. The survey was designed to image reflectors in the upper part of the Tertiary and the overlying Quaternary section. The survey parameters/methods, data processing, and interpretation of the S-wave data are described in a companion report (Bay Geophysical Associates, 1999).

- Reprocessing and interpretation of an industry P-wave reflection seismic data. A 23-km-(14.5-mi)-long east-west-trending P-wave reflection survey line, which was originally acquired for oil exploration by GSI, passes within one mile of the site. These data were purchased and reprocessed for this study. These data were used to help constrain the locations of post-Miocene faults within the basin. An interpretation of these proprietary data is provided in Bay Geophysical Associates (1999).

- Magnetometer Survey. 9.6 km (6 mi) of high-resolution magnetic data were collected in the site area: three lines, each 3.2 km (2 mi) in length were surveyed coincident with, and parallel to S-wave survey line A. The survey methods and results are described in Appendix A.

- Electrical conductivity tests were conducted at the site to evaluate the feasibility of using ground penetrating radar techniques to image subsurface stratigraphy (Appendix A). The conductivities of the soils ranged from about 50mS/m (sand bars) to over 400 mS/m (proposed storage site area). These conductivities are not favorable for obtaining high-resolution GPR data at depths where stratigraphy is old enough to be useful for evaluating fault capability. Therefore, additional GPR survey investigations were not pursued.

1.1.5 Drilling Program

Boreholes were drilled and logged to provide subsurface data to evaluate the continuity of key older marker horizons (e.g., pre-Bonneville lake cycle soils and deposits) across faults identified in the site area based on the geophysical surveys. The drilling program provided data to support the mapping investigations and selection of sites for detailed trenching investigations. Thirty holes were completed using a hollow stem auger and 5 ft continuous sampling device. Air rotary drilling was used in a few places where the hollow stem auger could not penetrate. To the extent possible, air rotary drilling was avoided because it does not provide a continuous sample. The holes were drilled to depths ranging from 8.2 to 27.1 m (27 to 89 ft). Logs of the auger holes are provided in Appendix B. Locations of the holes are shown on Plate 1.

1.1.6 Trenching Program

Twenty-five test pits and two longer (approximately 60 m (200 ft)) trenches were excavated to provide detailed information on the stratigraphy in the site area and to provide exposures across selected fault targets. Logs of the test pits and three hand-drilled auger holes are provided in Appendix C. Maps of the trench exposures are shown on Plates 2 and 3. The locations of the test pits and trenches are shown on Plate 1.

1.1.7 Geochronology Investigation

The assigned ages of the sediments and landforms in the site area are based primarily on geomorphic and stratigraphic relationships and correlation to the well-established lake chronology that has been developed for the Lake Bonneville basin region. Calcareous fossil material (ostracodes and charophytes) from deep-water sediments exposed in a test pit was collected and dated using radiocarbon analysis. This data provides local calibration to the Bonneville lake cycle stratigraphy and confirms the ages inferred for local stratigraphic units from geomorphic and stratigraphic correlations.

Four ash samples were collected from Salt Lake Group strata exposed in Trench 1. These samples were submitted to the University of Utah for microprobe analysis and correlation.

The results of the radiocarbon and tephra microprobe laboratory analyses are presented in Appendix D.

1.1.8 Seismicity Analysis

Seismicity data for the region was compiled and analyzed as part of the probabilistic seismic hazard analysis. Analysis of the earthquake catalog included: (1) reducing various measures of earthquake size to a uniform magnitude measure that is consistent with the ground motion attenuation relationships selected for characterizing ground motion at the site; and (2) determining the time period of complete reporting for various magnitude levels contained in the catalog. The analysis of the earthquake catalog is provided in Appendix F.

1.1.9 Seismic Hazard Analyses

Consistent with the requirements of Part 72, deterministic seismic hazard methodologies were used in the SAR to arrive at design basis ground motions. In light of recent changes to Part 100 (100.23) and anticipated changes to Part 72 (SECY-98-126), a probabilistic approach has been implemented as part of this study. Probabilistic seismic hazard analyses were performed to evaluate the fault displacement and vibratory ground motion hazards at the proposed PFSF site.

These analyses incorporate quantitatively the knowledge and uncertainties regarding seismic sources that might effect the site. The hazard results are in the form of hazard curves that express the annual probabilities or frequencies with which various levels of fault displacement and vibratory ground motion are expected to be exceeded in the proposed storage area. The PSHA results are compared to the ground motions based on a deterministic assessment.

1.2   ACKNOWLEDGEMENTS

2.0   STRUCTURAL GEOLOGIC SETTING OF SKULL VALLEY

The proposed PFSF site is located in the approximate center of Skull Valley, a structural basin bounded on the west and east by the Cedar Mountains and Stansbury Mountains, respectively (Figures 1-1, 2-1, and 2-2). The structural geologic setting of the proposed site is described in the following section, with emphasis on those features having an impact on seismic hazard at the site. The interpretations of regional faulting are shown on the compilation geologic map of Skull Valley (Plate 6) and two structural geologic cross sections that cross Skull Valley immediately north and south of the proposed site (Figures 2-1 and 2-2). The fault interpretations in map and section are based on previous geologic mapping, seismic-reflection and gravity data, and site investigations conducted as part of this study.

2.1   DATA SOURCES AND ANALYTICAL APPROACH

The structural cross-sections and map interpretations of fault geometry were prepared based on compilation and analysis of existing geologic map data, reprocessing and interpretation of a proprietary seismic reflection profile north of the site, and proprietary regional gravity data.

The cross sections extend for a total horizontal distance of about 50 km from the western Stansbury Mountains to the eastern margin of the Great Salt Lake Desert. The cross sections were drawn at 1:1 scale (no vertical exaggeration) and to depict subsurface structural relationships down to a total depth of about 15 km, which represents the approximate lower limit to most seismic activity in this region (Smith and Arabasz, 1991). The horizontal extent of the cross-sections was chosen to adequately encompass the potentially significant structures in the vicinity of the site.

The map data were transferred to the cross-sections using standard techniques described in Woodward and others (1989). Except where they follow existing lines by Rigby (1958) in the Stansbury Mountains, the cross section prepared for this study are oriented perpendicular to the strike of bedding and/or trends of major structural features to illustrate the geometry of faults and folds with a minimum of geometric distortion. The surface data from the Cedar Mountains and Stansbury Mountains were compiled on shallow cross-sections at the original map scales. Folds larger than several hundred meters in amplitude were identified and projected to 3-4 km depth using the kink-fold method of Suppe (1983). The shallow cross sections across the mountain ranges then were reduced to 1:100,000 scale and compiled on the regional sections. Structural features were extended from shallow depths (about 3-4 km) to the interpreted base of the seismogenic crust (about 15 km).

2.1.1 Geologic Map Data

The principal source of regional bedrock map data is the geologic map of the Tooele 1° x 2° Quadrangle (1:250,000) by Moore and Sorenson (1979). The cross sections were prepared at a scale of 1:100,000. Previously published map data at larger scales from the Cedar Mountains and Stansbury Mountains that were evaluated and incorporated in the cross sections include stratigraphic and structural geologic data from Maurer (1970) and Rigby (1958). Additional geologic data reviewed and considered includes mapping of the northern Stansbury Mountains and northeastern Skull Valley by Helm (1995), reconnaissance mapping and structural interpretation of the Stansbury Mountains by Tooker and Roberts (1971), as well as field investigations performed for this study.

2.1.2 Seismic Reflection Data

A seismic reflection profile located north of the site (Line GSI-UT-34) that was originally gathered for hydrocarbon exploration was purchased from a geophysical data broker and reprocessed for this study. This line trends east-west and is located Approximately 600 m north of the site (Plate 1). The reprocessed version of the line available for this study is a migrated time section and is included in Bay Geophysical Associates (1999).

2.1.3 Gravity Data

Proprietary gravity data from Skull Valley were used in this study. The data consist of complete Bouguer anomaly values at a series of discrete measurement stations in Skull Valley, as well as derivative maps and 2D profiles of the regional Bouguer gravity field generated from this data set. Both direct gravity measurements along approximately east-west-trending traverses and gravity profiles derived from the interpolated regional map were analyzed to provide constraints on subsurface structure in Skull Valley. A subset of the contoured gravity data showing the most prominent low, high, and steep-gradient anomalies is presented on Plate 6. These data are used to help constrain the map geometry of faulting in Skull Valley.

In addition to the proprietary data, published gravity data examined for this study include maps by Cook and others (1975; simple Bouguer anomaly map of Utah, 1:1,000,000), and Cook and others (1989; complete Bouguer anomaly map of Utah, 1:500,000). There is a pronounced 20-30 mgal gravity low in central and western Skull Valley that represents a significant departure from a smooth regional gradient along the lines of the cross-sections (Figures 2-1 and 2-2). This anomaly results from the presence of a relatively lower density body at depth, which is interpreted as Tertiary alluvium overlying the Paleozoic bedrock. This gravity low therefore represents sedimentary fill within a Tertiary basin.

The gravity data also are used to constrain the geometry of the Tertiary basin in cross section. Gravity profiles along the lines of the cross-sections were derived from the latter map and are shown at 1:100,000 scale on the cross-sections. The proprietary gravity data were modeled using Macintosh-based software called Grav2D. The software incorporates standard 2-D gravity modeling theory and approaches (e.g., Dobrin, 1976). The reduced gravity data were evaluated by drawing 2-D bodies of various shapes and densities in the subsurface along the profile, then calculating the predicted gravity for a given model. The predicted gravity values can be compared to the observed values to test the model.

The density contrast between this lower density body and surrounding rocks can be estimated by evaluating acoustic velocities used to stack and migrate the industry seismic reflection profile that crosses the gravity low. Shallow rocks in the upper 1.5 second depth twt (two-way time) located east of the gravity low exhibit average seismic velocities of about 4250 m/s. To the west, rocks in the same depth range within the gravity low exhibit average seismic velocities of about 2100 m/s. Using an empirical relation between seismic velocity and rock density, (Ludwig and others, 1970), the density contrast associated with the different seismic velocities is about 0.4 gm/cm^3. This value is consistent with estimates of the density contrast between bedrock and alluvium in Skull Valley used by previous workers (i.e., 0.4-0.5 gm/cm3; Johnson and Cook, 1957; Zoback, 1983).

We modeled the low gravity anomaly in central and western Skull Valley by finding the shape of a body of alluvium with a density contrast of -0.4 gm/cm3 that best reproduces the observed gravity low. The only free parameter in the model is the 2-D shape of the low density body in cross-section, which we interpret to be a wedge of alluvium overlying the bedrock in Skull Valley. The modeled shape and dimensions of this wedge of alluvium were incorporated into the cross sections.

Given the gravity low anomaly indicates the general shape of the Tertiary basin, these data are used to infer the location of faults related to basin development along strike to the north and south of the east-west cross section. We observe a direct correlation between faults within Skull Valley and adjacent gravity highs and lows. This relationship is observed across the postulated Springline fault on the east side of the valley and the East Cedar Mountains fault on the west. In addition, the steep gradient southwest of the gravity high associated with Lone Rock at the north end of the valley lies along the projected trend of a series of northwest-trending faults that splay off the Stansbury fault south of Lone Rock (Plate 6). The relationship

also is apparent from correlation of the Tertiary basin and related bounding faults to the east interpreted from the seismic reflection data and the 2D gravity modeling.

2.2 STRUCTURAL DEVELOPMENT OF THE STUDY REGION

Based on analysis of available map and geophysical data, the major structural features in the study region consist of a series of older folds and thrust faults that have been deformed by younger Tertiary normal faulting and crustal extension.

The Stansbury Mountains and Cedar Mountains are faulted anticlinoria that probably accommodated significant regional crustal shortening during the Mesozoic and early Tertiary Sevier-Laramide orogenies (Maurer, 1970). Rigby's (1958) cross-sections through the Stansbury Mountains clearly show that the range is coincident with the axis of an asymmetric fold called the "Deseret anticline" by previous workers (see discussion in Rigby 1958 for summary). This anticlinorium reaches a maximum structural relief at the latitude of the Skull Valley Indian Reservation and plunges to the south and north for a total length of about 40 km. The Cedar Mountains is an east-vergent anticline or anticlinorium whose axis is near the center of the range (Maurer, 1970). The west and east limbs of the Cedar Mountains anticline are cut by thrust and reverse faults that repeat parts of the Paleozoic section (Maurer, 1970; Moore and Sorenson, 1979).

The contractional structures in the Cedar Mountains and Stansbury Mountains are unconformably overlain by mid- to late-Tertiary volcanic rocks (Maurer, 1970; Rigby, 1958; Helm, 1995), consistent with the interpretation that they probably are associated with the Sevier-Laramide deformation (Maurer, 1970). In addition to the Mesozoic-early Tertiary phase of crustal shortening, stratigraphic and structural relations in the Stansbury Mountains indicate that this region probably was subjected to one or more Paleozoic phases of uplift and folding. In particular, there is a Devonian-Mississippian angular unconformity in strata on the eastern flank of Stansbury Mountains, and a probable mid-Carboniferous angular unconformity exposed farther east (Rigby, 1958). The earlier of these two unconformities may be temporally related to the Antler orogeny.

The large-scale contractional structures in the Stansbury Mountains have been faulted and offset by Tertiary and Quaternary normal faults. The best mapped and best understood of these structures is the Quaternary-active Stansbury fault zone (Rigby, 1958; Helm, 1995), which forms the major escarpment along the western margin of the Stansbury Mountains. Workers have proposed that Tertiary normal faults also are present in Skull Valley west of the Stansbury

fault based on the presence of bedrock outcrops (Helm 1995) and gravity data (Cook and others 1989; Zoback 1983). These structures include the postulated Springline fault west of Salt Mountain (Helm 1995), north of the study site.

2.3   MAJOR STRUCTURES DEPICTED IN THE CROSS SECTIONS

The major structures depicted on the cross sections are described in the following section. These consist of pre-mid-Tertiary contractional structures that are no longer active, and which have been faulted and offset by younger post-mid-Tertiary normal faults and related extensional deformation.

2.3.1   Older Contractional Structures

The major anticlines or anticlinoria exposed in the Cedar Mountains and Stansbury Mountains are reasonably well constrained by outcrop patterns of folded Paleozoic units (Figure 1-1); however, the available structural data are too sparse to permit detailed reconstructions of the fold profiles.

The Cedar Mountains anticline is generally broad, open, and both limbs are cut by reverse faults that dip away from the axis of the fold. Distinct asymmetry of the fold is not apparent at the latitude of the cross-sections, but cross-sections constructed by Maurer (1970) from areas to the north of the section lines suggest the fold is moderately asymmetric and vergent to the east.

The Deseret anticline in the Stansbury Mountains is interpreted to be an east-vergent fault-propagation fold that is underlain by a blind, west-dipping thrust fault, here named the "Deseret anticline thrust fault". Based on analogues from other thrust belts, and from bedding dips on the western limb of the Deseret anticline, we assume that the dip of the thrust fault is about 20°-30° to the west.

Mapping by Rigby (1958) and Moore and Sorenson (1981) indicates that an east-vergent thrust fault is present along the eastern margin of the Stansbury Mountains at the latitude of section A-A' (Figure 2-1). This thrust fault mapped at the surface is the up-dip continuation of the blind Deseret anticline thrust inferred to underlie the Stansbury Mountains to the south at the latitude of section B-B' (Figure 2-2). This interpretation is consistent with cross-sections by Rigby (1958), which show that the maximum structural relief on the Deseret anticline, and hence probably the maximum throw on the underlying thrust fault, occurs at about the latitude of section A-A'.

2.3.2 YOUNGER EXTENSIONAL STRUCTURES

The cross-sections depict three west-dipping normal faults and one east-dipping normal fault (East Cedar Mountains fault) in the study area. The west dipping faults include: (1) the Stansbury fault zone along the western margin of the Stansbury Mountains; and (2) two unnamed faults in central Skull Valley. For convenience, we refer to these latter structures as the East and West faults. The Stansbury and the East and West faults are the most important structures with respect to the assessment of the potential for fault rupture in the vicinity of the site.

The Stansbury fault zone is a west-dipping normal fault (Rigby, 1958) that exhibits strong geomorphic evidence for late Quaternary activity (Helm 1995). Because no direct measurements of the dip of the fault are available at the latitude of the cross-sections, we assume a 55° dip for the fault, consistent with the dip of the fault that produced the 1983 Borah Peak normal-faulting earthquake in Idaho (Smith and Arabasz, 1991). Based on very short trace lengths, limited map extent and close spatial relationship to the Stansbury fault, we interpret that the two splays of the fault mapped at the latitude of cross-section B-B' merge down dip into a single fault or fault zone. Based on the geometry of the Deseret anticline and our interpretation of the geometry of the underlying blind thrust fault, we see no compelling reason to assume that the Stansbury fault merges downdip with the thrust fault, as proposed elsewhere in the Basin and Range province (Mohapatra and Johnson, 1998). We conclude that the Stansbury fault probably extends as a planar or subplanar structure to the base of the seismogenic crust, and does not significantly interact with older thrust faults that may be present at depth. The late Quaternary activity of the Stansbury fault is discussed in Section 5.1.

Unlike the Stansbury fault, the East and West faults are not readily apparent in the geomorphology. The main surface evidence of the fault are the outliers of bedrock at Hickman Knolls and Castle Rock that lie to the east (in the uplifted footwall) of the West and East faults, respectively (Plate 6, Figures 2-1 and 2-2). The locations of the faults and their map geometry are inferred primarily from analysis of seismic reflection and gravity data. The location and dip of the faults on the reprocessed industry seismic line is inferred primarily from the geometry of layered basin sediments imaged beneath Skull Valley, from the lateral terminations and offset of these reflectors (Figure D-1 in Bay Geophysical Associates, 1999) and by analogy to other faults in the Basin and Range.

East Fault

The easternmost indication of faulting within Skull Valley, west of the Stansbury fault, is

associated with the eastern margin of the Tertiary basin interpreted from the geophysical data (regional and local seismic profiles, gravity). The East fault is recognized on the regional seismic profile (Line GSI-UT-34, Figure D-1 in Bay Geophysical Associates, 1999) as a west-dipping zone of abrupt reflector terminations between about shotpoints 183 and 260. In the deeper section, a strong set of coherent, east-dipping reflectors (~ 1.2 – 1.6 twtt) end abruptly to the east beneath about shotpoint 260. The eastward terminations can be traced upward into the shallow section to the east.

In the upper part of the imaged section, the eastward termination of strongly reflective layers above about 0.6 sec twtt projects to the ground surface at about shotpoint 193. A second fault is interpreted 450m to the east at shotpoint 183. These shallow reflectors are interpreted as representing Paleozoic strata and are correlated to the deep prominent reflectors at 1.2 to 1.6 sec twtt. We interpret the structures at shotpoints 193 and 183 to represent the bounding faults to a single fault zone that forms the eastern margin to the Tertiary basin in Skull Valley (Figure 2-1).

The zone of faulting at the east end of seismic line 34 (East Fault) is correlated to a zone of down-on-the-west faulting of similar width located at the eastern end of high-resolution seismic profile Line PFSF-98-A, between shotpoint 946 and the end of the line (Section 5.2 and Figure D-1 in Bay Geophysical Associates, 1999). The fault zone on Line A is located about 3500 ft (1000 m) southeast of the east fault on Line 34, along the trend of the steep gravity gradient interpreted as the eastern margin of the Tertiary basin.

The East fault as defined by the geophysical data in the site vicinity is not well expressed in the surface geology. There is an alignment of en echelon parallel stream drainages extending north and south of the two seismic profiles (Plate 6). This geomorphic expression dies out to the south abruptly, near the northern limit of bedrock outcrop at Hickman Knolls. The East fault is projected to the north along the trend of several linear drainages and the gravity gradient, both of which swing to a northerly trend west of Castle Rock (Plate 6).

The location of East fault north of the site also is constrained by the north-northwest trending linear fault line scarp (?) in alluvial deposits south of Castle Rock. Evidence pertaining to the amount and timing of Quaternary displacement on the East Fault is described in Section 5.2.

Based on the northward continuation of the steep gravity gradient and north-trending linear drainages, we interpret that the East fault likely extends north of Castle Rock at least as far as

the east-west-trending Pass Canyon structure. The exact location of intersection between the East fault and Pass Canyon structure is uncertain. It appears to lie from 2.4 to 4.6 km east of the southern tip of the postulated Springline fault as defined by Helms (1993). The similar geometry between the Stansbury and East faults and similar apparent eastward offset of faulting north of the Pass Canyon structure suggests the East fault may connect with the postulated Springline fault.

There are fewer data that constrain the location of the East fault southeast of Hickman Knolls. The weaker geomorphic expression to the southeast also is reflected in the shallowing of the steep gravity gradient. The gravity low that lies to the west continues to the southeast, but the anomalous low is less intense and the adjacent high to the east is characterized by irregular, lobe-shaped gravity high promontories and intervening gravity low gradients.

Following the general trend of the gravity gradient to the southeast, the East fault projects toward a zone of northwest-southeast-trending faults in bedrock in the northern Onaqui Mountains. The bedrock faults follow a deeply incised northwest-trending linear bedrock valley that enters Skull Valley at the northern end of a large outlier of bedrock named "the Dell." Based on these observations and interpretations of mid-valley faulting in Skull Valley, the East fault forms the principal bounding fault to the buried Tertiary basin within Skull Valley, extending from Pass Canyon Structure in the north to "The Dell" at the range front of the Onaqui mountains in the south (Figures 2-1 and 2-2; Plate 6).

West Fault
The West fault is the westernmost, major west-dipping fault recognized on seismic line GSI-UT-34 (Figure D-1 in Bay Geophysical Associates, 1999). This fault displaces the prominent reflectors at the base of the layered sequence with a down-on-the-west sense of offset. These reflectors are interpreted as Paleozoic sedimentary bedrock. South of line GSI-UT-34, the West fault is inferred to lie west of the outcrop of Paleozoic bedrock at Hill 4642 (Plates 1 and 6; Figure 2-2). South of Hill 4642, the location of the West fault is inferred primarily from the proprietary gravity data (Appendix E). Our interpretation is based on the observation that faults within the valley west of the Stansbury range separate gravity highs on the east from gravity lows on the west. This relationship is observed across the postulated Springline fault north of Pass Canyon, along the East fault in the vicinity of the site, and along the northwest-trending fault southwest of Lone Rock, at the north end of Skull Valley (Plate 6). Based on this relationship, we infer the eastern margin of the Tertiary basin likely consists of one or more

discontinuous and/or weakly developed faults that bound the two lobate gravity highs between Hickman Knolls and the range front at the Dell.

There is little evidence for continuation of the West fault north of line GSI-UT-34. Sack (1993) maps a series of northwest-trending lineaments immediately north of line GSI-UT-34, within Quaternary deposits of Skull Valley. Most are parallel beach ridges associated with Lake Bonneville. The southernmost of the features, however, appears as a strong tonal contract/linear depression that seems to cut across the topographic contours. North of this lineament there is no evidence in the bedrock geology, the surficial geology, or geomorphology for the northwest continuation of the West fault. The northern limit of the possible fault-related lineament is coincident with northern closure of the Tertiary basin as defined by the gravity data. Additionally, there is no evidence for a continuation of northwest-trending structures within bedrock in the East Cedar Mountains along the projection of the West fault. We infer that the West fault dies out north of line GSI-UT-34 in the vicinity of the lineaments mapped by Sack (1995).

Offset of the West fault increases to the south, as indicated by the increasing intensity of the gravity low anomaly and northwest-trending gravity gradient associated with the Tertiary basin. A southward increase in offset on the West fault also is indicated by the presence of Paleozoic bedrock outcrop west of Hickman Knolls. There also is an increase in northwest-trending lineaments in both bedrock and Quaternary deposits/landforms in the vicinity of Hickman Knolls and to the southeast (Plate 6). Based on the gravity data, we interpret that the West fault rotates to a more westerly trend south of Hickman Knolls, following the trend of gravity contours. This interpretation places the West fault between the gravity high "promontory" southeast of Hickman Knolls and the gravity low "embayment" immediately to the south. The southern projection of the West fault intersects the East fault in the vicinity of Johnson Pass, and the combined East/West faults extend southeast as a single structure to the bedrock fault at the Dell (Plate 6). Based on similar reasoning, we also interpret that a fault lies between the second gravity-high lobe to the southeast and the gravity low south of the high (Plate 6). The location of this fault is poorly constrained; it is inferred to have a geometry similar to the southern section of the West fault.

Fault "F"

The prominent shallow reflectors that lie west of the East fault on seismic line GSI-UT-34 are terminated to the west against a west-dipping normal fault (Fault "F") that projects to the ground surface near shotpoint 227 (Figure D-1 in Bay Geophysical Associates, 1999). We

interpret from the seismic profile that Fault F merges down-dip with the East Fault at a depth of about 0.9 – 1.0 sec twtt.

Fault F is correlated south from line GSI-UT-34 to a 200m-wide zone of predominantly down-on-the-west faults between shot points 3138 and 3329 on high-resolution seismic reflection line A (i.e., profile PFSF-98-A) west of the site (Plate 1). Fault F is also recognized at the west end of line D (profile PFSF-98-D), between shot points 197 and 369, and is extended south through a zone of faults that offset the Stansbury bar 300m north of bedrock outcrop at Hickman Knolls (Plate 1). Two north-trending linear outcrops of silicified reddish-brown dolomite breccia occur along the western margin of Hickman Knolls. The outcrops contain a strong N05°-10W°-trending planar shear fabric that dips steeply (~ 75°) to the west. Asymmetric shearing and offset of silicified (chert?) clasts indicate a component of right- lateral displacement during early brittle ductile transitional faulting.

Fault F is not identified north of line GSI-UT-34. However, the change in trend of the East Fault near Castle Rock lies near the northern projection of Fault F. Based on this projected trend, and on the observation that Fault F decreases in displacement to the south, we infer that Fault F splays south from the East Fault at the change in trend near Castle Rock and dies out at southward in the vicinity of Hickman Knolls. The nature and timing of the Quaternary displacement on fault F is described in Section 5.2.

2.4   STRUCTURAL MODEL

A structural model that accounts for the observed style, location and geometry of faulting within Skull Valley (mid-valley faults) is described to support analysis of fault-related hazard. The mid-valley faults consist of the postulated Springline fault, the East fault and the West fault. The East and West faults represent two strands of a fault system that extends northwest from The Dell, into Skull Valley basin. Seismic and gravity data indicate these faults form the eastern margin to an east-dipping, half-graben Tertiary basin that underlies the central part of Skull Valley and that has very subtle expression in the bedrock and surficial geology. Seismic reflection data north of the site indicate that the West fault lies within the basin and the East fault forms the basin-boundary fault along the eastern margin. South of the site, the West fault forms the eastern margin to the basin. Some or all of the slip therefore, is transferred from the East fault to the West fault in the vicinity of the site.

Additionally, the geologic expression of the East fault and the gravity gradient associated with it decrease south from the site, suggesting that the displacement also decreases to the south

(Plates 1 and 6). A northward increase in displacement on the East fault is inferred from a stronger geomorphic expression in the drainage pattern, geologic expression along the escarpment south of Castle Rock, and the northward continuation of the gravity gradient. In contrast, geologic and geophysical evidence suggests the West fault dies out abruptly north of the site, and persists south of the site as the east margin to the Tertiary basin.

These observations suggest there is a right stepover or "bridge" structure between the East and West faults at the latitude of the site. The stepover is the surface expression of a structural link at depth between the East and West faults across which fault displacement is transferred from one fault to the other. This model is consistent with the observations of no major faulting within the stepover region. The stepover is characterized by a zone of low-displacement faults that are discontinuous along-strike.

3.0   SITE STRATIGRAPHY

The stratigraphy in the vicinity of the proposed PFSF consists of an approximately 150 to 250 m (500 to 800 ft)-thick section of Quaternary and Tertiary basin fill overlying Paleozoic bedrock (Figure 3-1). The Quaternary section consists of a sequence of primarily lacustrine deposits representing a series of pluvial lake cycles with intertonguing subaerial sediments. Correlation of these deposits to a well established regional pluvial chronostratigraphy provides well-constrained age estimates for late Quaternary deposits at the site. In general, the Quaternary section thickens to the north with increasing distance from Hickman Knolls. At the proposed storage area, Quaternary deposits are approximately 85 ft (26 m) thick. The Quaternary sediments overlie Tertiary basin fill deposits that consist of an interbedded sequence of siltstone, claystone, and tuffaceous sediments. The upper part of the Tertiary basin fill is middle to late Miocene (approximately 6 Ma).

3.1   REGIONAL PLUVIAL CHRONOSEQUENCE

There have been four major lake cycles during the past 700,000 years in the Bonneville basin region (Figure 3-2). Evidence of these lake cycles has been documented based on outcrop data (see summary in Machette and Scott, 1988) and from cores from the floor of the Bonneville basin (Oviatt and others, 1997). The term "Lake Bonneville" is used to refer to the most recent major late Pleistocene lake in the Bonneville basin, which existed between about 28 and 12 ka (Oviatt and others, 1992; Oviatt, 1997). Numerous studies throughout the basin have resulted in a geochronometrically well-constrained reconstruction of the fluctuations in lake level that occurred during this lake cycle (Figure 3-3). The history of earlier lake cycles is less well known because the older lake deposits have been largely obliterated by erosion or buried by younger lake deposits and alluvium.

As illustrated in Figure 3-3, several major stillstands represented by distinctive shorelines and facies changes in the lacustrine deposits are recognized within the Lake Bonneville lacustrine cycle. The general elevations and ages of these shorelines are given in the Table 3-1. A Quaternary map of Skull Valley showing the general distribution of Quaternary deposits and shoreline features at a scale of 1:100,000 is provided by Sack (1993) (Plate 6).

Two of these shorelines, the Stansbury and Provo shorelines, are present within the site area. Several prominent geomorphic features within the site area relate to the Stansbury shoreline as discussed below. On Hickman Knolls, the Provo shoreline is evidenced by prominent tufa deposits at an elevation of 1473 m (4830 ft) and an erosional platform at approximately 1479 m

(4850 ft). Sack (1993) maps the Provo shoreline at an approximate altitude of 1493 m (4900 ft) on the piedmont east of the site, but review of aerial photographs for this study suggest that it is at a lower elevation (1482 m ± 2 [4860 ft ± 5]) close to or slightly above the elevation observed on Hickman Knolls. The Bonneville shoreline, which marks the highest strandline of the Bonneville lacustral cycle, lies approximately 8 km (5 mi) east of the site in the upper piedmont west of the Stansbury fault at an elevation 1598 m (5240 ft) (Sack, 1993).

3.2   SITE STRATIGRAPHY

Stratigraphic units that have been identified from subsurface exposures (trenches and test pits) and core samples are shown in cross sections on Figure 3-1 and Plate 4. A summary of the major stratigraphic units and their ages is provided in Table 3-2. A brief description of each of the major units is as follows.

Salt Lake Group (middle to late Miocene)

Trench T-1 (Plate 2) exposed a section of predominantly claystone and tuffaceous siltstone with interbeds of siliceous vitric ash (tuff) and minor gravelly sandstone. Four tuff and ash samples collected from Trench T-1 were analyzed by Dr. Perkins using microprobe analyses at the University of Utah. A summary of the results of the analysis, which are discussed in Appendix D, is provided in Table 3-2. Three of the samples (TR-1, TR-2, and TR-3) appear to be from the same ash fall unit. This gray vitric tuff unit does not match any of the dated silicic fallout tuff units that are part of the late Cenozoic vitric tephra data base established by the University of Utah. The ash bed, herein referred to as the Skull Valley ash bed, most closely resembles a tuff in the Salt Lake Formation in Cache Valley, Utah. The Salt Lake formation in Cache Valley was deposited during the interval from 11 Ma to 5 Ma (Perkins, unpublished data). A fourth sample (TR1-4) collected from a thin interbed in the section is a white biotite bearing ash bed that is a good compositional match to two ~15.4 Ma ash beds in the Rio Grande Rift north of Santa Fe, New Mexico. The possible match of a sample with two or more different ash beds is not uncommon when using probe analyses for correlations (see discussion of analyses in Appendix D). The results suggest that samples TR1-1, TR1-2, TR1-3, and TR1-4 are middle to late Miocene in age and are part of the Salt Lake formation, which regionally ranges in age from ~16 to 4 Ma.

Tertiary Salt Lake group sediments were encountered in a deep boring (boring C-5) that was completed as part of the Quaternary mapping program. Reddish brown sandy silt and clay and possibly a tuff unit (based on white sediments in air rotary cuttings) was encountered at a depth of 26 m (86 ft). A tuff unit encountered in SWEC boring A-1 at a depth of between 26 to 27.5

m (85 to 90 ft) was previously analyzed and correlates to the 6.4 Ma Walcott tuff as reported in the Safety Analysis Report (SWEC, 1997).

Pre-Little Valley Alluvium and Soil (pre-160 ka)

The oldest Quaternary deposits recognized at the site consist of sandy gravel channel alluvium exposed at the western end of Trench T-1 (Plate 2) and in the lower part of test pits T-18 and T-20. The unit is best exposed in Trench T-1 where the channel deposits consist of a coarse boulder gravel facies (Unit Q1a) that was deposited as a channelized debris flow that is interbedded with alluvial/colluvial sand-ramp deposit (Unit Q1b). A strongly developed soil (Unit Q1c) characterized by laminar, platey carbonate structure and thick carbonate rinds (up to 7 mm thick; Stage IV K-soil horizon development) is formed in the upper 1 to 1.5 m (3 to 5 ft) of both units.

The strong carbonate development and its relative stratigraphic position below the pre-Bonneville sand-ramp deposits in TP-18 and TP-20 attest to the relative antiquity of this unit compared to other Quaternary deposits exposed at the site. The deposits are inferred to correlate to a pre-Little Valley lacustrine cycle age (older than 160 ka). Machette and Scott (1988) cite evidence for a significant period of subaerial exposure in the Bonneville basin subsequent to deposition of the Lava Creek ash (approximately 600 ka). Given the relative topographic position of the site area, this period of subaerial exposure may not have been terminated in the site area until the region was inundated during the Little Valley lake cycle. It is possible that the soil formed on unit Q1 in Trench T-1 formed during this approximately 400,000-year-long interpluvial period of subaerial deposition, erosion, and soil formation. The age of these deposits is not well constrained. 600 ka is considered to be the minimum age of a this deposit. They could be much older.

Little Valley Lacustrine Cycle Deposits (150 to 130 ka)

Deposits representing the penultimate lake cycle, the Little Valley lake cycle, which occurred ~ 160 to 130 ka (correlative with marine oxygen-isotope stage 6, Shackleton and Opdyke, 1973) were encountered in borings C-4 and C-5. Little Valley lacustrine deposits are best evidenced in boring C-4 where a sequence of lacustrine deposits that pre-date the Bonneville lake cycle occurs at depths of 9.4 to 13.7 m (30.8 to 45 ft). The deposits consist of a basal sandy gravel (beach facies) that fines upward to a silty clay with ostracode faunas (deep-water facies) that in turn is overlain by a sequence of well-bedded sand with heavy mineral layering (regressive beach facies).

Little Valley lacustrine deposits lie at depths of greater than 13.7 m (45 ft) beneath the proposed storage area. Little Valley lacustrine deposits were encountered only in boring C-5. In this boring, deposits that lie below pre-Bonneville alluvium consist of gravelly sand and clayey sand containing black, laminated mineral horizons interbedded with laminated sandy silt and silty sand. The sands appear to have been deposited in a beach environment where wave action provides a mechanism for sorting heavy mineral layers. The significant amount of gravel in the section suggests proximity to alluvial channels draining into the lake (possibly a lagoon environment near the mouth of a paleo-Indian Hickman Creek channel).

Promontory Soil developed in Pre-Bonneville Alluvium and Eolian Deposits (130 to 28 ka)

The Promontory soil and deposits in which it formed represent a period of subaerial exposure that occurred during the interpluvial period between the Little Valley and Bonneville lacustrine cycles (approximately 130 to 28 ka) (Machette and Scott, 1988). The Promontory soil was observed in subsurface exposures in Trench T-1 and test pits T-18 and T-20. The soil in these exposures, which is formed in pre-Bonneville alluvium and eolian or reworked eolian (sand-ramp) deposits, is characterized by stage II carbonate soil profile development (i.e., disseminated carbonate matrix, continuous 1-mm-thick coatings on pebbles). In Trench T-1, the Promontory soil is developed in sand-ramp deposits that, like the younger post-Provo sand-ramp, consist of a basal lag gravel overlain by a sequence of predominantly reworked eolian silty sand and interbedded sandy gravel lenses. The relative degree of soil profile development (i.e., pedogenic carbonate accumulation) compared to soils formed on younger post-Provo deposits suggests that the soil formed over at least a 20,000- to 30,000-yr period prior to the Bonneville transgression approximately 28 ka. This suggests that the deposits that the Promontory soil formed on are at least 50,000 to 60,000 years old.

The Promontory soil also was encountered in several borings as evidenced by the presence of similar 1- to 2-mm-thick carbonate rinds on alluvial gravel clasts or carbonate-cemented eolian deposits (Figure 3-1 and Plate 4). The upper part of the soil in the site area may have been partially eroded during the early transgression of Lake Bonneville. The prominent reflector observed in seismic data at a depth of about 0.15 msec appears to coincide with the unconformity as mapped from boring data.

The Promontory soil and associated pre-Bonneville deposits generally are relatively thin (< 2 to 3 m [< 5 to 10 ft]) beneath the proposed storage area. In many of the borings, the borings terminated in this unit (refusal when drilling with the hollow-stem auger) and the total thickness of the unit was not determined.

Bonneville Lacustrine Cycle Deposits (28 to 12 ka)

The general sequence of deposits associated with the Lake Bonneville lacustrine cycle (referred to as the Bonneville alloformation) consist of coarse-grained littoral deposits at the base grading upward into sandy marl and laminated marl (Stansbury oscillation phase) that grades up to sandy marl (post-Stansbury transgressive-phase) and laminated and massive, blocky marl units (Bonneville deep-water phase), which in turn, is overlain by a lighter-colored marl (the Provo deep-water phase). The stratigraphic section observed at the proposed PFSF site is similar to sections that have been studied elsewhere in the Bonneville basin. In particular, the section that we correlate to the Stansbury oscillation (the Stansbury deep-water and regressive facies) is very similar stratigraphically to the type locality at Stansbury Gulch on Stansbury Island (Oviatt and Miller, 1997). Figure 3-3 places the stratigraphic nomenclature used in this study into the context of the Pleistocene chronology of Lake Bonneville.

Stansbury Transgression Facies

This unit primarily consists of massive, marly, very fine to medium grained, well sorted sand. The unit maintains a relatively uniform thickness of 5 to 5.5 m (17 to 19 ft) across the entire site (Plate 4). In the center of the site area it was generally encountered at a depth of about 8 to 9 m (28 to 30 m) and extended to a depth of 13.7 to 14.3 m (45 to 47 ft). This unit includes some thin, clay beds and locally thin gravel stringers. The basal part of the unit locally consists of interbedded gravelly sand and sandy gravel containing subrounded clasts and reworked gravel from the underlying pre-Bonneville units. The sand likely was deposited in a littoral to nearshore-deltaic environment.

Stansbury Deep-water Facies

Thinly bedded to laminated sandy marl and marly sand with thin (less than 1 mm thick), white beds with diatoms, aragonite, small ostracodes, and abundant charophytes (carbonate casts of fine plant-stem or algal-filaments) were encountered at a depth of about 5 to 6 m (17 to 18 ft) in test pits TP-7 and TP-8. Ostracodes and charophytes extracted from the white marl layers from this unit (Samples 4790/FS-1a/TP-7 and 4790/FS-1a/TP-8) yielded radiocarbon dates of 24,600 ± 190 and 23,990 ± 380 RCYBP, respectively (see Appendix D). The unit thickens gradually to the west across section 6 from 2.1 to 2.4 m (7 to 8 ft) in the eastern half of the section to 3 to 3.3 m (10 to 11 ft) in the center of the western half of the section.

Stansbury Regressive Facies

A lowstand unconformity was identified in the sections exposed in test pits TP-7, TP-8, and Trench T-2. In test pits TP-7 and TP-8, gypsiferous mud interfingering with loose silty sand to

fine sand lenses unconformably overlies the Stansbury deep-water facies sediments. The deposits are most easily identified where the contact is unconformable. The deposits associated with this unconformity are relatively thin (less than about 0.5 m) and grade upwards into the overlying transgressive deposits making it difficult to differentiate the contact between regressive and transgressive deposits in some core samples. This unit was not differentiated in many of the borings (see Plate 4).

Post-Stansbury Transgressive Facies

The post-Stansbury transgressive facies consists of a sequence of marly sandy silt to silty sand and interbedded sandy silt and silty clay. The presence of ostracodes in the fine-grained interbeds suggest that these beds represent deeper-water conditions in the lake level subsequent to the Stansbury lowstand. In test pits TP-7 and TP-8, a single prominent marly interbed is present in the lower part of the transgressive sequence. This interbed may correlate with a secondary fluctuation during the Stansbury oscillation (spike C on Figure 3-3b) or during the rise to the Bonneville shoreline (e.g., U1 on Figure 3-3a). Elsewhere (e.g., Trench T-2) the sequence includes multiple thin silty clay to clayey silt interbeds at the same general altitude.

The sequence of prominent sand ridges mapped between the proposed storage area and the northern flank of Hickman Knolls (T5S, R8W, sections 5, 6, 7, and 8) (Figure 1-3) and an E-W-trending cross-valley barrier beach gravel bar that can be traced for a distance of at least 4.8 km (3 mi) from near the center of Section 7, T5S, R8W to center of Section 10, T5S, R9W) (Plates 1 and 5) were deposited during the post-Stansbury transgressive phase. The gravel bar, which lies at a general altitude of about 4514 ± 2 ft formed in shallow water below the Stansbury shoreline. The Stansbury shoreline, one of the conspicuous late Pleistocene shorelines of Lake Bonneville, consists of tufa-cemented gravel and barrier beaches within a vertical zone of about 45 m, the lower limit of which is 70 m above the modern average level of Great Salt Lake (Oviatt and others, 1990). Oviatt and others (1990) cite stratigraphic evidence at a number of localities that shows the Stansbury shoreline formed during the transgressive phase of late Pleistocene Lake Bonneville (sometime between about 22,000 and 20,000 yr B. P.). Stratigraphic relationships in test pit TP-19, which most clearly document the relative ages of Stansbury shoreline and nearshore facies in the proposed PFSF site area, support this correlation. In this test pit, clast-supported, well-rounded sandy gravel that lies at an altitude of about 4512 ft (Stansbury gravel bar) overlies a thick (at least 3 m [10 ft]) section of cross-bedded medium sand to interbedded silty very fine to fine sand that in turn overlies laminar, marly sand to sandy marl (Stansbury deep-water facies). The gravel deposit is overlain by

silty fine sand that was deposited as the lake deepened during the transgression to the Bonneville shoreline.

Additional stratigraphic evidence from auger holes (AH-2 and AH-3, Appendix D) and test pit TP-11 (Appendix C, Figure C-1) support a pre-Bonneville deep-water phase age for the sand ridges that lie north of Hickman Knolls. As shown on the map of the north wall of TP-11, the ridges are underlain by well sorted, silty fine to very fine sand. Marl and reworked marl that was deposited during the Bonneville deep-water phase onlap the sand ridges and in turn are overlain by post-Provo eolian and playa deposits.

Bonneville Deep-water Facies

Two deep-water facies units are identified in test-pit and trench exposures and in core from borings completed for this study. The lower unit consists of an upward-fining sequence of pale brown, well bedded, thinly laminated sandy marl containing abundant ostracodes. The lower contact of this unit is gradational to the underlying transgressive–phase littoral sediments. The laminated marl is overlain by a gray to olive (with white mottling) massive, very fine sandy clayey silt (marl) that contains abundant ostracodes and exhibits coarse angular blocky structure. The contact between the laminated marl and massive, blocky marl generally is a sharp, well defined contact. Oviatt and others (1994) describe fossil ostracode faunas for similar units that are recognized throughout the Bonneville basin (Oviatt and Miller, 1997). They conclude that the massive unit represents the deepest-water phase of Lake Bonneville that culminated about 15 ka. Dropstones (ice rafted pebbles) are observed in both marl units.

Locally, the upper part of the massive, blocky unit exhibits prominent reddish brown mottling in addition to more abundant white mottles. This zone may represent the Bonneville flood event, but this interpretation is speculative. Oviatt and Miller (1997) note that the flood unit elsewhere in the basin consists of a sandy laminated unit that in many places contains abundant reworked ostracodes. We did not observe a similar laminated unit in the proposed PFSF site area.

Provo Deep-water Facies

In several of the test pits (TP-1, TP-7, TP-8) and Trench T-2, the massive, blocky upper Bonneville deep-water sediments are overlain by a pale brown, massive sandy marl unit that is interpreted to have been deposited subsequent to the Bonneville flood (approximately 14.5 ka) during the Provo stage and initial regression (14.5 to 12 ka). A cambic B soil horizon marked by a reddening along ped faces is formed in the upper part of the unit.

The Provo deep-water sediments are missing in some areas where they appear to have been eroded. A number of regressional shorelines have been mapped across the proposed PFSF site area (Figure 1-3). Stratigraphic relationships in test pits TP-7, TP-8, and TP-9 suggest that these shorelines are predominantly erosional rather than depositional features. For example, in test pit TP-9, which lies below a prominent shoreline feature (Figure 3-3), Provo deep-water sediments and the upper (massive, blocky) Bonneville deep-water unit have been eroded (Plate 4).

Post-Provo Recessional Facies

Provo recessional deposits were not clearly identified in any of the subsurface trench or test pit exposures or in core samples. In test pit TP-1 a thin unit of sandy silt containing a few ostracode fragments was identified above the Provo deep-water sediments. As noted above, the recessional shorelines appear to have been primarily erosional features with little or no associated deposits.

Post-Provo Subaerial Deposits (post-12 ka)

Post-Provo Eolian, Reworked Eolian, and Playa Deposits
Bonneville lacustrine sediments in the proposed storage facility site area generally are overlain by a thin (less than 2.5 m thick) mantle of eolian , reworked eolian, or playa sediment. A weak soil marked by platey soil structure and weak (Stage I) carbonate accumulation is formed in these deposits.

Post-Provo Sand-ramp
Thicker deposits of eolian and reworked eolian and alluvium comprise the modern sand-ramp that is formed along the flanks of Hickman Knolls. The sand-ramp consists of fine sand (eolian and reworked eolian material) interbedded with sandy gravel (alluvium). The sandy gravel and gravelly sand faction decrease in relative abundance with increasing distance down the fan surface away from the bedrock outcrop. A coarse boulder gravel lag comprises the basal facies of the sand-ramp.

4.0   BEDROCK GEOLOGY

Hickman Knolls is an area of low-lying bedrock outcrop in central Skull Valley that lies immediately south of the site (Figure 4-1). This exposure is important to site characterization because it provides a long-term record of the bedrock conditions in the immediate vicinity of the site. Geologic mapping of the lithologic and structural characteristics of Hickman Knolls (Sections 4.1 and 4.2) was conducted to characterize the bedrock. The results of the bedrock mapping provide a basic constraint on the location and amounts of potential faulting in the site area (Section 4.3). Exposures of deformed Tertiary strata in Trench T-1, excavated along the northern flank of Hickman Knolls, provide additional information regarding the style and nature of late Cenozoic deformation in the site area (Section 4.4).

4.1   LITHOLOGY

Bedrock exposed on Hickman Knolls consists of primarily of dolomite breccia and limestone breccia. The breccias are poorly sorted, and the breccia texture is fairly uniform among the varying lithologies. Individual clasts range in size from less than one millimeter to several meters in diameter, with an average size-range of 1 –10 cm. Post-depositional growth and crystalline calcite and massive silica are common within the matrix, the clasts, and veins that cut across the breccia fabric.

At the scale of several adjacent outcrops, distinct lithologic domains are recognized that reflect layering within the bedrock. The three most important lithologic domains are:

1. Very dark gray ("black") to medium gray calcitic dolomite. This is the most common lithologic unit and accounts for about 75% of the bedrock exposed at Hickman Knolls.

2. Light gray silicic limestone breccia; and

3. Light reddish brown, strongly recrystallized limestone with abundant reddish-brown chert.

The degree of brecciation is variable, from pervasive fracturing of intact strata with little to no rotation and translation of adjacent clasts, to complete brecciation with no apparent structural continuity of the rockmass (Figure 4-2). This variability was observed in a single outcrop at several locations. Bedding is relatively rare and outcrops containing recognizable bedding accounts for less than about 15% of the exposed bedrock. Most of the breccia development is fairly uniform, with neighboring clasts mostly having very similar to identical lithology. Continuity of internal primary structure between adjacent clasts is apparent at some locations,

however clasts typically appear rotated and separated from their original neighbors, but with very little lithologic mixing.

The breccias all are clast-supported, having a matrix that accounts for less than about 10% of the rock volume. The matrix is a combination of argillaceous material, very finely comminuted limestone, and secondary calcite and silica. Early post-depositional alteration by pressure solution during diagenesis is indicated by close packing and interlocking of clasts. A pressure solution cleavage that cuts across the matrix and clasts also is present, but is only developed locally. Matrix-supported breccias, where clasts are supported by secondary deposits of carbonate and/or silica were observed only immediately adjacent to faults and fault zones.

Although much of the breccia appears massive with a random internal fabric, many outcrops exhibit a crude layering of the breccia that appears both depositional and structural in origin. At the scale of the outcrop, the breccia layering appears as discontinuous lens-shaped packages of similar bedrock lithology and breccia structure. The breccia lenses are bounded by thoroughgoing fractures, many of which have a curviplanar sigmoidal geometry suggesting they may have originated as small shear planes. At a few locations such as at the north end of the knolls, this local breccia layering is bounded by discontinuous, low-angle, north-dipping extensional fractures and faults filled with calcite and silica (Figure 4-3).

Primary structure defined by the breccia layering that is consistent across larger areas is delineated by subtle outcrop morphology at the northwestern, eastern and southeastern margins of the Knolls. At these locations primary structure appears as a geomorphic layering in the landscape defined by banding of vegetation and subtle outcrop morphology. At both locations the layering dips to the east and southeast. At a few localities, direct measurement in outcrop indicates bedding is oblique to the southwest-dipping layers defined in the landscape. These observations, together with observations of a breccia layering in outcrop (Section 4.2), suggest the southwest dips reflect primary structure penecontemporaneous with brecciation.

Regional Stratigraphic Correlation

Moore and Sorenson (1979) assign the rocks exposed at Hickman Knolls to map unit "Ocq" representing lower, middle and upper Ordovician carbonates and quartzite. Lower and middle Ordovician strata in northwest Utah were deposited in a shallowing ocean/continental margin environment represented by a thick sequence of regionally continuous limestone (Garden City Formation) (Hintze, 1988). These strata are overlain by thin and discontinuous upper mid-Ordovician clastics of the Kanosh shale and Swan Peak/Eureka quartzites, deposited on the

southern margin of a broad, uplifting structural high, the Tooele Arch . The upper Ordovician Fish Haven dolomite is regionally continuous across the Toole Arch, and is notable as a resistant cliff-forming section throughout northwest Utah (Hintze, 1988).

Ordovician rocks in the Stansbury Mountains are represented by the lower to middle Ordovician Garden City formation limestone overlain by thin, discontinuous middle Ordovician clastics, and upper Ordovician dolomite (Teichert, 1959). The Ordovician sequence in the site area was measured and described by Teichert (1959) from exposures on the west slopes of the Stansbury Mountains, two miles east of the range front and four miles north of Johnson Pass (Plate 6). Teichert (1959) also measured and described the Kanosh shale and Fish Haven dolomite from exposures in the same area.

A definitive assignment of the Hickman Knolls bedrock to known formations was not attempted during this study. Based on the descriptions of regional stratigraphy in northwest Utah (Hintze, 1988), and on the previous bedrock geologic mapping of the Stansbury Mountains-Skull Valley region by Teichert (1959) and Rigby (1958), the bedrock at Hickman Knolls is considered middle to upper Ordovician in age. The dominant black dolomite lithology and its very resistant nature suggests the bedrock belongs to the lower Fish Haven formation.

4.2   STRUCTURE

At the outcrop scale, the fabric and texture of the breccia dominate the structure of the bedrock. In addition to the breccia fabric, two classes of structures are described for the study area: faults (ductile shearing and cataclasis); and fractures (including cleavage) that post-date brecciation.

Faults

Two different styles of faulting that reflect fundamentally different deformation mechanisms are recognized at Hickman Knolls: (1) brittle faults formed by discontinuous cataclasis under low temperature and pressure environmental conditions (Figure 4-4a); and (2) ductile shear zones formed by continuous ductile flow, suggesting relatively slow deformation under elevated temperature conditions (Figure 4-4b). These deformation mechanisms are attributed to very different environmental conditions that indicate the prevalent tectonic conditions during faulting. The conditions of faulting also form the basis for inferring a tectonic or nontectonic origin for the deformation.

The largest fault-related structure at Hickman Knolls is a low-angle, ductile shear zone that dips east and north. This shear zone is well exposed at the northwest margin of the Knolls, and at the base of the north-trending bedrock scarp near the center of the knolls. The light gray layer exposed in the northwest consists of a 1-2 m-thick zone of very light gray layers within the black dolomite that dips moderately to the east (Figure 4-4b). The individual layers are 10 cm to one meter thick, and thinner layers are discontinuous along strike. Many of the layers exhibit strongly developed asymmetric shear structures including shear bands, reidel shears and pinch-and-swell structures that all indicate down-to-the-west extensional displacement.

The exposure near the center of the knolls consists of a 3-5 m-thick very light gray layer within the black dolomite breccia. This layer dips gently to the north at about 15°, and has been sheared parallel to its upper and lower contacts. The shearing has produced a series of large pinch-and swell structures that affect the entire layer of light gray dolomite. The pinch-and-swell structures are symmetric; asymmetric structures that would indicate the relative sense of shear were not recognized. The pinch-and-swell structures are produced by extensional strain, suggesting the structure is an extensional shear zone in which the upper plate was translated to the north.

At both of these locations the light gray layers that define the shear zone have no apparent lithologic contrast to the surrounding black dolomite. In hand specimen, there is also no indication of a mechanical contrast between the shear zone and the surrounding host rock. Deformation by ductile mechanisms unlikely will be localized and produce these structures without anisotropy within the deforming rockmass (e.g., Ramsay, 1967; Price and Cosgrove, 1991). This observation suggests the rock has undergone considerable alteration since the deformation occurred, consistent with a dolomitization process, and also with the evidence for abundant fluid flow and vein formation during a later brittle-ductile and brittle phase of deformation (see discussion of fractures below).

The low-angle ductile shear zone is associated with a lithologically distinctive unit composed of strongly recrystallized, light grayish yellow dolomitized pelitic limestone breccia containing abundant lenses of extended chert stringers. The lithologic unit lies structurally and topographically below the shear zone (in the footwall) by about 7 m at both locations. This structural-stratigraphic association provides a marker horizon that covers the eastern two-thirds of the Knolls. Bedrock mapping indicates this complex marker horizon is offset less than about 15 m down-on-the-west between the exposure in the center of the Knolls and the exposure at the northwest margin.

Faults formed by cataclasis at low pressure and temperature conditions also are present within Hickman Knolls. The most prevalent of these structures are faults directly related to the brecciation process. These are small-scale structures that commonly form the margins to the layering within the breccia, but also cut across the layering in some places. The most distinguishing characteristic of these faults is their very limited extent. Even faults that have a strong lithologic expression, alteration by fluid flow, and strongly developed cataclastic texture have strike lengths of less than several meters. This characteristic indicates anomalously rapid attenuation of displacement along strike that is not characteristic of tectonic faults (e.g., Cowie and Scholz, 1992). We infer that the strain on these faults is consumed by the process of brecciation and, therefore, must be penecontemporaneous.

Fractures

The most common structural features not related directly to brecciation are north-south trending and east-west trending high-angle fractures. Both of these fracture-sets form prominent bedrock scarps from less than 1 meter to greater than 7 meters in height. These scarps have a strong expression in the morphology of Hickman Knolls and are associated with many of the lineaments interpreted from aerial photographs (Plate1). The north-trending scarps are the most prominent of these fractures. These fractures are both open cracks, particularly where they are located along bedrock scarps, and filled with secondary calcite and silica. The silica-cemented fractures are mostly located adjacent to faults. The north-trending and east-trending fractures were investigated in detail across the entire Knolls, and no evidence of faulting on the basis of structural indication for shearing or lithologic evidence for stratigraphic offset was observed.

4.3   IMPLICATIONS TO LOCAL FAULT STRUCTURE

Geologic mapping of the bedrock lithology and structure exposed at Hickman Knolls provides a fundamental constraint on the amount and location of faulting in bedrock in the vicinity of the site in three direct ways: (1) No thoroughgoing faults were observed that cross Hickman Knolls, independent of lithology; (2) No major lithologic discontinuities, independent of structure, were observed that would indicate the presence of a significant fault; and (3) the outcrop location of structural-stratigraphic markers associated with a distinctive low-angle ductile shear zone suggest a maximum of 15 m vertical offset in bedrock between the east-central and western portion of the Knolls.

Four main conclusions regarding the location, style, and magnitude of local faulting are made from the lithology and structure of bedrock observed at Hickman Knolls:

1. The presence of Paleozoic bedrock in the central Skull Valley, together with geophysical evidence for the presence of a buried Tertiary basin immediately to the west, supports the regional structural interpretation of a major west-dipping normal fault west of Hickman Knolls;

2. It is unlikely there exists a major fault extending through Hickman Knolls with significant offset;

3. The majority of the deformation is consistent with in situ or translatory brecciation of semi-consolidated material in an early post-depositional environment; and

4. A later phase of low-strain, brittle deformation is expressed as north-south and east-west vertical fractures that post-date earlier ductile shearing.

4.4   TRENCH T-1

Trench T-1 revealed a 70 m-long exposure of Tertiary bedrock overlain by Quaternary alluvial and minor pluvial deposits (Plate 2). The Tertiary section consists of siltstone, claystone and volcanic tuffs. These deposits are assigned to the late Miocene to Pliocene Salt Lake formation based on microprobe analysis and correlation of one of the ash units to an ash deposit of middle to late Miocene age (Section 3.2; Appendix D). A gravelly, sandy silt of uncertain age and origin overlies and appears to be tectonically emplaced within the Tertiary strata. This unit, designated unit Q/T on Plate 2, is interpreted to be landslide debris of Quaternary?/Tertiary age based on its composition and stratigraphic position. Three alluvial and pluvial deposits that are early/middle? to late Pleistocene in age overlie and are inset into the Tertiary strata. For a discussion of these units see Section 3.2.

Faults and folds deform the Miocene Quaternary?/Tertiary, and locally Pleistocene deposits exposed in Trench T1. Miocene strata are strongly deformed by normal faults, reverse faults and oblique-slip faults throughout the entire exposure (Plate 2). The deformation in Trench T-1 appears to represent two different styles and episodes of deformation. An earlier period of deformation is characterized by low-to-moderate angle reverse faulting, associated folding, and small scale extensional (bending-moment) normal faulting. As described below, this deformation is attributed to nontectonic deformation mechanisms. A latter period of extensional deformation that involves Quaternary deposits locally overprints this deformation. This deformation, which is consistent with the style, orientation, and deformation observed in geophysical data north of Hickman Knolls, is attributed to late Cenozoic faulting.

Late Cenozoic Faulting

Normal faults exposed between Stations 60 and 65 exhibit the strongest evidence of late

Cenozoic faulting. The fault located at Station 65 exhibits the largest offset of any of the faults exposed in the trench. A prominent sequence of white vitric tuff (unit T5a) overlain by reworked ash (units T5b and T5c) is displaced a minimum of 3.25 m down-on-the-east across this fault and the east-dipping fault at Station 60. The steep dip of the fault at Station 65 and adjacent shear deformation on both the east and west sides indicate a component of strike slip, but the amount could not be determined. A similar high angle, north-trending predominantly normal fault having a component of oblique slip also was observed in test pit TP-12 approximately 13 m east of this fault. Although the location of this fault is not coincident with the projection of the fault exposed in Trench T-1, the similar location, orientation and indication of oblique slip suggest they may be structurally related. Both of these structures trend north-south, similar to the prominent fracture set present in the Paleozoic bedrock of Hickman Knolls

In Trench T-1 Post-Little Valley sand ramp deposits are displaced across the zone of closely-spaced normal faults between Stations 61 and 64. Deposition of the sand ramp likely was initiated shortly after the recession of the Little Valley lake cycle about 130 ka. The Promontory Soil, characterized by a Stage II+ carbonate accumulation, is developed in these deposits. Based on the amount of carbonate accumulation, this soil likely represents a minimum of 20 to 30 ka period of soil formation prior to burial. The upper part of the soil may have been truncated during deposition of the overlying Post-Provo sand ramp. The faults do not extend up into the overlying Post-Provo sand ramp. The timing of most recent faulting is thus constrained to have occurred post-130 ka (?) and pre-12 ka. The maximum vertical stratigraphic separation on the base of the Post-Little Valley sand ramp deposits (unit Q2b) across the zone is 0.5 to 0.7 m. The displacement on individual faults that are expressed as thin, reddish clay seams, ranges from < 4 cm to about 15 cm.

Similar reddish clay seams also were observed at the eastern end of Trench T-1 near Station14. Only one of these clay seams could be traced into the underlying Tertiary strata. This structure exhibited < 10 cm of displacement of a Tertiary horizon.

The north-trending structures within Trench T-1 that exhibit evidence of Pleistocene activity are judged to be active secondary faults within the distributed zone of faulting between the East and West faults. Possible correlation to faults identified in the high-resolution s-wave seismic data to the north is discussed in Section 5.2.4. – Nontectonic Deformation. Several aspects of the earlier phase of deformation observed in Trench T1 indicate a local, nontectonic origin. The reverse structures have a moderate to low angle of dip, with highly variable strike and dip

orientation as indicated by the attitude of shear planes and isoclinal folds. The variable strike of the contractional structures suggests the deformation occurred under very low lithostatic conditions at the near surface, unconstrained by a consistent stress field characteristic of tectonic deformation. Much of the extensional deformation, which crosscuts and offsets the compressional structures, also exhibits highly variable orientation of structure, appears to be associated with broad fold structures, and appears to detach at a very shallow depth beneath the trench exposure. All of the observed displacements on the dip-slip faults in the trench exhibit small amounts of displacement.

Folding of the Tertiary strata, evidenced by northeast-plunging recumbent folding of unit T3 between stations 67 and 70, broad warping of units T8, T9, and T10 between stations 48 and 62, overturned strata between stations 38 and 44, and northward-plunging slip planes in Tertiary strata and at the contact with the Q/T unit between stations 16 and 19, appears to have occurred in conjunction with the compressional faulting. The general northward plunge of structures suggests a relative northward direction of movement.

The compressional deformation exposed in Trench T-1 is consistent with a localized detachment or landslide originating on the northern flank of Hickman Knolls. We interpret the Q/T unit to be landslide debris incorporated into the section during movement of the slide mass. The upper headscarp of the postulated landslide or lateral slump block likely would be located within the broad sediment-filled embayment between bedrock outcrop in the northwestern part of Hickman Knolls. The thick accumulation of sand ramp deposits in this area has buried or obscured the location of the headwall region. The indication of a nontectonic origin for the observed deformation in Trench T1, and the nontectonic origin of deformation in Paleozoic bedrock exposed on Hickman Knolls alternatively may lead to the suggestion that Hickman Knolls could have originated as a larger scale detached bedrock slide. As noted in the SAR (p.2 of Appendix 2A of SWEC, 1997), there has been speculation that Hickman Knolls may be a detached block of bedrock that moved as a large slide mass into the basin. Large scale (300 to 400 km[2)] landslide blocks or rock-avalanches of Miocene age have been identified at several localities within the Basin and Range, including the Avawatz Mountains (Spencer, 1990), Death Valley areas (Topping, 1993), Soda Mountains (Grose, 1959), Old Dad Mountains (Dunne, 1977) and Halloran/Silurian Hills Area (Bishop, 1997) of southeastern California and the Matlin Mountains of northwestern Utah (Todd, 1983). Bishop (1997) notes that conditions favorable to avalanche deposition were widespread during Miocene extension. Todd (1983) cites evidence to suggest a genetic relation between volcanic activity, subjacent intrusion (?),

and low-angle faulting, that is, a model that involves shallow crustal extension sited over Tertiary intrusions.

Low-angle faulting and folding observed in Trench T-1 at the northern margin of Hickman Knolls shares some characteristics in common with the localities cited above. The low-angle fault surfaces truncate Tertiary strata, involve lenses of fine-grained tuffaceous sediments or volcanic ash that may have lubricated movement, and are associated with recumbent folding of more competent siltstone beds. The latter suggests that the Tertiary strata may have been unconsolidated or partially saturated at the time of deformation. However, significant differences are noted and it is more likely that the deformation observed in this trench resulted from a localized slide mass originating on the flanks of Hickman Knolls rather than movement of the entire Hickman Knolls bedrock mass.

Lithologic features of mega-breccia sheets interpreted to be rock-avalanche deposits in the Halloran/Silurian Hills area include monolithologic composition, crackle and jigsaw breccia textures, large blocks up to tens of meters across, low (5-20 percent) matrix content, clastic dikes, and basal striations (Bishop, 1997). In the Matlin Mountains, the displaced terrain is composed of five brecciated displaced sheets of pre-Tertiary rocks, each resting upon Tertiary sedimentary rocks, the lowest sheet overlying the rooted terrain (Todd, 1983).

Although brecciation and low-angle ductile shear zone are observed in the Paleozoic bedrock of Hickman Knolls, this deformation is consistent with deformation in semi-consolidated material during an early post-depositional environment. Basal detachment faults of possible late Cenozoic age (i.e., cataclastic mechanism of deformation) are not exposed within the bedrock of Hickman Knolls. Todd (1983) observes basal ductile shear structures interpreted as the result of frictional heating during sliding. Although a viable mechanism for the observations in the Matlin Mountains, we observe no indication of shear heating in the Paleozoic rocks of Hickman Knolls. There also is no evidence for elevated temperatures associated with the deformation observed in Trench T-1. If the structures in Trench T-1 were related to basal sliding of a detached Hickman Knolls, there should be evidence for high-temperature alteration of the sediments because they are in such close proximity to the Paleozoic bedrock.

The shear strains associated with the low-angle ductile shear zone exposed in Hickman Knolls are high, whereas those in Trench T-1 are relatively low. The low-angle faults exposed in Trench T-1 juxtapose Tertiary sediments, but there is no indication of a contact between

Paleozoic bedrock and the Tertiary lithologies or structures. The brecciation and ductile shearing of Hickman Knolls bedrock is Paleozoic in age, whereas the deformation in Trench T-1 is mid-late Tertiary and younger.

We conclude, therefore, that the compressional faulting and associated folding observed in Trench T-1 is nontectonic, probably related to local landsliding. We cannot preclude, however, with the available data the possibility of a larger scale landslide block. A regional detached block model would preclude the need for a major west-dipping normal fault west of Hickman Knolls. Although, we do not favor this model, we have given it some weight as a factor in our assessment of the seismogenic capability of the West fault in our seismic source characterization model (see Section 6.0).

5.0 NATURE AND TIMING OF QUATERNARY DEFORMATION

The faults most significant to the fault evaluation study include:

- The Stansbury fault zone, which lies 9 km east of the site and is the main structural boundary between the Skull Valley half graben and the uplifted Stansbury Mountains to the east;

- two mid-valley faults, the East fault and the West fault, which lie about 0.9 km east and 2 km west of the site respectively; and

- a broad zone of distributed faulting on the down-thrown side of the East fault that is bounded by the two mid-valley faults.

The results of detailed field and/or subsurface investigations to assess the nature and timing of Quaternary faulting on these features are presented below.

5.1 STANSBURY FAULT ZONE

The Stansbury fault forms the border between the western margin of the Stansbury Mountains and piedmont slopes that border the eastern margin of Skull Valley (Plate 6). At its closest location, the main fault scarp is 9 km west of the east border of the proposed PFSF site. The Stansbury fault dips to the west, and has had down-on-the-west displacement of late Quaternary alluvium derived from the Stansbury Mountains. Previous investigations show the length of fault that has had late Quaternary displacement is approximately 40 to 45 km (Hecker, 1993; Helm, 1995). The Stansbury fault, as defined by previous workers, extends from the northern end of the Stansbury Mountains at the village of Timpie, to Johnson Pass near the village of Willow Springs. Helm (1995) notes that the fault consists of two distinct sections, separated by a west-trending cross fault coincident with Pass Canyon and the southern margin of Salt Mountain. The 20-km-long section of the fault north of Pass Canyon consists of several strands and has a complex pattern of synthetic and antithetic faults. Helm (1995) notes that displacement along the northern section of the fault is partitioned among several strands, and the 25-km-long southern section of the fault, in contrast, is comparatively simple, with most of the displacement occurring on a single, distinct strand. Helm (1995) shows that these two sections also are associated with differences in range-crest elevation, plan-view geometry, scarp heights, and drainage-basin asymmetry. In addition, regional gravity data suggest that the basin-fill deposits in Skull Valley are thickest adjacent to the highest parts of the Stansbury Mountains thus supporting Helm's (1995) proposed sections of the Stansbury fault. She postulates that the fault sections are rupture segments that may, or may not, rupture independently.

South of Johnson Pass, Hecker (1993) includes a fault trace along the western margin of the Onaqui Mountains, which was mapped by Moore and Sorensen (1979), as part of the Stansbury fault. Sack (1993) also mapped this trace, but referred to it as the Onaqui fault zone. This fault extends from Johnson Pass south to a major canyon named The Dell, a distance of about 9 km. West of The Dell, a bedrock salient extends westward from the base of the Onaqui Mountains, that is crossed by numerous north-trending, discontinuous fault strands (Moore and Sorensen, 1979). South of this salient, the range front is sinuous, and Moore and Sorensen (1979) do not map a fault along the range margin. Sack (1993), however, shows a down-on-the-west fault along the southern 3 km of the western Onaqui Mountains front. The range-crest elevations south of Johnson Pass support the presence of at least one additional fault section between Johnson Pass and Lookout Pass.

All workers agree that there has been late Quaternary movement on the Stansbury fault, but there is some uncertainty concerning the timing of the most-recent earthquake. On the basis of fault-scarp morphology, Barnhard and Dodge (1988) and Helm (1995) suggest that the most recent movement on the Stansbury fault occurred prior to the Lake Bonneville highstand (about 15,000 years ago). In contrast, on the basis of stream nickpoints located a short distance upstream of the scarps, Everitt and Kaliser (1980) concluded that the most recent movement on the fault occurred during the Holocene. Barnhard and Dodge (1988) addressed this possibility by visiting two stream channels that have prominent nickpoints, and concluded that resistant bedrock influenced upstream migration of the nickpoints, and thus that the fault has not had Holocene displacement.

Aerial photographs (1:20,000 scale) were analyzed and a field reconnaissance was conducted along traces of the Stansbury fault east of the site (Figure 5-1) to evaluate the timing and amount of the most recent Quaternary displacements. Scarp profiles were measured across the main fault trace at the mouth of Antelope Canyon (Figure 5-2) and across two secondary traces that lie 1½ to 2 km west of the range front (Figure 5-3).

5.1.1 Main Fault Trace

East of the site the main fault scarp is generally between elevation 5600 and 5800 feet (i.e, about 400 to 500 feet higher than the Bonneville shoreline). The apexes of the alluvial fans are displaced across small graben that are evident at the mouths of Indian Hickman and Antelope Canyons. North of Indian Hickman Canyon, the main fault scarp is readily apparent on the aerial photographs. South of Indian Hickman Canyon, the scarp is more subdued and appears to be eroded and buried by young alluvial fan deposits. At the mouth of Antelope Canyon, a

young stream terrace that is inset below the alluvial fan can be seen on the aerial photographs on the east (upthrown) side of the fault that appears to be truncated by the fault. At the mouth of Indian Hickman Canyon the young alluvial deposits do not appear to be displaced.

Two scarp profiles were measured across the main fault scarp immediately north of Antelope Creek (Figure 5-2). Profile SF-1 is across the graben that displaces the alluvial fan surface. Based on its geomorphic position and the weathering of cobbles and boulders at the fan surface, the fan deposits are inferred to be no younger than the episode of fan deposition in the Basin and Range that is correlated with the Pinedale glaciation. Accordingly, the age of the fan is inferred to be about 35 ± 5 ka. (Tables 3-2 and 5-1). The fault scarp is 12.5 m high and the net vertical displacement across the graben is 4.2 to 5.0 m (Figure 5-2a).

The modern stream is incised more than 15 m below the apex of the fan. There is an approximately 1- to 4-m high terrace that is inset below the fan surface along the north side of the creek. This terrace is displaced across a 2.9-m-high scarp and the vertical displacement of the terrace surface is 1.9 ± 0.2 m. The age of this terrace is not well constrained. Based on the geomorphic position of the terrace and the relatively subdued character of the scarp along this segment of the fault compared to Basin and Range faults that have had late Holocene displacement, the scarp is inferred to have formed during the early to middle Holocene. It probably represents a single displacement event.

5.1.2   Secondary Fault Traces

Sack (1993) maps three secondary fault traces that appear to be northwest-trending splays off of the main fault trace. These fault traces are well expressed on the aerial photographs as 0.8- to 2-km long linear scarps that traverse an alluvial fan surface that has been modified by wave erosion during transgression of the Pleistocene lake to the Bonneville shoreline. The alluvial fan at profiles SF-2 and SF-3 (Figure 5-1) is significantly older than the fan gravel at profile SF-1a. The fan surface is much more dissected. Quartzite boulders and cobbles commonly have thick weathering rinds that consist of a dark red rind up to 1 mm thick over a more diffuse zone of weathering up to 1 cm thick. Boulders having thick rinds that are spalling off are common on the fan surface. These weathering characteristics are characteristic of Bull Lake or older alluvial fans in the Basin and Range. Correlation with the Bull Lake glaciation suggests the fan gravel is at least 160 ka.

Shorelines eroded into the fan surface are clearly truncated along the fault. These shorelines lie above the Provo shoreline and had to have formed prior to, or during, the transgression of the

lake to the Bonneville shoreline. Recessional shorelines would not have formed during the rapid draw down of the lake from the Bonneville to the Provo level. Assuming they formed during the most recent transgression, they are younger than the Stansbury shoreline (about 20 ka) and older than the Bonneville shoreline (about 15 ka). Based on their elevation, they are inferred to be about 18 ± 2 ka. The scarp heights at profiles SF-2 and SF-3 are 3.6 m and 2.8 ± 0.1 m respectively, and the vertical displacements are 2.7 m and 1.9 m (Figure 5-3).

Inflections in the scarp profiles (changes in slope angle in the face of the scarps) indicate the cumulative displacement probably was produced by multiple events. Geomorphic relations along the scarps indicate the cumulative displacement at SF-2 and SF-3 is the result of at least two events on each of these traces.

Southeast of profile SF-2 the scarp intersects a gravel bar (elevation 5240 feet) associated with the Bonneville shoreline. A discontinuous lineament can be traced across the bar that suggests there has been post-Bonneville displacement along this trace. The scarp across the bar is lower than the scarp to the northwest and it has been obscured in most places by Holocene alluvial fans that grade out across the Bonneville shoreline. These relations, interpreted based on the aerial photographs, suggest there was at least one pre-Bonneville event (i.e., prior to ~15 ka) followed by an early to middle Holocene event (i.e., post Bonneville but older than the alluvial fans that bury the Bonneville shoreline). These relations are consistent with the inferred early-to middle-Holocene age for the most recent event on the main trace at Antelope Canyon. Assuming two events, the average displacement per event was 1.4 m.

The timing of the most recent events along the scarp at profile SF-3 are not as well constrained, but the geomorphic relations suggest their ages are similar to those along the scarp at SF-2. The southeast end of the scarp cuts a gravel bar at elevation 5080 feet, which formed during the transgression to the Bonneville shoreline. The bar is younger than the Stansbury shoreline (~20 ka) and older than the Bonneville shoreline (~ 15 ka). Near the northwest end of this feature (0.75 km northwest of profile SF-3), the scarp is breached by a gully and a small debris-flow fan has formed west of (on the down-thrown side of) the scarp. The fan buries the lower half of the scarp face. The presence of the scarp across the apex of this small fan, a sharp vegetation lineament across the fan and the fact that the fan has subsequently been incised suggest this young (middle Holocene ?) fan has been displaced by the fault. Assuming the scarp along profile SF-3 was formed by at least two events indicates an average vertical displacement per event of ≤1m.

5.1.3 Estimated Slip Rate and Average Slip Per Event

Table 5-1 is a summary of the displacement data on the Stansbury fault east of the site and the calculated slip rates. The value of 0.36 mm/yr for the Holocene stream terrace (line b on Table 5-1) is based on a single event displacement. Therefore, it does not represent a reliable average late Quaternary slip rate, which should represent the average behavior during successive events. The late Quaternary rates on the individual traces range between 0.11 ± 0.02 and 0.15 ± 0.02 mm/yr. These rates are somewhat higher than the late Cenozoic rate of 0.07 ± 0.02 mm/yr calculated by Helm (1995) for the northern section of the Stansbury fault, and are generally consistent with published rates of other Basin and Range faults that lie west of the Wasatch, which typically have late Quaternary slip rates in the range of 0.1 to 0.2 mm/yr.

Summing the slip rates on the faults that intersect a transect extending west of Indian Hickman Canyon indicates a cumulative late Quaternary slip rate across the Stansbury fault zone of 0.39 ± 0.04 mm/yr. This value is faster than previously reported estimates, primarily because displacement across secondary traces was not included in the previous estimates. Helm (1995) concludes that the southern section of the fault, which lies west of the highest part of the range, is probably characterized by faster Quaternary slip rates than the northern section of the Stansbury fault. Considering this, and taking into account the uncertainties in the displacement data, rates in the range of 0.4 ± 0.1 mm/yr are used to characterize the average slip rate along the length of the Stansbury fault in the probabilistic seismic hazard analysis (Section 6.2).

From the scarp profiles described above, the single-event displacements are estimated to be about 1.9 m on the main fault trace (profile SF-1b) and 1.4 m and $\leq$1m on the secondary fault traces (profiles SF-2 and SF-3 respectively). This indicates a possible range of single event displacements of about 1 m, assuming the fault traces ruptured independently, to about 4 ½ m, if the primary and secondary traces all ruptured simultaneously. The Holocene faulting on the main trace appears to die out between Antelope and Indian Hickman canyons at about the latitude as the northern limit of the secondary traces. This suggests the most likely vertical displacement during the most recent event is about 2 m to 2 ½ m. The 2-m value corresponds to the displacement from profile SF-1b (1.9 $\pm$ m). The 2 ½-m value corresponds to the sum of profiles SF-2 and SF-3 divided by two events. The displacement measurements along this section of the fault are likely to be somewhat higher than the average for the entire length of the Stansbury fault. Scarp heights tend to be higher and the height of the range to the east is higher than the sections of the fault to north and south. The values considered in the probabilistic analysis for the average slip per event on the Stansbury fault range from 1 m to 4 ½ m with a preferred value in the range of 2 to 3 m (Section 6.2).

5.2 MID-VALLEY FAULTS

Two west-dipping normal faults are mapped along the center of the basin in the southern part of Skull Valley (Plate 6). Evidence of late Pleistocene activity is indicated for both fault traces, which bound Hickman Knolls and are referred to in this report as the East fault and the West fault. These faults are probably truncated by the Pass Canyon fault, but the possible continuation of the East fault to the postulated Springline fault also is considered.

Small faults identified in the area between the East fault and the West fault are interpreted to be due to secondary deformation in the hanging wall of the East fault. The structural data suggest that the site is in the stepover area between the East and West faults, but alternative fault geometries also are considered.

The results of the various site area investigations are described in Section 5.2.1. Sections 5.3.2 and 5.2.3 summarize the evidence for Quaternary faulting on the East fault and the West fault, respectively. Section 5.2.4 describes the distributive faulting in the stepover areas.

5.2.1 Results of Site Investigations

Photogeologic Interpretations of Low-Sun-Angle Aerial Photographs

The 1:20,000-scale aerial photographs greatly facilitated the geologic mapping of the Quaternary geomorphic features and bedrock areas in the site vicinity (Figure 1-3 and Plate 1). By far the dominant geomorphic features evident on the aerial photographs are shoreline erosional and depositional feature associated the transgression and regression of Lake Bonneville during the late Pleistocene. As discussed later, these features provide useful datum for constraining the amount and timing of fault displacement. None of the east-west trending shorelines that cross the site are visibly offset on the aerial photographs, indicating that, if there has been any faulting since the lake level receded about 12,000 years ago, the cumulative displacement must be very small.

The most pronounced north-south trending features that are apparent on the aerial photographs are linear ridges, which were identified on Sacks' (1993) Quaternary geologic map of Skull Valley as "Faults or fractures having small or undetermined displacement." Mapping and test pits clearly demonstrate that these features are depositional near-shore sand ridges associated with the influx of sand from Indian Hickman Creek into Lake Bonneville when it was at the Stansbury level (~22 ka to ~20 ka).

Particular attention was paid to photo lineaments that could potentially be tectonic in origin. Two basic types of lineaments are identified on Figure 1-3, lineaments within the areas of bedrock outcrop and those in areas underlain by Quaternary deposits. The bedrock lineaments, which were described in section 4, coincide with mineralized shear zones that are resistant to erosion and generally bound the ridges or occur along ridge crests on Hickman Knolls. The lineaments in the Quaternary terrain consist of linear drainages, tonal contrasts and vegetation alignments. In general these lineaments trend northward parallel to the regional slope. As shown on Plate 1, some of the lineaments may coincide with faults identified based on the seismic reflection survey. As described below, the orientation of these lineaments is considered when correlating fault picks on adjacent survey lines.

High-resolution seismic shear wave survey (Bay Geophysical Associates, 1999)
Interpretations of four seismic lines collected for this study were used to identify the location of faults in proximity to the proposed storage area site (Bay Geophysical Associates, 1999). Table 5-1, which is reproduced from their report, summarizes the sense and amount of displacement for two reflectors (Qp and Q/T) that can be traced across the entire site. These reflectors are interpreted to represent the unconformities at the base of the Bonneville alloformation (Qp) and the Quaternary/Tertiary contact.

The Qp unconformity represents the subaerial period of erosion, deposition, and soil formation that occurred between the Little Valley lake cycle, which ended about 130 ka, and the Bonneville lake cycle. The oldest Bonneville lake sediments at the site are about 28 ka. The depth of the Qp reflector calculated based the two-way-travel time and using an interval velocity of 800 ft/sec coincides with the depth of the Promontory soil in the boreholes. The calculated displacements of the Qp reflector using this interval velocity (Table 5-1) are about three times less than the displacements of the Promontory soil based on borehole data. This discrepancy is probably due to the fact the "interval velocity" represents the average velocity of the sediments between the surface the Promontory soil and not the true interval velocity at the depth of the offset. The true internal velocity at that level is undoubtedly higher than the average velocity. Given the uncertainties in the shear wave profile at the site, the calculated displacements of the Qp reflector are adjusted by a factor of 3 when assessing fault displacements and slip rates (e.g., Tables 5-3, 5-4 and 5-5).

The Q/T reflector likely represents an unconformity at the top of the Salt Lake Group. The time represented by the Q/T unconformity is not well constrained by available data. Vitric tuffs that have been collected from boreholes and trench exposures (Table 3-3) indicate a middle to

late Miocene aga (~6 to 14 Ma) for the Salt Lake Group in the site area (Appendix D).
Detailed sampling of one borehole (GMX borehole C-5, Appendix B) showed a relatively
uniform section of lacustrine deposits below the Qp unconformity/pre-Bonneville deposits and
the top of the Salt Lake Group (Q/T reflector) that correlates to the Little Valley alloformation
(~130 to 160 ka). These data suggest a minimum upper constraining age for the Q/T boundary
at this location of > 160 ka. A maximum age of approximately 4 Ma is based on the estimated
age of the underlying Salt Lake Group.

As shown in Plate 1, faults identified on the high-resolution seismic lines can be classified into
three categories based on the age of the youngest offset reflector. The oldest faults die out at or
below the Q/T reflector. The youngest faults displace the Qp reflector. An intermediate
category consists of faults that displace the Q/T reflector but do not displace the Qp reflector.

Subsurface Investigations
Subsurface stratigraphic data collected from borings, test pits, and trench exposures are used to
further evaluate the fault locations and displacements inferred from the seismic data. The
subsurface data that were collected along an east-west transect across the site subparallel to
Seismic Profile PFSF-98-A are shown on cross section D-D' (Plate 4). A more detailed cross
section across Faults F1/F3 is presented in Figure 5-4. Logs of trenches T-1 and T-2 are shown
on Plates 2 and 3, respectively.

Topographic Profile and Subsurface Data for Stansbury Cross-Valley Barrier Bar
A relatively continuous cross-valley barrier bar extends for a distance of at least 4.8 km from
near the center of Section 7, T5S, R8W to center of Section 10, T5S, R9W (Plate 1). The
approximately 2- to 2.5-m-high bar varies in width, ranging from 30 m where it has been more
extensively eroded to 90m. A longitudinal topographic profile along the crest of the bar and
transverse profiles at three locations are shown on Plate 5.

A series of three test pits (TP-14, TP-23, and TP-24) supplemented by natural exposures along
gullies provide representative stratigraphic sections through the bar at several locations. The
barrier deposits consist of well sorted, cross-bedded, clast-supported, sandy gravel. Locally
they are cemented by tufa in the upper part. The gravel deposits are overlain by interbedded
fine and very fine sand that is overlain by eolian and dune deposits.

Similar gravel bar deposits were observed in test pits TP-13 and TP-19 along the northern flank
of Hickman Knolls and in test pits TP-21 and TP-22 in the northeast part of the site study area

(NE ¼, Sec. 5, T5S, R8W, Plate 1). The latter two test pits were excavated into a bar that extends along the southern flank of the steeper escarpment to the northeast of the proposed storage site area. Thinner, eroded gravel bar deposits also were observed in TP-18 and TP-20 and Trench T-1 along the northern flank of Hickman Knolls (SW ¼ , Sec. 8, T5S, R8W).

Based on the prominent geomorphic expression, regional extent, and stratigraphic evidence that suggests the relatively continuous barrier bar west of Hickman Knolls predates the transgression to the Bonneville highstand, this feature is interpreted to mark the approximate elevation of the Stansbury shoreline, which formed between about 22 ka to 20 ka. A slightly lower Stansbury bar along the northern flank of Hickman Knolls also is indicated by stratigraphic and geomorphic relationships. An abrasion surface and tufa deposits at an elevation of 4506.4 ft near the crest of a bedrock knoll north of the main access road to Hickman Knolls (center, Section 7, T5N, R8W: Plate 1) appears to correlate with gravel bar deposits in TP-18 and TP-20 that occur at elevations of 4507 to 4508 ft. Gravel bar deposits in TP-13, TP-19, TP-20, and TP-21 are overlain by Bonneville deeper-water deposits indicating a Stansbury age for these bars. Correlation of these gravel bar deposits to the gravel bars north and west of Hickman Knolls are not well constrained. Structural relationships suggest these deposits probably correlate with the lower Stansbury bar in the vicinity of Trench T-1 rather than the higher more continuous cross-valley bar.

A series of discrete steps (in cross section) and sharp bends (in map view) in the topographic profile surveyed along the crest of the bar coincide with lineaments identified on aerial photographs (Figure 1-3) and displacements inferred from test pit data (Plate 5). Deformation of the bar across the projected fault traces generally is not constrained to a single, well-defined scarp, but rather appears to be distributed across a series of small steps within wider zones. This would be expected for a rupture propagating to the surface in unconstrained, loose gravel materials. Some of the unevenness in the surface profile also may be attributed to survey points that were measured on more eroded parts of the bar or where there are variations in the thickness of sediments mantling the bar gravel. The most reliable data for estimating possible amounts of vertical separation across these steps are provided by test pits and natural exposures where the top of gravel, or tufa formed at or near the top of gravel, are exposed. Estimated amounts of possible displacement of the Stansbury bar across individual fault traces are described in Section 5.2.3.

5.2.2   East Fault

As imaged in the proprietary seismic reflection line (line GSI-UT-34; Appendix D in Bay Geophysical Associates, 1999), the East fault is a west-dipping normal fault that includes two main traces (at shotpoints 183 and 193). Faults A1 to A4 on seismic line PFSF-98-A correlate to the westernmost trace on line GSI-UT-34 (shotpoint 193). The eastern trace on line GSI-UT-34 at shotpoint 183 correlates to a possible fault(s) between stations 400 and 600 on line PFSF-98-A. The western trace (Faults A1 to A4) coincides with prominent linear reaches of Indian Hickman Creek (Figure 1-3). The easternmost trace coincides with a topographic escarpment along the western flank of Castle Rock Knoll that truncates a Bull Lake or older age alluvial fan (Figure 3-1).

Late Pleistocene/Holocene activity is indicated for the East fault based on the following lines of evidence: (1) discrete displacements of the Qp reflector are imaged in the seismic data, (2) the Bull Lake or older age alluvial fan appears to be truncated by the fault, and (3) the Provo shoreline appears to be at a higher elevation east of the fault relative to the corresponding shoreline on Hickman Knolls.

Estimated displacements and slip rates calculated for the East fault are summarized in Table 5-3. The slip rate estimates are based on displacements of datums ranging in age from ≥160 ka to 12 ka, and thus are considered to be representative of the late Pleistocene slip rate for this fault. The central estimates of slip rates range between 0.1 to 0.3 mm/yr (Table 5-2). Uncertainty in the estimated slip rates for the East fault is attributed to a number of factors:

1. The correction factor used to convert measured displacements in the seismic data has not been calibrated with borehole data in the vicinity of the fault A picks. It is possible that velocities in the sediments overlying the Qp reflector in this area, which lies closer to the source of clastic sediments coming into the lake, would be slightly less than for finer-grained sediments further to the west where a 3 times multiplier has been assessed based on borehole data. This would result in slightly lower slip rate values.

2. The slip rates estimated based on the displacements of the Qp reflector measured in the seismic profiles would be twice the amount estimated in Table 5-3 if the displacement is averaged over a post-28 ka versus post-55 ka time period. As discussed in Section 7.2, the 55 ka time period is judged to be more representative of the late Pleistocene slip history.

3. The slip rate based on the displacement of the alluvium could be significantly less than the 0.2 to 0.3 mm/yr estimated for the fan offset if the fan is older than Bull Lake (> 160 ka).

4. The estimated range in displacement values for the Provo shoreline are based on inspection of 1:24,000 U.S. Geological Survey 7.5-minute quadrangles. Based on the spot elevations provided on these maps, the upper estimate of the possible elevation difference is fairly well constrained, but the lower limit is less certain.

To incorporate these uncertainties, we include a broader range (0.05 to 0.45 mm/yr) in the slip rate distribution used in the probabilistic hazard analyses.

5.2.3   West Fault

The West fault is a west-dipping normal fault that intersects seismic line GSI-UT-34 at approximately shotpoint 280. This fault projects beyond the western extent of the shear-wave seismic survey lines acquired for this study. The projected trace of the fault, which lies west of the bedrock outcrops, coincides with possible vertical displacements of the Stansbury cross-valley bar (Plates 1 and 5) suggesting late Pleistocene activity. Based on the apparent changes in the elevation of the surface of the bar and elevations of the top of gravel in TP-14 and a tufa sample at or near the top of gravel in the bar west of the projected fault trace, a vertical separation of the Stansbury bar across the West fault is 1 to 1.5 m (Plate 5 and Table 5-3). Based on the surface morphology of the bar the faulting occurs across a small graben and down-to-the west traces west of test pit TP-14. The fault zone aligns with linear drainages and tonal lineaments identified on aerial photographs along the western boundary of the Hickman Knolls bedrock outcrop (Figure 1-3). It may be associated with a series of northwest-trending lineaments identified by Sack (1993) in Sections 23 and 26, T5S, R8W. Most of the lineaments in this zone appear to be related to shoreline processes. One of the lineaments consists of a sharp tonal contrast that appears to cut across the topographic contours, which suggests it is not due to wave erosion and might be tectonic in origin. Based on the net vertical offset of the Stansbury Bar across the projected trace of the West fault, the late Quaternary slip rate is 0.05 to 0.07 mm/yr (Table 5-2). This slip rate, which is based on apparent displacement of a single datum, may have occurred during a single event. This estimate, therefore, is not considered very reliable. The cumulative displacement of Tertiary strata across the West fault compared to the more significant displacements across the East fault as imaged on line GSI-UT-34 suggest that the West fault at the latitude of the proposed PFSF site is a less significant fault, which is consistent with the lower calculated slip rate on the West fault.

5.2.4   Zone of Distributed Faulting

A broad zone of distributed faulting is present in the area between the East and West faults. Both west-dipping and east-dipping normal faults are imaged in the seismic data across this zone. The total cumulative displacement across individual faults within this zone is small

based on the estimated displacements of the Q/T reflector across individual faults (Table 5-1) and the limited amount of offset of Paleozoic bedrock units in Hickman Knolls (Section 4.0). Several of the faults (Faults D3, E1, E2, E3, and G2) do not appear to extend above the Q/T reflector, suggesting that there has been no late Quaternary movement on these traces. If there has been late Quaternary movement, it is less than the detection threshold of the seismic data (less than about 2 ft.). Faults A1-A4, B2, C1, D1, F1/F3, F2/F4, and H1 appear to displace or deform the Qp reflector and extend into the overlying Bonneville sediments, suggesting late Pleistocene (post-28 ka) activity on these traces. Faults B1, C2, D2, G1, and H2 may displace the Q/T reflector, but appear to die out below the Qp boundary. Bay Geophysical Associates' (1999) estimated amounts and sense of displacement based on measured offsets of the Q/T and Qp reflectors are summarized in Table 5-1.

In addition to the seismic data, drilling, trenching, and mapping data were used to constraint the location and amount of late Pleistocene deformation across individual fault traces in the vicinity of the site area.

Fault D1

The location and down-on-the-west sense of displacement interpreted for Fault D1 on Line PFSF-98-A was confirmed by borehole data (Plate 4). The unconformity at the base of the Bonneville/Promontory Soil contact appears to step down approximately 0.7 m (2.3 ft) between boreholes C-18 and C-30. Possible displacements of the contact at the top of Pre-Stansbury transgressive facies in an approximately 30 to 45 m-wide zone east of Fault D1 suggest the most recent event post dates the deposition of this unit. There is evidence for little or no vertical separation of the top of the deep-water facies unit (~24 ka), but warping and minor deformation in the overlying Bonneville sediments cannot be precluded. The stratigraphic evidence suggests that there has been at least one, and possibly two events, post 28 ka.

Alternative correlations of Fault D1 to faults imaged on lines PFSF-98-B and PFSF-98-D are permitted by the seismic data.

A prominent linear drainage (Figure 1-3) lies between boring C-18 and C-30. This north-northwest-trending drainage is well expressed between lines PFSF-98-A and PFSF-98-D. It intersects line PFSF-98-D at shotpoint 1050, directly west of a fault pick at shotpoint 1110. The fault on line PFSF-98-D exhibits a similar sense of displacement to Fault D1 on line PFSF-98-A. Correlation of fault picks between lines PFSF-98-D and Line PFSF-98-B are difficult due to the lack of good data for the western portion of line PFSF-98-D. The fault may follow a

north trend suggested by the linear drainage, in which case, it may correlate to the zone of normal faults observed in Trench T-1 (Station 61 to 64, Plate 2) and test pit TP-12 (Appendix C). The maximum vertical stratigraphic separation on the base of the Post-Little Valley sand ramp deposits (unit Q_2b in Trench T-1) across the zone of closely spaced normal faults is 0.5 to 0.7 m. The displacement on individual fractures ranges from < 4 cm to about 15 cm.

Alternatively, Fault D1 may correlate with a fault pick at shotpoint 885 on Line PFSF-98-B, across which the character of the Qp reflector changes.

Faults imaged in the deeper p-wave reflection survey (SWEC, 1997, Geosphere Midwest seismic survey) may correlate with Fault D1. Correlations between the p-wave survey and the s-wave survey are not well constrained given the lack of data in the Tertiary section overlying the bedrock surface (inferred to be an unconformity at the top of Paleozoic bedrock) that is imaged in the p-wave survey. Faults at shot point 1780 (depth 213 m) on p-wave seismic line 2 and between shot points –60 and 230 (depth of 250 to 260 m) on p-wave seismic line 3 lie in proximity (within 80 m) of the alternative locations for Fault D1 as imaged in the s-wave survey. Correlation of these two fault zones is reasonable given the similar appearance (little to no displacement of the unconformity at the Tertiary/Paleozoic bedrock contact) and gentle dip of bedding in the Paleozoic bedrock east of these faults as imaged in the p-wave survey. The lack of significant displacement of the Tertiary/Paleozoic bedrock unconformity is consistent with the interpretation of these faults as minor features within a zone of distributed secondary faulting.

E Faults

Faults imaged in the seismic data across the middle of the proposed storage area (Faults E1, E2, and E3) are imaged in the Tertiary section, but do not show evidence of post-Q/T displacement. These faults most likely correlate at depth with the zone of faulting shown on the Geosphere Midwest P-wave seismic line 2 between stations 400 and 800.

Trench T-2 (Plate 4) was excavated across Fault E1, which of the three E faults can be traced highest in the section on the seismic data (Plate 4). A detailed log of this trench is shown on Plate 3. The trench exposed the upper part of the Bonneville alloformation. Deposits in the lower part of the trench are interpreted to have been deposited during the lowstand of the Stansbury oscillation approximately 20 to 22 ka. These deposits are overlain by post-Stansbury transgressive and Bonneville deep-water facies. A thin veneer of post-Provo eolian and reworked eolian sediments overlie the Bonneville deep-water sediments. The trench clearly

demonstrated the absence of discrete faults in sediments within 6 m (20 ft) of the ground surface across the projected trace of Fault E1. Boring data collected across this fault and Fault E2 also show evidence of no deformation of Bonneville lake cycle sediments. Numerous, vertical to subvertical fractures were observed in the upper deep-water sediments in Trench T-2. These fractures cannot be traced into the coarser deposits in the bottom of the trench, and there is evidence of no displacement of thin clay marker beds that extend across the projected trend of the fractures at depth. The fractures are principally oriented north-northwest (see rose diagram on Plate 3). The origin of the fractures is uncertain. They may have formed in response to nontectonic (e.g., isostatic unloading, periglacial shrink-swell) or tectonic (i.e., strong ground shaking, warping and distributed faulting at depth) processes.

The E faults are best correlated with faults on line PFSF-98-C based on similarities in the overall signature and seismic character of the faults and adjacent strata. This correlation suggests a northwest trend for the faults consistent with the general trend of gravity in the site area.

F Faults

Four faults forming two couplets (F1/F3 and F2/F4) are well imaged in seismic line PFSF-98-A. These faults are correlated with similar faults on line PFSF-98-D between shotpoints 197 and 369, and based on this trend would correlate with a prominent down-on-the-west fault imaged on line GSI-UT-34 at shotpoint 227.

Faults F1 and F3 are west-dipping and east-dipping faults, respectively, that bound a small graben that is well imaged in seismic line PFSF-98-A. Post-Qp displacement on these faults is evident in the seismic data. A series of boreholes were drilled across Faults F1 and F3 to confirm the location and amount of late Pleistocene deformation on these faults.

A geologic cross section based on closely spaced boreholes across Faults F1 and F3 is shown on Figure 5-4. The boring data support the seismic interpretation of a graben with post-Promontory Soil displacement. The unconformity at the base of the Bonneville alloformation/Promontory Soil contact appears to step down-to-the west across two traces that are inferred to represent Fault F1 and step up-to-the-west across two traces that are correlated to Fault F3. Displacements across individual traces and the net displacement across the entire graben are tabulated on Figure 5-4. Stratigraphic relationships interpreted from the borehole data indicate that there likely have been two surface ruptures on this fault that post-date the transgression of the lake in this area (~28 ka). An approximately 1 m-thick sand and gravel

unit is present in the basal part of the Stansbury transgressive facies west of the F1 fault traces. This unit may have been deposited on the downthrown side of a scarp that resulted from the initial faulting event on Fault F1. This unit has subsequently been displaced across the east-dipping fault traces. Stratigraphic units in the upper part of the cross section show evidence for little or deformation across discrete fault traces. However, broad warping of the upper units cannot be precluded.

Fault F2 is a down-on-the-west fault that exhibits good evidence of post-Qp displacement on both seismic lines PFSF-98-A and D. Fault F4, a down-on-the-east trace cannot be correlated to line PFSF-98-D. To some degree, linear reaches of the present drainages do coincide with the projected trends of the F faults.

The projected trends of the F faults appear to correlate with two well expressed bedrock lineaments in Hickman Knolls. These lineaments coincide with resistant ridges of reddish brown, silicified, altered dolomite breccia containing sheared chert stringers (Section 4.0). The Stansbury bar also appears to be displaced across the F faults. The top of gravel appears to step down-on-the-west approximately 0.6 m (1.9 ft) across the zone between TP-23 and TP-24 (Plate 5).

H Faults

The westernmost fault imaged on line PFSF-98-A is a down-on-the-east normal fault that appears to displace the Qp reflector. This fault appears to align with a strong linear drainage and small displacements in the Stansbury bar west of TP-23. Another down-on-the-east fault trace likely occurs just east of TP-14 where the Stansbury bar is breached by a modern drainage. The Stansbury bar swings sharply to the south in this region and is breached by a number of small drainages. The western boundary of this apparent downdropped zone may correlate with an antithetic (down-on-the-east) fault trace imaged in line GSI-UT-34 at shotpoint 260.

6.0 POTENTIAL EARTHQUAKE GROUND MOTIONS

The potential for strong ground shaking at the site due to earthquakes is assessed based on a probabilistic seismic hazard analysis (PSHA). Section 6.1 describes the PSHA methodology used in this study. The characteristics of earthquake sources (active faults and seismic source areas) used in the hazard analysis are described in Section 6.2 and the results are presented in Section 6.3. Section 6.4 compares the PSHA results to ground motion estimates based on a deterministic analysis.

The design basis ground motions for the proposed PFSF site were arrived at using a deterministic approach, consistent with Part 72.102 and 10 CFR Part 100 for nuclear power plants. A deterministic approach assumes that the maximum credible earthquake on all capable sources will occur at the closest approach to the site. The controlling source results in the largest ground motions at the site and determines the SSE ground motions. The deterministic design basis ground motions at the proposed PFSF site were presented in the SAR (Section 2.6.2). Deterministic approaches do not incorporate any information related to the frequency of earthquake occurrence, nor do they allow for the explicit inclusion of uncertainties in the location, size, or ground motions associated with earthquakes. For these reasons, Part 100 has been revised (Part 100.23) to allow for probabilistic methodologies to be used to arrive at design basis ground motions. Part 72 has not yet been revised, but the rulemaking plan (SECY-98-126) indicates that probabilistic approaches should likewise be used for dry cask storage installations. Therefore, we have conducted a probabilistic seismic hazard analysis that incorporates the findings of the field studies and associated uncertainties. To evaluate the potential for fault displacement at the site, a probabilistic fault displacement analysis was also conducted (Section 7).

6.1 PSHA METHODOLOGY

6.1.1 Probability Level of Interest

Probabilistic seismic hazard analyses result in "hazard curves" that express the probability (or annual frequency) of exceeding various levels of ground motion. Lower probability levels are associated with progressively higher levels of ground motion. As such, the probability levels express the degree of conservatism in the ground motions to be used for design. The NRC recommends that a risk-informed graded approach to seismic design be used that takes into account the consequences of the possible failure of a system in arriving at an appropriate probability level. The NRC staff recognizes the value of this approach in its evaluation of the request for exemption to Part 72.102(f)(1) Seismic Design Requirement for Three Mile Island

Unit 2 Independent Spent Fuel Storage Installation (SECY-98-071), and in its Rulemaking Plan for revision to Part 72 (SECY-98-126). The Commission stated that "…ISFSI's which do not involve massive structures, such as dry storage casks and canisters, the required design earthquake will be determined on a case-by-case basis…" (45 FR 74697 [1980]). In its Rulemaking Plan, it is stated that the "NRC staff believed that a major seismic event at an ISFSI storing spent fuel in dry casks or canisters would most likely have minor radiological consequences compared with a major seismic event at an NPP, spent fuel pool, or single massive storage structure" (SECY-98-126). The NRC, therefore, recommends that a probabilistic approach be taken and that the probability levels appropriate to the design of a dry cask storage system should be higher (i.e., ground motions lower) than those for a nuclear power plant.

Until the Part 72 rulemaking is completed, there is only indirect guidance from the Staff regarding the appropriate probability level for seismic design. In the exemption to Part 72.102, the seismic requirement (design earthquake or DE) for the TMI-2 ISFSI was 0.35g peak ground acceleration, corresponding to a ~5 x 10^{-4} per year probability level (or ~2,000 year return period). The deterministic SSE at the INEL site was assessed to be 0.56g. In arriving at their decision, the Staff considered the appropriateness of a probabilistic methodology and a risk-informed graded approach. They noted that such a graded approach, which expresses the relative risk posed by the ISFSI, has been developed in DOE Standard 1020 "Natural Phenomena Hazards Design and Evaluation Criteria for Department of Energy Facilities." The standard takes a graded approach to design critical facilities, requiring facilities with greater accident consequences to use higher design requirements for phenomena such as earthquakes and tornadoes. They conclude, "Dry spent fuel storage facilities such as the TMI-2 ISFSI are PC 3 and must have a design earthquake equal to the mean ground motion with a 2,000-year return period. Considering the minor radiological consequences from a canister failure, and the lack of a credible mechanism to cause a failure, the staff finds that the DOE approach of using the 2,000-year return period mean ground motion as the design earthquake for dry storage facilities is adequately conservative."

The staff also note that the 10 CFR Part 60 Design Basis Event rulemaking also adopts a graded approach. In this approach, a design basis event is based on a probabilistic, risk-graded methodology. For seismic events, the staff has accepted DOE's two-tiered approach toward designing Part 60 SSCs. Those SSCs with potential failure consequences less than the public dose limit of 10 CFR 20.1302(a)(1), 1 mSv (100 mrem), must withstand the 1,000-year return period mean ground motion. Analysis of the consequences associated with a cask failure at the

PFSF are less than the 100 mrem dose limit, thus suggesting that the 1,000-year return period is appropriate.

Based on the above arguments for a risk-informed graded approach, we conclude that an appropriate design probability level for the PFSF site is 5×10^{-4} (2,000-year return period). The design basis ground motions presented in the SAR were based on a deterministic approach and did not incorporate the uncertainties associated with seismic sources, recurrence, or attenuation relationships. The PSHA presented herein does include these uncertainties explicitly, including the findings of the fault studies. The deterministically defined design basis ground motions are compared with the 2,000-year ground motions derived from the probabilistic approach, and are shown to be conservative relative to this criterion.

6.1.2   Implementation of PSHA Methodology in This Study

Basic Model

The methodology used for the probabilistic assessment of ground motion hazard at the Skull Valley site follows that outlined for the Yucca Mountain project as described in USDOE (1997) and CRWMS M&O (1998). The methodology for a PSHA was first proposed by Cornell (1968, 1971). The basic components of the PSHA for ground motion hazard are shown schematically on Figure 6-1. The components are as follows.

1. The sources of potentially damaging future earthquakes are identified. The types of sources typically identified are specific geologic structures, such as faults, and areal source zones representing tectonic provinces or zones of seismicity.

2. The frequency of earthquake occurrence in each source is assessed. This includes an evaluation of the maximum event that a source can produce. The probability distribution of distance from individual earthquakes to the site is also defined by specifying the appropriate spatial distribution model for earthquake location on the seismic source.

3. Appropriate ground motion attenuation models are selected for estimating site ground motions from each source. The estimates include both the expected levels of ground motion and the variation about the expected value that any recording may exhibit.

4. Using the probabilistic models developed in steps (2) and (3), a relationship between ground motion level and probability (frequency) at which it is exceeded is developed, defining a *hazard curve*. Specific ground motion levels for design can then be chosen by selecting an appropriate probability level.

The mathematical formulation used for PSHA typically assumes that the occurrence of damaging earthquakes can be represented as a Poisson process. Under this assumption, the probability that a ground motion parameter, Z, will exceed a specified value, z, in time period t is given by:

$$P(Z > z| \, t) = 1 - e^{-v(z) \cdot t} \leq v(z) \cdot t \qquad \text{(6-1)}$$

where $v(z)$ is the average frequency during time period t at which the level of ground motion parameter Z exceeds value z at the site from all earthquakes on all sources in the region. The inequality at the right of Equation (6-1) is valid regardless of the probability model for earthquake occurrence, and $v(z) \cdot t$ gives an accurate and slightly conservative estimate of $P(Z > z)$ for probabilities of 0.1 or less, if $v(z)$ is the appropriate average value for time period t.

The frequency of exceedance, $v(z)$, is a function of the frequency of earthquake occurrence, the randomness of size and location of future earthquakes, and the randomness in the level of ground motion they may produce at the site. It is computed by the expression:

$$v(z) = \sum_n \alpha_n(m^0) \int_{m^0}^{m^u} f(m) \left[\int_0^\infty f(r|m) \cdot P(Z > z|m,r) \cdot dr \right] \cdot dm \qquad \text{(6-2)}$$

where $\alpha_n(m^0)$ is the frequency of earthquakes on source n above a minimum magnitude of engineering significance, m^0; $f(m)$ is the probability density of earthquake size between m^0 and a maximum earthquake the source can produce, m^u; $f(r \,|\, m)$ is the probability density function for distance to an earthquake of magnitude m occurring on source n; and $P(Z > z \,|\, m,r)$ is the probability that, given an earthquake of magnitude m at distance r from the site, the peak ground motion will exceed level z.

Section 6.2 describes the implementation of steps (1) and (2) for this project: identification of the seismic sources that may produce earthquakes significant to ground motion hazard at the site, and for each source an assessment of the frequency of earthquake occurrence, $\alpha_n(m^0)$, the maximum earthquake the source can produce, m^u; the distribution of earthquake sizes, $f(m)$, and the spatial distribution of earthquakes on the source. Section 6.3 describes the implementation of step (3): selection of appropriate ground motion models for assessing the probability of exceeding specified ground motion levels as a function of magnitude and distance, $P(Z > z \,|\, m,r)$. Section 6.4 describes the implementation of step (4), computation of the hazard at the site.

Assessment of Scientific Uncertainty

The PSHA methodology outlined on Figure 6-1 and defined by Equation (6-2) is formulated to represent the randomness inherent in the natural phenomena of earthquake generation and seismic wave propagation. The randomness in a physical process has come to be called *aleatory* uncertainty (SSHAC, 1997). In all assessments of the effects of rare phenomena, one faces uncertainty in selecting the appropriate models and model parameters because the data are limited and/or there are alternative interpretations of the data. This uncertainty in knowledge has come to be called *epistemic* uncertainty (SSHAC, 1997).

The uncertainty assessment was performed using the *logic tree* methodology. The logic tree formulation for seismic hazard analysis (Kulkarni and others, 1984; Coppersmith and Youngs, 1986; Electric Power Research Institute, 1988; National Research Council, 1988) involves setting out the sequence of assessments that must be made in order to perform the analysis and then addressing the uncertainties in each assessment sequentially. Thus, it provides a convenient approach for breaking a large, complex assessment into a sequence of smaller, simpler components that can be addressed more easily.

Figure 6-2 shows an example of a logic tree. The logic tree is composed of a series of nodes and branches. Each node represents a state of nature or an input parameter that must be assessed to perform the analysis. Each branch leading from a node represents one possible alternative interpretation of the state of nature or parameter being evaluated. If the variable in question is continuous, it can be discretized at a suitable increment. The branches at each node are intended to represent mutually exclusive and collectively exhaustive states of the input parameter. In practice, a sufficient number of branches are placed at a given node to represent the evaluator's uncertainty in estimating the parameter.

Probabilities are assigned to each branch that represent the expert's evaluation that the branch represents the correct value or state of the input parameter. These probabilities are conditional on the assumption that all the branches leading to that node represent the true state of the preceding parameters. Because they are conditional probabilities for a mutually exclusive and collectively exhaustive set of values, the sum of the conditional probabilities at each node is unity. The probabilities are based on scientific evaluations because the available data are too limited to allow for objective statistical analysis, and because scientific evaluation is needed to weigh alternative interpretations of the available data. The logic tree simplifies these assessments, because the uncertainty in each parameter is considered individually, independent of prior evaluations. The nodes of the logic tree are sequenced to express conditional aspects or dependencies among the

parameters and to provide a logical progression of evaluations from general to specific in characterizing the input parameters for PSHA.

The probabilities (relative weights) assigned to the branches at a node of the logic tree represent one of two types of probability assessments. For the first type, the branches at a node define the range of parameter values; the associated weights define the probability distribution for the parameter. For example, estimates of the slip rate on a fault are uncertain because of uncertainties in the amount of displacement of a particular geologic unit across the fault and the age of the unit. The probability distribution for a parameter value may be characterized in several ways: as a discrete distribution defined by a preferred value and a range of discrete higher and lower values; a cumulative distribution based on scientific evaluations; or by a mean estimate and an uncertainty estimate similar to a normal or log-normal statistical distribution. Examples of these means of characterization are given below. Continuous distributions can be discretized to form logic tree branches following a number of approaches. Keefer and Bodily (1983) showed that most distributions can be represented reliably by three values: the median estimate (50th percentile), assigned a weight of 0.63, and a higher and lower value, each given weights of 0.185, which represent the 5th and 95th percentiles (± 1.645 standard deviations for a normal distribution). They list other discretization schemes for more points. Another four-point representation of a normal distribution is described in EPRI (1993, Chapter 9). Miller and Rice (1983) present a number of discrete approximations to subjectively defined, continuous cumulative distributions.

In some instances, the uncertainty in assessing parameters can be estimated using formal statistical techniques. In these cases, continuous parameter distributions developed from statistical estimation procedures can be discretized for use in a logic tree formulation.

A second type of probability assessment, to which logic trees are particularly well suited, is indicating a relative preference for, or degree of belief in, alternative hypotheses. For example, the sense of slip on a fault may be uncertain—two alternatives might be strike-slip or reverse-slip. Based on the pertinent data, a relative preference for these alternatives can be expressed by weights in the logic tree. A very strong preference (i.e., the data strongly support one interpretation over the other) for one alternative over the other usually is represented by weights such as 0.9 and 0.1. If there is no preference (i.e., the data equally support either alternative) for either hypothesis, they are assigned equal weights (0.5 and 0.5 for two hypotheses). Increasing the weight assigned to one alternative from 0.5 to 0.9 (or more) reflects increasing support in the data for that alternative. Because the relative weights ultimately are the result of scientific evaluations based on available information, it is important to document the data and interpretations that led to

the characterization of parameter values and their relative weights so that the process can be reviewed by others.

The example logic tree shown on Figure 6-2 characterizes the uncertainty in assessing the magnitude of paleoearthquakes that have occurred on a fault on the basis of dip-slip offsets observed in a trench placed across the fault. (Such assessments may be one means of characterizing the maximum magnitude for a seismic source.) There may be multiple sources of uncertainty in the assessment. Stratigraphic relationships in the trench walls may be somewhat ambiguous so that the amount of dip-slip displacement can be estimated only within a factor of two (e.g., 1.0 to 2.0 meters). One may also be uncertain about the existence of a significant component of lateral slip, which would indicate whether the fault is primarily a normal fault or an oblique-normal fault having a ratio of strike slip to dip slip in the range of 1:1 to 1.5:1. In addition, there is the uncertainty in whether the observed slip is more representative of the maximum slip during the paleoearthquake or the average slip.

The logic tree shown at the left of Figure 6-2 captures these uncertainties. The required interpretations in the logic tree usually are ordered from general to specific. If one interpretation depends on the state of another unknown, then it is placed to the right of that assessment in the logic tree. In this example, the total amount of fault offset is dependent on whether the fault is a normal fault or an oblique-normal fault. In addition, the evaluation of whether the observed displacement is representative of the maximum or the average displacement may also depend on the style of faulting. The trench may have been placed in an area where the fault scarp was most pronounced, indicative of maximum vertical displacement. However, this may not be the area of maximum slip if the fault is oblique-normal. Because these two interpretations are made more easily given knowledge of the style of faulting, the node for interpretations of the style of faulting is placed first (to the left) in the logic tree. The order of the interpretations is dictated primarily by convenience in dealing with dependencies in the characterization. After the logic tree is constructed, the order of the nodes can be changed.

For the example shown on Figure 6-2, the evaluation of the assessor is that the interpretation of normal faulting is preferred slightly (0.6) to the interpretation of oblique-normal faulting (0.4). In actual interpretations, the assessor documents the reasons for this evaluation.

The next level of characterization in the example addresses the amount of displacement. The stratigraphic relationships indicate from 1.0 to 2.0 of offset. The interpretation of these data may favor displacements in the range of 1.0 to 1.5 but allow for as much as 2.0 meters. Thus, if the

fault is a normal fault, the distribution for the observed offset may be specified by three discrete values: 1.0, 1.5, and 2.0 m. The probabilities (relative weights) assigned to these values are 0.4, 0.4, and 0.2, respectively, reflecting that the data more strongly support displacements of 1.0 to 1.5 m.

If the fault is considered an oblique-normal fault, then the observed offsets must be increased to account for unmeasured strike-slip offset to obtain the net slip on the fault plane. The factor of increase is 1.4 for a 1:1 strike-sip/dip-slip ratio, and 1.6 for a 1.5:1 strike-sip/dip-slip ratio. In this example, it is considered twice as likely that the strike-slip to dip-slip ratio is closer to 1:1 than to 1.5:1. Thus the factors are given relative weights of 0.67 and 0.33. The evaluation of the strike-slip to dip-slip ratio is added to the logic tree after the branch for oblique-normal faulting. The evaluation is unnecessary along the normal faulting branch. There the distributions for the amount of net slip are assumed to be equal to those developed for normal faulting multiplied by the appropriate factor.

The final evaluation is whether the observed offsets represent maximum displacements or average displacements. This evaluation is important because separate empirical relationships between magnitude and fault offset are given for maximum and average displacement (e.g., Wells and Coppersmith, 1994). This evaluation is made conditionally on which sense of slip is assumed to be correct--that is, the probability that the observed offset is a maximum given normal faulting is a separate evaluation from the probability that it is a maximum displacement given oblique-normal faulting, and the two probabilities do not have to be equal. In the example the data strongly support the interpretation that the observed displacements represent maximum (0.8) rather than average (0.2) values if the style of faulting is deemed normal. If the fault is considered oblique-normal, then the maximum and average displacement is considered to be equivocal, and the two alternatives are given equal weight.

Each end branch on the right-hand side of the logic tree shown at the left of Figure 6-2 specifies one estimate for the magnitude of the paleoearthquake. The magnitude estimate is obtained using the appropriate empirical relationship between fault displacement (either average or maximum) and moment magnitude given by Wells and Coppersmith (1994). Their relationships for normal faulting earthquakes were used for the normal style of faulting; their relationships for strike-slip faulting were used for the oblique-normal style of faulting. The resulting magnitudes are listed along the right side of the logic tree. The probability that the magnitude for the paleoearthquake will take on any particular value is equal to the joint probability of the set of parameters (branches) leading to that assessment. These probabilities are given in parentheses next to the magnitude

assessments. The characterization in the logic tree specifies a discrete distribution for the magnitude of the paleoearthquake. This distribution is shown at the right of Figure 6-2 in discrete density and cumulative forms.

The process illustrated above for characterizing the magnitude of paleoearthquakes was used to quantitatively express the uncertainty in the seismic source and ground motion attenuation characterization for ground shaking hazard. These assessments are described in Sections 6.2 and 6.3.

6.2   SEISMIC SOURCE CHARACTERIZATION

Seismic sources include all structures that have some potential for causing strong ground shaking at the PFSF. The seismic source model developed for this study includes two types of sources: (1) *fault-specific sources,* which include mapped late Quaternary faults within about 100 km of the site, and (2) *seismic source zones* to account for seismicity that cannot be attributed to fault-specific sources included in the model (Figure 6-1). Different approaches are used to characterize these two types of sources as discussed below.

6.2.1   Fault Sources

Active faults within 100 km of the proposed PFSF site (Plate 7) are listed in Table 6-1. These faults, excepting the recently identified East and West faults, are described in the previous SAR submittal (SWEC, 1997). Faults from this group that are included as fault sources in the seismic source model for this analysis are judged to be capable of generating magnitude 5 or larger earthquakes and, based on published reports, are inferred to have had multiple late Quaternary displacements. Several faults that are known or suspected to have had Quaternary displacement, but are not reported to exhibit evidence of late Quaternary displacement, are not included as fault-specific seismic sources. The rate of slip on these faults is too low to have a significant effect on the ground motion hazard at the site. Relatively short (<10 km) faults that lie at distances greater than 25 km also would not contribute significantly. Earthquakes that occur on Quaternary or suspected Quaternary faults that are not included as fault sources are modeled as part of the seismic source zones.

Seismic sources that might make a significant contribution to the seismic hazard at the PFSF (either because they have a relatively high rate of activity and/or because they are close to the site) are characterized in greater detail than sources far from the site. These include the Stansbury fault, the East Cedar Mountains fault, and the mid-valley faults (East fault, West fault, and postulated Springline fault) (Plates 6 and 7). Regional structural cross sections and

alternative structural models for these faults as presented in Section 2.0 and paleoseismic data discussed in Section 5 provide the basis for our characterization of these local fault sources.

6.2.1.1 Fault Source Characterization Parameters

The logic tree used to characterize fault sources is shown on Figure 6-3. The key parameters used to define the seismic hazard potential of significant crustal fault seismic sources are: total fault length and plan view geometry; probability of activity; maximum magnitude; and recurrence parameters. The assessment of these parameters are based on consideration of the maximum rupture length of faults, seismogenic crustal thickness and downdip geometry that can be used to estimate downdip width, and slip rates. The range of values and relative weights applied for each of these parameters in the probabilistic hazard analysis are provided in Table 6-2.

Total Fault Length and Plan View Geometry

Discontinuous faults are generalized as a single continuous trace consisting of one or more straight line segments, so that the average source-to-site distance and total length of the modeled fault are consistent with the mapped fault.

Probability of Activity

The assessment of activity for crustal faults reflects the judgment of the likelihood that the structure is seismogenic, or active, within the present tectonic regime and will, therefore, localize seismicity above the levels occurring randomly within the regional source zones. Faults for which there is evidence for late Quaternary (approximately the past 780 ka) are assumed to be associated with past seismogenic fault displacements [probability of activity = 1.0]. Faults for which there is questionable evidence for late Quaternary activity or that have limited downdip extent (i.e., may not extend to seismogenic depth) are assigned a probability of activity of less than 1.0.

Maximum Earthquake Magnitude

The assessment of maximum magnitude for fault sources is based on empirical relationships between magnitude and rupture length, magnitude and rupture area, magnitude and single event displacement (if data are available for the maximum and/or average displacement per event) (Wells and Coppersmith, 1994); the relationship of Anderson and others (1996) between magnitude, rupture length, and slip rate; and the relationship between magnitude, rupture length, and maximum displacement (Mason, 1996). Where the appropriate data are available, all of these techniques were used. The individual techniques were assigned relative weights

that reflect the combined weights of expert panel members who characterized the seismic source parameters for the Yucca Mountain PSHA (CRWMS, 1998). The weights assigned to the various empirical methods varied among the different experts. However, when viewed collectively, the judgements of the eighteen panel members indicate that the most weight is given to relationships based on rupture length and/or rupture area. These two methods received about equal weight with the rupture length relationship being favored slightly over the rupture area relationship. The relationship based on rupture length plus slip rate received the lowest weight. Assigned weights for this method ranged from 0 to 0.4 with the collective weight being less than or about equal to 0.1. Relationships based on displacement (either maximum displacement or average displacement) were considered less stable than those based an rupture length and area and also were assigned a low weight that was only a little higher than the weight assigned to the relationship based on rupture length plus slip rate. If displacement data are available, the relative weights assigned to the methods for estimating maximum magnitude are: magnitude versus rupture length [0.4]; magnitude versus rupture area [0.35]; magnitude versus displacement [0.15]; magnitude versus rupture length and maximum displacement [0.05]; and magnitude versus rupture length and slip rate [0.05]. When using displacement to estimate magnitude, average displacement is considered to be a more stable indicator of the size of the earthquake than maximum displacement, which only occurs along a very short length of the total rupture. Given the displacement method, the relation based on average displacement is assigned a weight of 0.7 and the one based on maximum displacement is assigned a weight of 0.3. If displacement data are not available, the method relating magnitude to rupture length and slip rate is assigned a weight of 0.1 and the remaining weight is assigned equally between the other methods.

The maximum magnitude distribution includes alternative rupture scenarios as described for each fault source and reflects the postulated maximum rupture dimensions based on combinations of rupture length and width. The maximum rupture length depends on the total fault length and on the length of the longest part of the fault that is expected to rupture during a single event. Various criteria are used to assess possible rupture segmentation scenarios for independent fault sources. Rupture of the total fault length is generally considered; for long faults this option is given relatively low weight especially if paleoseismic data on recency and recurrence suggest multiple rupture segment scenarios are more likely. For short faults, 100 percent of the total fault length commonly is given a probability of 1. Paleoseismic data regarding the timing and dimensions of previous surface ruptures are used where available to delimit rupture segments. Geometric and other geologic constraints also are considered in assigning weights to various possible rupture scenarios. Down-dip width is computed from

fault dip, thickness of the seismogenic zone, and limitations imposed by fault geometries where two faults intersect.

Seismicity data indicate that the largest historical earthquakes in the Basin and Range province occurred on 45 to 65 degree dipping normal faults that nucleated at depths of about 15 km (Smith and others, 1985). All the faults included in the seismic source model are high-angle normal faults. We represent the uncertainty in the fault dip by considering three equally likely values of 45, 55, and 65 degrees.

Depth to the base of the seismogenic zone was based on depth distributions of seismicity in the region. Figure 6-4 shows east-west cross sections of the focal depth distribution of well located earthquakes (depth error < 2 km) in the region. The data indicate that most of the earthquakes occur shallower than about 18 km, with some as deep as 25 km. We consider the thickness of the seismogenic crust to be uncertain within the range of 15 to 20 km. The discrete probability distribution of 15 km [0.4], 18 km [0.4], and 20 km [0.2] is used to express this uncertainty. The depths of 15 and 18 km are favored because of the typical depth of large Basin and Range earthquakes and nearly all of the seismicity occurs shallower than 18 km.

Slip Rate

Fault slip rate provides a fundamental constraint on the average rate of seismic moment release and earthquake recurrence. Slip rate has the advantage of spanning a longer time period than the historical record, but there can be uncertainties both in measuring displacement and determining the ages of geologic units displaced. To the extent possible, estimated slip rates are based on published slip rates. Where reported rates are not available, slip rates (with wider uncertainty) are based on analogy with other mapped faults and/or by inferring the likely ages and amount of displacement based on reported descriptions of the faults.

Earthquake Recurrence Models

Earthquake recurrence is represented in terms of the rate of seismic activity and the relative frequency of various magnitude earthquakes. Earthquake recurrence for fault sources is assessed based on the slip rate on the fault as converted to seismic moment rate using fault area and from estimates of paleoseismic recurrence intervals when available.

The geologically derived seismic moment rate is used to translate slip rate into earthquake recurrence rate by partitioning the moment rate into earthquakes of various magnitudes according to a recurrence relationship (e.g., Anderson, 1979). Three general types of recurrence

relationships have been proposed: (1) truncated exponential relations that mimic the behavior of recorded earthquakes in a region (e.g., Gutenberg and Richter, 1954); (2) a characteristic earthquake recurrence model (Youngs and Coppersmith, 1985) in which there is a greater tendency for earthquakes close to the maximum to occur than is predicted by seismicity-based exponential relations; and (3) relations that attribute all of the moment release on faults to earthquakes close to the maximum (Wesnousky, 1986). Each of these relationships were used in the probabilistic hazard analysis with relative weights of [0.22], [0.65], and [0.13] respectively. The assigned weights represent the average of the subjective judgements regarding the appropriate recurrence model for fault sources made by experts for the Yucca Mountain PSHA (CRWMS, 1998). The truncated exponential and characteristic magnitude distributions require a b-value to define the frequency of smaller earthquakes. The b-value obtained from the analysis of the regional seismicity (Section 6.2.2.1) was used for characterizing the earthquake recurrence models for the faults.

6.2.1.2 Fault Characterization

Sixteen fault sources are included in the seismic hazard analysis (Plate 6, Table 6-1, and Figure 6-3). The fault parameters used to characterize these sources are summarized in Table 6-2 and described below. Maximum magnitude distributions for individual fault sources are shown on Figure 6-6.

Mid-Valley Faults (Skull Valley)

Quaternary activity has been documented on a zone of faults within the southern Skull Valley that includes the East fault and the West fault. A similar fault, the postulated Springline fault has been inferred in the northern part of Skull Valley (Rigby, 1958; Hood and Wadell, 1968; Helm, 1995). Quaternary activity has not been documented for this fault, but based on analogy to the mid-valley faults in the southern part of the valley, the postulated Springline fault is assigned a probability of activity of 0.8 in this analysis. The East, West, and postulated Springline faults are collectively referred to as the mid-valley faults in this study. Alternative structural models (see Section 2.0 and Plate 6) that allow the possibility that some of these faults are linked or coalesce at depth, and could rupture together during individual earthquakes are considered for these fault sources. A logic tree summarizing the fault sources implied for each of these models is given in Figure 6-5.

The first node of the logic tree addressees the preference for the two alternative structural models presented in Section 2.0. These models chiefly reflect a difference in the assessment of the geometry and seismogenic capability of the West fault. In both models the East fault is

included as active fault source that may, in some scenarios be linked along strike with the postulated Springline fault. Structural model A, in which the West fault splays from the East fault in the vicinity of Johnson Pass, best fits the available geologic and gravity data and thus, is given significantly more weight [0.8]. The alternative model B, which is given a weight of 0.2, allows for a longer West fault and captures the uncertainty in the southern extent of this fault.

Assessments of the seismogenic capability of the West fault are dependent on the structural model. In model A, the West fault may or may not be an independent seismic source depending on the geometry of the fault and possible intersection with the East fault at depth. Given the uncertainty in the geometries of these faults at depth, the probability of the West fault being an independent seismic source (i.e., it does not coalesce with the East fault above seismogenic depth) is assigned a weight of 0.5. In model B, the West fault is judged to be an independent fault source with a probability of 0.7. The higher weight given to the likelihood the fault is a seismic source is based on the structural relationships that require a fault between elevated bedrock in Hickman Knolls and the deep part of the basin, and evidence for late Pleistocene activity on the West fault. Lower weight [0.3] is given to the possibility that Hickman Knolls is a detached bedrock slide (i.e., is rootless), thus, obviating the need for a block-bounding fault to the west (see discussion in Section 4.4).

The second node of the logic tree addressees the likelihood that the East fault and the postulated Springline fault are linked along strike. A possible structural boundary between the northern and southern parts of Skull Valley is suggested by structural and gravity data. Helm (1995) noted that the Pass Canyon cross fault and a fault segment boundary along the Stansbury fault coincide with a regional alignment of tectonic features in the Oquirrh, Wasatch, and Uinta Mountains. The apparent truncation of Salt Mountain along this trend combined with gravity data that indicate the formation of two distinct depocenters in the northern and southern parts of the basin suggest that this structural trend persists across Skull Valley. This, in addition to the lack of geomorphic expression of continuity between the East and postulated Springline faults, is the basis for giving low weight [0.3] to the possibility the two faults are linked and higher weight [0.7] to the possibility they are independent fault sources.

Maximum rupture length scenarios for each of the proposed fault sources are summarized in Table 6-3. Postulated rupture segment boundaries are shown on Plate 6. Weights assigned to maximum rupture lengths (Table 6-2) reflect our judgment in the validity of the alternative segmentation models. The assessment of maximum magnitude distributions for the alternate

fault sources are shown on Figure 6-6. These distributions reflect the postulated rupture dimensions based on combinations of rupture lengths and widths.

The slip rate distributions used for the individual fault sources (Table 6-2) vary depending on the structural model. Slip rate estimates for the East and West faults derived from paleoseismic data, which are discussed in Section 5.2, provide the basis for estimating the slip rate values used for the mid-valley faults. Generally, the highest weight is given to the central estimates, with less weight given to the end member values that capture the uncertainties in paleoseismic estimates. There is no independent slip rate data for the postulated Springline fault. In cases where the Springline fault is modeled as a separate source, it is given a slip rate distribution comparable to the East fault with weights more evenly distributed to reflect greater uncertainty. Slightly higher weight is given to higher slip rates in models in which the West fault coalesces with the East fault at depth and is treated as a single fault source (with or without linkage to the Springline fault).

Stansbury Fault

At its closest approach, the main trace of the Stansbury fault is 9 km west of the east border of the proposed PFSF site (Plate 6). The Stansbury fault dips to the west. A discussion of the nature and rate of Quaternary deformation on this fault is given in Section 5.1. The fault has a total length of 73 km, extending from the northern end of the Stansbury Mountains near the village of Timpie, to Lookout Pass at the southern end of the Onaqui Mountains (Plate 6). The fault sections identified by Helm (1995) are used herein with minor modifications. The fault sections include a 24-km-long section from Timpie south to Pass Canyon (Section "A"), and a 23-km-long section from Pass Canyon to Johnson Pass (Section "B"). In addition, we consider the possibility of additional fault sections south of Johnson Pass. The mapped fault trace and linear range front between Johnson Pass and The Dell, the substantial relief of the Onaqui Mountains, and the fault trace at the southern end of the range mapped by Sack (1993) all suggest the fault may continue to the south. We identify fault section "C", which extends from Johnson Pass to The Dell and is 9 km long. We also consider fault section "D", which extends from The Dell to Lookout Pass and is 17 km long (Plate 6).

We consider five rupture scenarios for the maximum-magnitude earthquake that incorporate various combinations of the four fault sections noted above. Because of the prominence of fault scarps across late Quaternary alluvial deposits along the Stansbury fault between Pass Canyon and Johnson Pass, as well as the proximity of this section, each of the scenarios includes rupture of section "B". The relatively short rupture of 23 km, in which section "B"

ruptures alone, is given a low weight [0.1], because it is likely that the maximum earthquake includes rupture along at least one other section. Scenarios that include rupture of section "B" and an adjacent section are given higher probabilities, including a weight of 0.2 for the 47 km-long rupture of sections "A" and "B", and a weight of 0.3 for the 32-km-long rupture of sections "B" and "C". The 56-km-long scenario in which all three of the northern sections ("A", "B", and "C") rupture is weighted 0.3, based on the presence of evidence of recurrent displacement along all three sections. Lastly, the longest scenario, in which rupture occurs along all four sections of the entire 73-km-long fault, is weighted low [0.1] because of the discontinuity of the fault between The Dell and Lookout Pass.

The maximum magnitude distribution for the Stansbury fault (Figure 6-6) includes all five of the rupture scenarios and reflects the postulated rupture dimensions based on combinations of rupture lengths and widths. In addition, data for average displacement during a single event were included in the assessment. These data suggest that the average displacement during a single event on the segment of the Stansbury fault that lies closest to the site is between 2 to 3 m (see discussion in Section 5.1). As described in Section 5.1, the following distribution for average single event displacement was used in this analysis: 1 m [0.1], 2 m [0.4], 3 m [0.4], 4.5 m [0.1].

As discussed in Section 5.1, the estimated late Pleistocene slip rate of the Stansbury fault is in the range of 0.4 ± 0.1 mm/yr. We represent the uncertainty in slip rate with the discrete distribution of 0.3 mm/yr [0.2], 0.4 mm/yr [0.6], and 0.5 mm/yr [0.2].

East Cedar Mountains Fault

As part of a hydrologic reconnaissance of Skull Valley, Hood and Waddell (1968) inferred the presence of a fault having east-down displacement along the eastern margin of the Cedar Mountains. We informally refer to this fault as the East Cedar Mountains fault (Plates 6 and 7). This inferred fault extends from a point due east of Hastings Pass and about 7 km southwest of the village of Dell (along Highway 80), south along the eastern margin of the Cedar Mountains to the southern end of the range at the town of Dugway. At its closest location, the fault is 9 km from the proposed PFSF site. As shown by Hood and Waddell (1968), the fault contains a northern, 33-km-long section that strikes about N10°E, and a southern, 27-km-long section that strikes about N45°W. The total fault length as shown by Hood and Waddell (1968) is 60 km.

Later workers, concentrating on the presence of fault scarps present in alluvial deposits, did not acknowledge the existence of this fault (Everitt and Kaliser, 1980; Barnhard and Dodge, 1988;

Hecker, 1993). However, Arabasz and others (1989) included suspected Pleistocene fault scarps along the northeastern flank of the Cedar Mountains, north of the fault mapped by Hood and Waddell (1968), in their compilation of seismic sources in the region. These possible faults were based on photolineaments that had been identified, but not field checked, by Barnhard and Dodge (1988). Hecker (1993) designates these inferred faults as "Quaternary (?)" and shows them as a 10 km-long zone of short (<2 km) discontinuous fault scarps that are 2 to 3 km east of the range front. Considering these possible fault traces as part of the East Cedar Mountains fault, the fault extends from the northern end of the Cedar Mountains at Interstate 80, to the southern end of the range at the town of Dugway. This interpretation of the fault yields a total fault length of 72 km, with a 45-km-long northern section and a 27-km-long southern section.

The entire length of the East Cedar Mountains fault is within the area covered by the late Pleistocene Lake Bonneville, based on the location of the Bonneville and Provo shorelines mapped by Currey and others (1983), Barnhard and Dodge (1988), and Sack (1993). The possible fault traces at the northern end of the range mapped by Barnhard and Dodge (1988) are located basinward of the 10,000- to 11,000-year-old Gilbert shoreline shown by Sack (1993). This would suggest possible fault movement within the past 11 ka. However, detailed mapping of surficial deposits throughout Skull Valley by Sack (1993) does not show the presence of the possible fault identified by Barnhard and Dodge (1988). It is likely that the features identified by Barnhard and Dodge (1988) are not related to surface faulting.

In addition, Sack (1993) identified a 1.5-km-long, northeast-facing scarp along the eastern margin of the Cedar Mountains, approximately 9 km southwest of Hickman Knolls. This scarp also is basinward of the Provo shoreline and, if related to surface faulting, would suggest a surface-rupture earthquake within the past approximately 15,000 years. However, aerial reconnaissance and preliminary aerial photographic analysis conducted for the SAR submittal study showed no evidence of surface displacement at the location of the scarps noted by Sack (1993), nor anywhere else along the eastern Cedar Mountains range front between Rydalch Canyon and Dugway. Based on examination of aerial photography conducted for this study, the scarps identified by Sack (1993) are at the same elevation as sinuous lake shoreline features to the southwest and, thus may be shoreline rather than tectonic scarps.

We conclude that there is no definitive evidence of post-Bonneville displacement along the East Cedar Mountains fault, as implied by mapping by Everitt and Kaliser (1980), Barnhard

and Dodge (1988), and Hecker (1993). However, with the available data, we cannot preclude the possibility of middle or late Pleistocene displacement (between 500 and 15 ka).

Based on the possible evidence for late Quaternary activity, the East Cedar Mountains fault is included as a fault source in the seismic source model for this analysis. We define the fault source to have a total length of 72 km, extending from the northern end of the Cedar Mountains at Interstate 80, to Dugway at the southern end of the Cedar Mountains (Plate 6). The East Cedar Mountains fault is assigned a probability of activity of 0.7 based on the questionable evidence of Quaternary activity and the possibility that this fault is truncated at depth by the west-dipping East fault at or above seismogenic depth. As shown on Figures 2-1 and 2-2, the overall basin geometry is consistent with a half graben bounded by the west-dipping East fault. The East Cedar Mountains fault, if it has been reactivated as a normal fault, may be truncated by the East fault at depths as shallow as 7 km. In the analysis the downdip width of the East Cedar Mountains fault incorporates the range of downdip extent permitted by varying fault geometries and dips for the East, West, and East Cedar Mountain faults.

We consider four possible values for the maximum rupture length, 12, 27, 45, and 72 km. A maximum rupture length of 12 km represents the average lengths of steep gradient segments that separate the more pronounced gravity anomalies. A maximum rupture length of 27 km represents the shortest straight segment of the fault that is well expressed as a linear gravity gradient. This length is comparable to the most well expressed segment of the Stansbury fault across Skull Valley. A maximum rupture length of 45 km represents the longest segment of the postulated fault. The lower three values of maximum length are given the most weight, 0.3, 0.4 and 0.15, respectively, because they are consistent with the overall structural framework of the valley and assessments of rupture lengths for the East and Stansbury faults. Rupture of the entire postulated length of the fault is given a weight of 0.05 because it is considered to be less likely than rupture of the entire Stansbury fault. No displacement data are reported for this fault. Therefore, the assessment of maximum magnitude is based empirical estimates of magnitude from assessments of rupture length and rupture area. The maximum magnitude distribution for the East Cedar Mountains fault, which reflects the postulated rupture dimensions based on combinations of the rupture length and width, is shown on Figure 6-6.

No slip rate data are available for the East Cedar Mountains fault. Assuming the East Cedar Mountains fault is an active fault, the slip rate probably is less than the slip rates for individual traces of the Stansbury fault, which are expressed as piedmont faults or the East fault. It is probably more analogous to the West fault, which is an intrabasin fault as opposed to the East

fault, which bounds the Tertiary basin (half graben). Based on comparison to these faults and the lack or limited extent of late Pleistocene/Holocene scarps along the range front, the following slip rates and weights are used for the East Cedar Mountain fault: 0.01 mm/yr [0.25], 0.04 mm/yr [0.25], 0.07 mm/yr [0.25], 0.1 mm/yr [0.2], 0.45 mm/yr [0.05]. The weight is distributed relatively uniformly among the lower four values, which are considered equally likely, and significantly less weight is given to the highest value that is considered less likely given the lack of geomorphic expression of recent faulting.

Rush Valley Faults

A number of short discontinuous faults having Quaternary scarps have been identified along the western margin and in the central part of Rush Valley (Plate 7). These include the Clover fault, the Sheeprock fault, the Mid-valley Horst, and the Vernon Hills fault. As described below we consider alternate models for the zone of faults along the western margin of the valley. The relatively short (<7 km) faults that border the Mid-valley Horst and Vernon Hills that are more distant from the proposed PFSF site are not modeled as a specific fault sources.

Clover Fault

The Clover fault is a northwest-trending, east-dipping normal fault that borders the northeast flank of the Onaqui Mountains along the western margin of Rush Valley (Bucknam, 1977; Everitt and Kaliser, 1980; Hecker, 1993). This fault zone also is referred to as the North Onaqui East Marginal fault (Everitt and Kaliser, 1980; Krinitzsky, 1989). At its closest approach, the Clover fault zone is 27 km from the proposed PFSF site. Scarps in late Pleistocene to Holocene(?) alluvium indicate a minimum fault length of 4 to 7 km. The scarps have been modified by agricultural activities and, therefore, cannot be used to estimate the age of faulting. The graded profiles of streams that cross the fault suggest that the most recent faulting occurred more than several thousand years ago (Barnhard and Dodge, 1988). Arabasz and others (1989) assign an age of >15.5 ka to the timing of the last movement on this fault. Scarps heights of 1.1 to 1.2 m, and a single event displacement of 0.6 m, are reported for the Clover fault (Barnhard and Dodge, 1988; Krinitzsky, 1989).

The Clover fault is characterized as an active fault with a probability of 1.0. The total length of the Clover fault is uncertain. The fault is one of a series of short discontinuous zones of Quaternary faulting along the western margin of Rush Valleys. To the north, a short (1.3-km-long), east-facing fault scarp in older alluvium near East Hickman Canyon is mapped by Solomon (1993). To the south, Everitt and Kaliser (1980) identify lineaments and a possible scarp along the southeast flank of the Onaqui Mountains and prominent Quaternary fault scarps

are mapped along the Sheeprock fault (Plate 7). The short lengths of these fault scarps suggest that the earthquakes that produced these scarps were at or near the threshold magnitude of surface rupture (i.e., M 6 to 6.5) and that the length of subsurface rupture may have exceeded the length of surface faulting. In order to address the uncertainty in the length and continuity of faults along the western margin of Rush Valley, alternate models and rupture scenarios for the Clover, East Hickman, and Sheeprock faults are considered.

Given the discontinuity of surface faulting along the western margin of Rush Valley and the evidence for a greater number of late Quaternary surface faulting events on the Sheeprock fault, relatively low weight [0.2] is given to a model (referred to as the west-side zone in Table 6-2) that allows for a continuous 52 km-long fault connecting the East Hickman Canyon scarp, Clover and Sheeprock faults. A maximum rupture length of 19 km [1.0] postulated for this fault zone reflects the lack of evidence for large magnitude earthquakes that would rupture the entire western margin zone.

Greater weight is afforded the model in which the Clover and Sheeprock faults are treated as independent fault sources. In this model the connection between the Clover fault and the fault scarps near Hickman Canyon is treated with uncertainty in the total length of the Clover fault. A weight of 0.25 is given to a total length of 7 km (the mapped length of the fault) and a weight of 0.75 is given to the combined length of 19 km.

The assessment of maximum magnitude is based on empirical estimates of magnitude from assessments of rupture length, rupture area, and single event displacement. It is uncertain whether the estimated single event displacement reported for this fault represents a maximum or average value. It is more likely that a single measurement along a fault represents the average value rather than the maximum, and thus the empirical relationship between maximum magnitude and average single event displacement is assigned higher weight [0.7] than the relationship based on maximum single event displacement [0.3]. The maximum magnitude distribution for the Clover fault is shown on Figure 6-6.

The slip rate for the Clover fault is not well constrained. The older alluvial fan deposits that are displaced by the Clover and East Hickman Canyon fault scarps are mapped as pre-Bonneville (>15.5 ka) (Everitt and Kaliser, 1980; Solomon, 1993). Based on scarp morphology the most recent episode of surface faulting appears to pre-date the Bonneville highstand and may be as young as ~35 ka on the East Hickman Canyon scarp (Solomon, 1993). Assuming that the older displaced alluvial fans are late Pleistocene (> 15.5 – 130 ka) and that only a single 0.6 m event

has occurred along the Clover fault yields a slip rate of 0.004 to 0.04 mm/yr. Assuming that this event occurred ~35 ka yields a rate of 0.01-0.02 mm/yr. The small displacement and/or lack of multiple surface faulting earthquakes along this fault suggests relatively low rates of activity. Therefore, a slip rate distribution of 0.01 mm/yr [0.6] and 0.05 mm/yr [0.4] is assigned to the Clover fault (Model A). A slightly higher weight is assigned to the 0.05 mm/yr value in Model B (Clover and Sheeprock faults combined) based on the possibility of higher rates of activity on the Sheeprock fault.

Sheeprock Fault Zone

The Sheeprock fault is a northeast- to northwest-trending, east-dipping normal fault along the northeastern flanks of Sheeprock Mountain. At its closest approach, the Sheeprock fault is 41 km from the proposed PFSF site. A zone of Quaternary fault scarps extends about 10 to 11 km along the fault zone (Everitt and Kaliser, 1980; Barnhard and Dodge, 1988; Hecker, 1993; Bucknam, 1977). Scarp heights range from 1.9 to 16.5 m with some scarps representing repeated surface rupture (Barnhard and Dodge, 1988). A possible Holocene age was inferred for the most-recent event along the Sheeprock fault (Everitt and Kaliser, 1980). However, more recent scarp-profile investigations suggest that the Sheeprock scarps are older than the Topliff Hill and Mercur, which pre-date the Bonneville highstand (15.5 ka) (Barnhard and Dodge, 1988). Diffusion-equation modeling of the scarps yielded an age of about 53 ka for the scarps (Hanks and others, 1984). The embayed character of the range front suggests a long period of activity preceding the recent episode of faulting (Everitt and Kaliser, 1980).

The Sheeprock fault is characterized as active with a probability of 1.0. As discussed in the previous section a 0.8 probability is given to a model in which this fault is an independent fault source and a 0.2 probability that it is part of a more continuous fault that includes the Clover fault. The latter model is described in the previous section. Assuming that the Clover fault is an independent fault (Model A) we assume that the entire 18 km-long fault will rupture during a single earthquake. No displacement data are reported for this fault. Therefore, the assessment of maximum is based on empirical estimates of magnitude from assessments of rupture length and rupture area. The maximum magnitude distribution for the Sheeprock fault (Figure 6-6) reflects the postulated rupture dimensions based on combinations of the rupture length and width given in Table 6-2.

The slip rate for this fault is not well constrained. The higher fault scarps along this fault suggest a slightly higher level of activity relative to other Quaternary faults mapped within and along the western margin of the Tooele and Rush Valleys. The slip rate distribution used for

this fault, 0.01 mm/yr [0.4], 0.05 mm/yr [0.5], and 0.1 mm/yr [0.1], is consistent with the rates estimated for faults within the valley and the more recently active structures (the Oquirrh, Mercur, Topliff Hill, and Stansbury faults) bounding the major ranges adjacent to the Tooele and Rush Valleys.

Oquirrh-East Great Salt Lake Fault Zone

The Oquirrh-East Great Salt Lake Fault Zone consists of a series of major westward-dipping, range-bounding Quaternary normal faults that includes the Oquirrh (Everitt and Kaliser, 1980; Olig and others, 1994) and East Great Salt Lake (Pechman and others, 1987; Viveiros, 1986) fault zones to the north and the East Tintic Mountain fault zones (Barnhard and Dodge, 1988) to the south (Plate 7). In their seismic hazard model, Youngs and others (1987) treat these faults as individual segments in a large fault zone they referred to as the Oquirrh Mountain fault zone, herein referred to as the Oquirrh-East Great Salt Lake fault zone. Each of these fault zones is described as a separate fault zone in the compilation by Hecker (1993). Wong and others (1995) present a segmentation model based on the following division of segments: the Promontory Mountains and Antelope Island segments of the East Great Salt Lake fault; the Oquirrh fault; the Mercur and Topliff Hill faults combined; and the East Tintic fault. In this analysis alternate models are considered that allow for both independent and dependent behavior of faults along this regional north-south trending zone of faults. Starting with the faults that lie closest to the proposed PFSF site, we discuss our segmentation model in the following sections.

Mercur-Topliff Hill Fault Zone

The Mercur-Topliff Hill fault zone consist of a zone of Quaternary faulting along the western side of the Oquirrh Mountains and Topliff Hill in Rush Valley (Plate 7). At its closest approach, this fault zone is 40 km from the proposed PFSF site. The Mercur fault zone consists of a 16-km-long alignment of late Pleistocene fault scarps along the western flank of the Oquirrh Mountain in Rush Valley. Based on exposures of faulted alluvium exposed in a mining shaft, together with an uplifted bedrock pediment, Everitt and Kaliser (1980) estimated a minimum of 60 m of Quaternary displacement on the fault. From scarp profile data, the Mercur scarps record displacements of 1.8 to 5.6 m (Barnhard and Dodge, 1988). Krinitzsky (1989) reports scarp heights of 2.1 to 7.7 m and a single event displacement of 0.9 to 1.9 m for the Mercur fault zone based on the scarp profile results of Barnhard and Dodge (1988). Solomon (1993) identified a small fault scarp south of the town of Stockton approximately 11 km north of the Mercur fault that exhibits a similar orientation and sense of displacement to the Mercur fault zone scarps. This scarp offsets late Pleistocene Lake Bonneville sediments, and it

is not clear if it is related to surface-faulting events along the Oquirrh fault zone to the north or the Mercur fault zone to the south.

The Topliff Hill fault zone lies along the west flank of the northern East Tintic Mountains, a lower more subdued range to the south of the Oquirrh Mountain range (Hecker, 1993). A zone of fault scarps, which are relatively continuous for a distance of 12 km, exhibit a similar geomorphic position and sense of displacement as those along the Mercur fault zone. These scarps also show evidence for recurrent movement with a reported cumulative maximum displacement of 5.8 m; the scarps appear to be younger than the Mercur fault scarps based on scarp profile data (Barnhard and Dodge, 1988).

Everitt and Kaliser (1980) concluded that the most-recent surface faulting event along the Mercur-Topliff Hill fault zone post-dated the formation of the Bonneville shoreline. Barnhard and Dodge (1988) reinterpreted a trench log by Everitt and Kaliser (1980), and note that scarps along the Mercur-Topliff Hill fault zone are wave-etched and, therefore, are older than the Bonneville shoreline. Based on scarp morphology the Mercur-Topliff Hill fault zone scarps are interpreted to be late Pleistocene (Barnhard and Dodge, 1988; Hecker, 1993).

Based on the presence of scarps across and observed displacement of late Pleistocene deposits, the Mercur-Topliff Hill fault zone is included as a fault source with a probability of activity of 1.0. The continuity and relationship of the Mercur and Topliff fault zones in the subsurface is not known. Variations in the continuity, orientation, and possibly in the ages of the fault scarps along the zone of Quaternary faulting on the east side of Rush Valley suggest that these faults may behave as independent faults and this model (Model A) is given a weight of 0.4 in this analysis. A slightly higher weight is given to a model (Model B) in which these faults are considered to be part of the same fault zone. The shortest rupture lengths considered in both models reflect the length of relatively continuous fault scarps along both the Mercur and Topliff fault zones, 16 km and 12 km, respectively. A rupture length of 27 km for the Mercur fault zone is based on the assumption that the small fault scarp near Stockton is related to Mercur scarps. The 24- km-long postulated rupture length along the Topliff Hill fault zone assumes a rupture of both the southern linear range front segment and northern late Pleistocene segments of the Topliff Hill fault zone. The total length of the fault zone characterized in Model B is 56 km, the distance from Stockton to the southern end of the Topliff Hill fault zone. A 33 km-long rupture, equivalent to the combined length of late Quaternary faults scarps along the Mercur and Topliff Hill faults is given the most weight [0.5]. A shorter rupture length of 16

km, the length of the Mercur fault scarps and a longer rupture of the entire zone (56 km) are weighted 0.2 and 0.3, respectively.

The assessment of maximum magnitude is based on empirical estimates of magnitude from assessments of rupture length, rupture area, and single event displacement. It is uncertain whether the estimated single event displacement reported for this fault represents a maximum or average value. It is more likely that a single measurement along a fault represents the average value rather than the maximum, and thus the empirical relationship between maximum magnitude and average single event displacement is assigned higher weight [0.7] than the relationship based on maximum single event displacement [0.3]. The maximum magnitude distribution for both models (see Figure 6-6) reflects the postulated rupture dimensions based on combinations of rupture lengths and widths given in Table 6-2 and an estimated 0.9 to 1.9 m single-event displacement for the Mercur fault zone.

The slip rate on the Mercur and Topliff Hill fault zones is not well constrained. The assessed distribution for average slip rate shown in Table 6-2 was based on assumed ages for older alluvium displaced by the fault (Everitt and Kaliser, 1980) and comparison of these fault scarps to those along the Oquirrh fault zone. The estimated age of the soil developed on the older alluvium suggests that the alluvial fans along the flanks of the Oquirrh Mountains may be equivalent to Bull Lake alluvium estimated to be ~160 ka to 130 ka. Assuming that the 1.8- to 7.7-m-high scarps reflect net displacement post-130 ka and pre-14.5 ka suggests that the long-term average slip rate for the Mercur fault zone falls within the range of 0.01 to 0.5 mm/yr. A long-term slip rate of 0.03 mm/yr is estimated from the cumulative minimum Quaternary displacement of 60 m in ~1.8 Ma. The heights of the most recent fault scarps as well as the relative height of the adjacent ranges, suggests that the rate of slip along the Mercur and Topliff Hill fault zones is equal to or slightly less than Oquirrh fault zone, which is estimated to be 0.1 to 0.2 mm/yr (Olig and others, 1994). Slip rates of 0.1 to 0.2 mm/yr or less are typical of Basin and Range faults away from the Wasatch fault (Schwartz, 1987). Based on consideration of these estimates, a preferred range of slip rates and weights is used as follows: 0.05 mm/yr [0.5], 0.1 mm/yr [0.4], 0.2 mm/yr [0.1].

Oquirrh Fault Zone

The Oquirrh fault zone is a west-dipping normal fault that borders the western side of the Oquirrh Mountains in Tooele Valley. At its closest approach, the Oquirrh fault zone is 45 km from the proposed PFSF site. A variety of names have been used for this fault zone including: the Oquirrh marginal fault (Everitt and Kaliser, 1980); the northern Oquirrh fault zone

(Barnhard and Dodge, 1988; Hecker, 1993); and the Oquirrh fault zone (Olig and others, 1994). We follow Olig and others (1994) in referring to the zone of Quaternary faulting along the northern part of the Oquirrh Mountains as the Oquirrh fault zone. The fault zone extends for a least 21 km and has been subdivided into two sections: a northern section that includes fault scarps in alluvium, and a southern section that includes a fault contact between bedrock and alluvium along the range front (Everitt and Kaliser, 1980; Barnhard and Dodge, 1988). An additional segment near Silcox Canyon southwest of Tooele, identified by Everitt and Kaliser (1980) as a scarp of erosional or undetermined origin is identified by Solomon (1993) as a fault scarp. A zone of subsidiary faults lies within about 5 km west of the main fault in the southern Great Lake (Hecker, 1993). These faults may represent the northern extension of the Oquirrh fault zone.

Scarps along the Oquirrh fault zone range in height between 2.9 and 10.8 m, and surface offsets are between 1.3 and 7.3 m (Barnhard and Dodge, 1988). Locally, the compound scarps represent displacement during more than one surface-faulting earthquake. Scarps of the Oquirrh fault zone displace the Provo shoreline of Lake Bonneville. Studies of scarp morphology suggest that the most recent surface-faulting event occurred between 9 ka and 13.5 ka (Everitt and Kaliser, 1980; Barnhard and Dodge, 1988). More recently, paleoseismological investigations along the northern section of the Oquirrh fault zone by Olig and others (1994) documented that: (1) the most recent surface faulting event occurred between 4.3 ka and 6.9 ka, (2) the second-most-recent event occurred between 20.3 and 26.4 kyr B.P., (3) the net vertical tectonic displacement is between 1.9 and 3.3 m with best estimates of 2.2 and 2.7 m for the most-recent event and 2.3 m for the penultimate event, (4) the recurrence interval between the last two events ranges from 13.3 ka and 22.1 ka, (5) calculated slip rates are 0.1 to 0.2 mm/yr for this interval, and (6) the third-most-recent event probably occurred before 33.95 ± 1.16 ka.

Total length of the Oquirrh fault zone is estimated to be 35 km, which allows for the fault to extend a few kilometers northwards into the Great Salt Lake and includes the isolated, short, discontinuous fault scarps near Stockton. Comparison of the available information regarding timing of the surface-faulting events on the Oquirrh fault zone, and the Mercur fault zone to the south suggests that these fault zones have behaved as independent rupture segments since the Bonneville lake cycle (Olig and others, 1994). Available paleoseismic information is inconclusive regarding a possible rupture segment boundary between the Oquirrh fault zone and the East Great Salt Lake fault zone to the north (Olig and others, 1994). Wong and others (1995) summarize data that support a segmentation boundary in this area. Two rupture models,

therefore, are considered: Model A, which treats the two latter faults as independent structures is given higher weight [0.9] based on data presented by Wong and others (1995) and Model B [0.1], which allows for ruptures to extend across the boundary between the mapped fault traces. A discussion of the offshore data used to evaluate this boundary is provided in the following section describing the East Great Salt Lake fault.

The rupture lengths and weights used in Model A are as follows: 12 km (the length of the northern section of the Oquirrh fault zone) [0.2]; 21 km (the combined length of the northern and southern sections) [0.4]; 35 km (the total length of the Oquirrh fault zone as described above) [0.4]. The rupture lengths and weights used in Model B reflect the possibility of longer ruptures due, in part, to the uncertainty in the continuity of fault segments that are mapped beneath the Great Salt Lake. Postulated rupture lengths for Model B are: 21 km [0.3], 35 km [0.5], and 52 km [0.2].

The assessment of maximum magnitude is based on assessments of rupture length, rupture area, and single-event displacement. The maximum magnitude distribution for both models (see Figure 6-6) reflects the postulated rupture dimensions based on combinations of rupture lengths and widths given in Table 6-2 and the estimated 2.2 to 2.7 m single event displacement for the Oquirrh fault zone. Olig and others (1994) note that the measured net vertical displacement values although limited in number are similar, suggesting they are closer to an average than an extreme. On this basis, we assume the 2.2 to 2.7 range reflects an average [0.7] rather than a maximum [0.3] single event displacement. As noted by Olig and others (1994), magnitude estimates based on displacement data are higher than those based on the 21 km length of the mapped fault.

Although recurrence data are available for the northern section of the Oquirrh fault zone, comparable data are not available for the rest of the Oquirrh fault zone or the East Great Salt Lake fault zone. Slip rate estimates are available for the Oquirrh fault zone as discussed above and for the East Great Salt Lake fault zone. These provide the basis for the estimated range of values given for both Models A and B in Table 6-2.

East Great Salt Lake Fault Zone
Gravity and seismic reflection data indicate that a major 100-km-long zone of faulting is concealed beneath the Great Salt Lake along the western margin of the NNW-trending linear topographic high that includes the Promontory Mountains, Fremont Island, and Antelope Island. This west-dipping fault, named the East Great Salt Lake fault zone by Cook and others

(1980), is clearly delineated in seismic reflection profiles across the lake (Mukulich and Smith, 1974; Smith and Bruhn, 1984; Viveiros, 1986; Pechmann and others, 1987; Mohapatra and others, 1993). These studies indicate that the fault exhibits normal displacement, generally strikes north-northwest and dips 30° to 50° to the west, and appears to have a listric geometry along at some of its length. At its closest approach, this fault zone is 66 km northeast of the proposed PFSF site.

This fault cuts sediments identified as Quaternary based on well data and appears to displace sediments within 10 to 20 m of the lake bottom (Viveiros, 1986; Hecker, 1993; Mukulich and Smith, 1974). A 1.5-km-long zone of *en echelon* fractures beneath the lake west of Antelope Island appears on aerial photos to have slight down-on-the-west displacement and to be unmodified by coastal processes, and thus may date from the latest Holocene (Smith and Bruhn, 1984; Hecker, 1993). Observations in drill holes suggest that the Mazama ash may be offset, inferring faulting may be younger than 6,800 yrs (D. R. Currey, written communication, 1994 as reported by Wong and others, 1995).

Following Pechmann (1987) and Wong and others (1995) we divide the East Great Salt Lake fault zone into two segments: a 40-km long Promontory Mountains segment and a 52 km- long Antelope Island segment. As noted above the relationship between the Oquirrh fault and the East Great Salt Lake fault zones is uncertain. Two rupture models as described in the previous discussion of the Oquirrh fault zone are considered: a model in which the two faults are independent fault sources (Model A) and a model in which ruptures may extend across the boundary between the two faults (Model B). In Model A rupture lengths postulated for the East Great Salt Lake fault zone are: 35 km (the length of the southern part of the fault zone bordered by Antelope Island), 40 km (the length of the northern segment), and 52 km (the length of the southern segment). In the combined rupture model (Model B) only the southern 52 km-long segment of the East Great Salt Lake fault zone is considered. The maximum magnitude distribution for both models (see Figure 6-6) reflects the postulated rupture dimensions based on combinations of rupture lengths and widths given in Table 6-2. The maximum magnitude distribution for Model B includes consideration of the paleoseismic evidence for single-event displacement outlined in Table 6-2.

Viveiros (1986) estimated fault slip rates on the East Great Salt Lake fault of 0.96 mm/yr during the Pliocene and 1.48 mm/yr during the Quaternary based on thickness of sedimentary deposits and inferred fault geometries. Vertical subsidence rates near the fault are estimated to be 0.3 to 0.5 mm/yr (Pechmann and others, 1987). Taking subsurface fault dip into account,

these rates translate into fault slip rates of 0.4 to 0.7 mm/yr, assuming that the sedimentation rates are controlled by subsidence along the fault (Pechmann and others, 1987). These rates, which are approximately one-half of those measured for the Wasatch fault zone, are over double the rates estimated for the Oquirrh fault zone. Net tectonic displacements, however, may be considerably less than the measured subsidence due to antithetic faults and back-tiliting of the hanging wall. These possibilities are not discussed by Pechmann and others (1987). The distribution of estimated slip rates used for the East Great Salt Lake fault (Model A) and the combined East Great Salt Lake and Oquirrh fault zones (Model B) as listed in Table 6-2 incorporate the higher rates presented by Pechmann and others as well as the possibility that the rates are more comparable to those determined for the Oquirrh fault zone.

East Tintic Mountains Fault

The 36-km-long East Tintic Mountains fault is a north-trending, west-dipping fault along the western side of the East Tintic Mountains (Plate 7). At its closest approach, this fault is 72 km southeast of the proposed PFSF site. Isolated, highly dissected scarps in alluvium along the fault appear to be among the oldest in western Utah (Bucknam and Anderson, 1979). Anderson and Miller (1979) mapped buried Quaternary (?) faults extending to the north and south of the alluvial scarps. These faults and faults that form bedrock-alluvium contacts at the south end of the East Tintic Mountains (Morris, 1987) are mapped as Quaternary (?) by Hecker (1993). This fault zone was considered to be a segment of the Oquirrh fault zone as described by Youngs and others (1987). Given the differences in recency and activity along this fault compared with the Mercur-Topliff Hill, Oquirrh, and East Great Salt Lake fault zones to the north, we consider this fault as an independent fault source.

Postulated rupture scenarios allow for rupture of the entire (35 km) length of Quaternary faults along the western margin of the East Tintic Mountains as mapped by Hecker (1993), or rupture of the northern 20 km-long segment that includes the most recent scarps. These rupture lengths are given weights of 0.6 and 0.4, respectively. The assessment of maximum magnitude is based on empirical estimates of magnitude from assessments of rupture length and rupture area. The maximum magnitude distribution (see Figure 6-6) reflects the postulated rupture dimensions based on combinations of rupture lengths and widths given in Table 6-2. Given the lack of slip rate data, a slip rate distribution is estimated based on the lesser degree of activity of this fault as expressed geomorphically compared to the fault zones along trend to the north. The following range of slip rate values are used: 0.005 mm/yr [0.1], 0.01 mm/yr [0.4], 0.05 mm/yr [0.4], 0.1 mm/yr [0.1].

West Valley Fault Zone

The West Valley fault zone consists of a series of mostly east-dipping normal faults that displace late Quaternary lake deposits in Salt Lake Valley (Plate 7). At its closest approach, the West Valley fault zone is 75 km northeast of the proposed PFSF site. This fault zone was originally called the Jordan Valley fault zone and subsequently renamed the West Valley fault zone (Keaton and others, 1987). The southern portion of the fault zone consists of two subparallel east-facing scarps (the Granger and Taylorsville faults), whereas the northern portion is broader and is characterized by many smaller, east- and west-facing scarps. Locally, the near-surface expression of the fault zone is characterized by monoclinal flexuring and minor step-faulting. The total length of the zone is about 18 km (Keaton and others, 1987). Geomorphic and stratigraphic evidence of two events during the past 12 ka to 13 ka is documented along the main Granger and Taylorsville faults (Keaton and others, 1987). Geomorphic relations within the northern West Valley fault zone suggest that four or more events occurred in the same time period and that some of the post-Bonneville faulting occurred prior to formation of the Gilbert shoreline (12 ka). Borehole evidence associated with several traces of the northern West Valley fault zone suggests that the most recent event may have occurred 6 ka to 9 ka and that two or three events may have occurred since 22 ka to 28 ka (Hecker, 1993; Keaton and others, 1987). As noted by Youngs and others (1987), it is unclear whether movement on the West Valley fault zone is independent or directly tied to movement on the Salt Lake City segment of the Wasatch fault zone. A Holocene slip rate of 0.5 to 0.6 mm/yr is estimated for the Granger fault and the West Valley fault zone as a whole. Lower rates of 0.1 to 0.2 mm/yr are inferred for the Taylorsville fault over longer periods of time (< 140 ka). The relatively high slip rate calculated for post-Bonneville time suggests that strain release may be due to isostatic rebound within an extensional setting (Hecker, 1993).

The seismic source characterization used in this study follows that described in Youngs and others (1987). As noted by Youngs and others, it is unclear whether movement on the West Valley fault zone is independent or directly tied to movement on the Salt Lake City segment of the Wasatch fault zone. These two models are given weights of 0.6 and 0.4, respectively.

Given that the West Valley fault is an independently active source, it is modeled as a single fault segment because its overall length is so short. The maximum rupture length is assumed to be equal to the total length of the zone (18 km). The estimated slip rate distribution of 0.3 mm/yr [0.5], and 0.5 mm/yr [0.5] incorporates the range of available slip rate data.

Utah Lake Fault Zone

Latest Pleistocene to Holocene (?) faults and associated folds are identified over a 30 km length in Utah Lake based on seismic-reflection profile data (Brimhall and Merritt, 1981). At their closest approach, the Utah Lake faults are 79 km east of the proposed PFSF site (Plate 7). Due to the widely spaced seismic-reflection transects, the fault locations are uncertain. An 8- to 15-m-deep layer identified as the Provo Formation, which is interpreted to be lake bottom sediments probably deposited during the regressive phase of Lake Bonneville (Machette, 1989), is displaced from < 2 to 5 m across individual faults and folds beneath the lake. The reflection profiles suggest that displacements decrease upward in strata above this horizon and occur within several meters of the lake bottom.

It is not clear if movement on the Utah Lake fault zone is independent or directly tied to movement of the Wasatch fault zone. Based on the uncertainties in the geometries and tectonic significance of these structures, we assign the Utah Lake fault zone a probability of activity of 0.6 and treat it similar to the West Valley fault zone as discussed above. Rupture lengths of 20 km and 30 km, which reflect the lengths of the longer more continuous mapped traces and the total length of the fault zone, are assigned equal weight. The estimated slip rate distribution of 0.3 mm/yr [0.5], and 0.5 mm/yr [0.5] incorporates the range of available slip rate data.

Drum Mountains Fault Zone

The Drum Mountains fault zone is a series of north-trending, east-dipping faults along the eastern margin of the Drum Mountains. At its closest approach, the fault zone is 80 km south of the proposed PFSF site. Bucknam and Anderson (1979) map a 5-km-wide zone of fault scarps within pre-Lake Bonneville age deposits east of the Drum Mountains. The fault zone, as shown by Hecker (1993), is 36 km long. Faulted Provo-level shoreline features provide a maximum age of 13.5 ka for the scarps (Crone, 1983). Scarps range in height from 0.7 to 7.3 m, with average heights of 2.4 m, and show no geomorphic evidence of having multiple events (Hanks and others, 1984). Morphometric analyses of the scarps provide ages of 5.6 ka (Hanks and others 1984) and 9 ka (Pierce and Colman, 1986). Trenching by Crone (1983) showed that Holocene faulting produced 3.7 m of stratigraphic throw, significantly more than the 2.7 m of surface offset measured from nearby scarp profiles.

Based on the presence of scarps across and observed displacement of late Pleistocene deposits, the Drum Mountains fault zone is included as a fault source with a probability of activity of 1.0. A maximum rupture length of 36 km (the length of Holocene faulting) is assigned a

weight of 1.0 based on the evidence for a single rupture event. The assessment of maximum magnitude is based on empirical estimates of magnitude from assessments of rupture length, rupture, area, and single-event displacement. The maximum magnitude distribution (see Figure 6-6) reflects the postulated rupture dimensions based on combinations of rupture length and widths and includes consideration of the paleoseismic evidence for single-event displacement as outlined in Table 6-2.

Based on the evidence of 3.7 m of slip in pre-Bonneville deposits reported by Crone (1983) and assuming an age range of ~30 ka to 160 ka for the pre-Bonneville deposits, the long-term slip rate for this fault ranges from 0.023 to 0.12 mm/yr. We use the following slip rate distribution in this analysis: 0.02 mm/yr [0.3], 0.05 mm/yr [0.4], and 0.2 mm/yr [0.3].

Fish Springs Fault

The Fish Springs fault is a north-trending, east-dipping fault along the eastern margin of the Fish Springs Range. At its closest approach, the fault is 81 km southwest of the proposed PFSF site (Plate 7). Bucknam and Anderson (1979) map the Fish Springs fault within alluvial fan deposits near the eastern base of the Fish Springs Range. The fault consists of a southern trace about 8 km long, and a northern fault trace about 3 km long. The potential fault rupture length, assuming scarps along both traces represent surface rupture in a single event, is about 12 km long (Bucknam and Anderson, 1979). A lack of scarp dissection and sharp nickpoints in small washes that cross the scarps suggest that the fault scarps are young (Bucknam and Anderson, 1979). The scarps occur below the level of the Bonneville shoreline and offset alluvial fan deposits that overlie shoreline features. The scarps therefore are younger than 12 ka. Field observations by Bucknam and Anderson (1979) suggest a maximum single-rupture surface offset of 3.3 m.

Based on the presence of scarps across and observed displacement of late Pleistocene deposits, the Fish Springs fault zone is included as a fault source with a probability of activity of 1.0. A maximum rupture length of 30 km (the length of the range front) is assigned a weight of 1.0. The assessment of maximum magnitude is based on empirical estimates of magnitude from assessments of rupture length, rupture, area, and displacement per event. The maximum magnitude distribution (see Figure 6-6) reflects the postulated rupture dimensions based on combinations of rupture length and widths given in Table 6-2 and an estimated 3.3 m maximum displacement per event for the Fish Springs fault. A long-term slip rate is not available for this fault. Based on analogy to the Drum Mountains fault zone and other low slip rate Basin and

Range faults, we use the following slip rate distribution in this analysis: 0.02 mm/yr [0.3], 0.05 mm/yr [0.4], and 0.2 mm/yr [0.3].

Wasatch Fault Zone

The 370-km-long Wasatch fault zone forms the eastern boundary of the Basin and Range province (Plate 1). The Wasatch fault zone contains nine westward-dipping normal fault segments that exhibit late Pleistocene or younger activity (Hecker, 1993). These segments are differentiated on the basis of timing of individual earthquakes and changes in scarp morphology and geometry (Machette and others, 1991). Three of the Holocene segments of the Wasatch fault zone are located within 100 km of the proposed PFSF site: the Salt Lake City, Provo, and Nephi segments. Paleoseismologic studies show that there have been repeated large-magnitude earthquakes on all three of these segments of the Wasatch fault zone. A seismic source model for the Wasatch fault zone is provided by Youngs and others (1987). The model was updated to incorporate current estimates of earthquake repeat times from McCalpin and Nishenko (1996), which reflect the results of paleoseismic studies conducted since 1987.

The 46-km-long Salt Lake City segment of the Wasatch fault zone is located approximately 81 km east of the proposed PFSF site. The Salt Lake City segment consists of three left-stepping surface traces that bound the western base of the Wasatch Range within Salt Lake City (Machette and others, 1991). The most-recent earthquake on the segment probably occurred 1,000 to 1,800 years ago (Hecker, 1993). However, diffusion-equation modeling of scarp degradation suggests a more recent age of 900 years. Based on Holocene fault scarps, average surface displacement per event is 2 m. Latest Quaternary slip rate estimates of 1 mm/yr are assigned to this segment of the Wasatch fault zone (Hecker, 1993).

Fault parameters used to characterize the Wasatch fault zone are presented on Table 6-2. Two models are considered: an unsegmented model and a segmented model. In the unsegmented model, the maximum rupture length is not constrained by the geologically defined segment boundaries and maximum rupture lengths up to 100 km are considered allowing for the simultaneous rupture of adjacent segments (Table 2 in Youngs and others, 1987). One hundred kilometers is about the maximum length of surface rupture reported for historic normal-faulting earthquakes (Wells and Coppersmith, 1994). Based on the results of paleoseismic investigations, which suggest the segments have ruptured independently during past earthquakes (Youngs and others, 1987; Machette and others, 1991), relatively low weight [0.2] is assigned to the unsegmented model compared to the segmented model [0.8].

Given the unsegmented model the average slip rate is judged to be in the range of 0.7 to 1.8 mm/yr based on the range of values reported by Hecker (1993) for the segments south of Collinston and north of Levan. The preferred value of about 1.1 mm/yr is based on the weighted average (weights were based on the relative segment lengths) of the central slip-rate values reported by Hecker (1993) for the Brigham City, Weber, Salt Lake City, Provo and Nephi segments. The range of values and assigned weights for the average slip rate on the Wasatch fault (unsegmented model) are: 0.7 mm/yr [0.05]; 0.9 mm/yr [0.2]; 1.1 mm/yr [0.4]; 1.3 mm/yr [0.25]; and 1.8 mm/yr [0.05].

Given the segmented model, the maximum rupture length for the each segment is taken as the total length of the geologically defined segments. The frequency of earthquakes is based on the recurrence data for past surface-faulting events compiled by McCalpin and Nishenko (1996) for each of the segments. McCalpin and Nishenko do not report recurrence intervals for the Collinston and Levan segments. These segments are at the north and south ends of the fault respectively. The end segments have a much lower rate of activity than the segments in between. Recurrence on these end segments was constrained using slip rate (Table 6-2). Based on 12-m high scarps in alluvium estimated to be several hundred thousand years old (Personius, 1990; Hecker, 1993), the slip rate on the Collinston segment is significantly lower than along the segment to the south. The actual rate is not well constrained. The following range of values was included in the hazard analysis: 0.02 mm/yr [0.45]; 0.04 mm/yr [0.45]; and 0.08 mm/yr [0.1]. The slip rate on the Levan segment also is not well constrained. Based on a single Holocene event (Jackson, 1991), the slip rate on the Levan segment is estimated to be <0.3 mm/yr (Hecker, 1993). The range of values included in the hazard analysis is: 0.05 mm/yr [0.1]; 0.1 mm/yr [0.4]; 0.2 mm/yr [0.4]; and 0.3 mm/yr [0.1]

6.2.2 Seismic Source Zones

Four areal source zones as shown on Figure 6-7 are incorporated into the seismic hazard model for this study. The Wasatch fault zone forms the boundary between the central and eastern zones. The boundaries between the central and western zones are defined by the apparent change in the number of recorded earthquakes in the three areas. The southeastern corner of the eastern source zone was configured to exclude the areas of coal mining induced seismicity defined by Arabasz and others (1997).

6.2.2.1 Recurrence

The earthquake catalog used in this study was compiled by the University of Utah. The catalog includes both the historical and instrumental earthquake records, which extend from 1850 to

July, 1962 and July, 1962 to the present, respectively. The historical period begins with the first publication of a Utah newspaper in 1850 and has been carefully cross-checked and annotated with several sources of information, including the NOAA earthquake data file at the National Geophysical Data Center, by the University of Utah. The instrumental period of the catalog relies heavily on the University of Utah network data. The instrumental record begins in July of 1962 with data recorded from 26 stations statewide, with improvements in coverage and instrumentation occurring in 1974 and 1981. A comprehensive documentation of the catalog is given in Arabasz and others (1989), which was created for the proposed siting of the Superconducting Super Collider (SSC). The catalog was upgraded significantly for the SSC project, including deletion of quarry blasts and duplicate recordings of events, and modification of magnitudes to make them consistent between different networks and historical recordings, thus making further improvement of the catalog unnecessary for this project. We incorporated the preliminary estimates of M_L for events past 1994 (W. Arabasz, personal communication, 1999).

For this project seismicity data were pulled for an approximately 200-km radius region encompassing the site (Figure 6-7). The maximum recorded magnitude in the region shown on Figure 6-7 is a **M** 6 event (10/6/1909). Seismic activity for the region is depicted on Figure 6-7 along with the regional source zones. The pattern of seismicity is fairly evenly distributed along the Wasatch Range, with clusters of activity occurring to the west and east of the range.

The estimation of earthquake recurrence parameters requires the identification and removal of dependent events (foreshocks and after shocks) and specification of the periods of complete reporting. Dependent events were identified using the methodology described by Youngs and others (1987).

Estimation of recurrence parameters also requires an assessment of the time period over which there has been complete reporting of earthquakes (see Stepp, 1972). Youngs and others (1987) analyzed the earthquake catalog for north-central Utah and found the following periods of catalog completeness:

Magnitude Range	Period of Complete Reporting
3.0 - 4.0	10/01/1974 to present
4.0 – 5.3	01/01/1938 to present
5.3 – 6.0	01/01/1875 to present
>6.0	01/01/1850 to present

The above periods of compete catalog reporting were used to estimate the recurrence parameters for each of the seismic source zones using the maximum likelihood technique (Weichart, 1980). Figure 6-8 shows the resulting recurrence relationships compared to the recorded seismicity within each source zone. The uncertainty in the recurrence relationship for each source zone was modeled by specifying a range of possible b-values and seismicity rates and computing the relative likelihood that each to the resulting recurrence relationships generated the observed earthquake catalog. These relative likelihoods were normalized into discrete probability distributions for the recurrence parameters (see Figure 6-3).

6.2.2.2 *Maximum Magnitude*

Most of the large earthquakes that have occurred in the Basin and Range province can be associated with specific faults. For this assessment, we assess the maximum size of an earthquake that might occur on an unrecognizable fault and use this to assign maximum magnitudes to the seismic source zones. Because the hypothesized fault is unrecognized from surface geologic studies, its maximum magnitude is considered to be the largest earthquake that can occur without rupturing the surface (termed the threshold of surface faulting). Wells and Coppersmith (1993) have studied the presence or absence of surface faulting as a function of magnitude. Their studies have shown that the magnitude at which there is a 50% probability of surface faulting is magnitude 6; at magnitude 5.5 the probability is about 20% and at magnitude 6.5 the probability is about 80%. Based on these analyses, we consider the maximum magnitude for an earthquake occurring in the seismic source zones to be uniformly distributed in the range of **M** 5.5 to 6.5, with a mean value of 6.0.

6.3 GROUND MOTION ATTENUATION MODELS

At present, strong motion data recorded in Utah are very limited. In the past, evaluations of seismic hazard, (e.g., Youngs and others, 1987) have typically concluded from examination of the limited strong and weak motion (i.e. seismographic network recordings) that strong ground motion attenuation relationships developed from analysis of California earthquake recordings can be used for Basin and Range sites. However, more recent studies have used examinations of world-wide normal faulting earthquake data together with a variety of modeling techniques to infer that there may be significant differences between strong ground motions in California and those from normal faulting earthquakes in extensional tectonic regimes, such as the Basin and Range region of north-central Utah. Much of this work was reviewed as part of the seismic hazard assessment for the proposed nuclear waste repository at Yucca Mountain, Nevada (CRWMS M&O, 1998). As part of that study, a panel of seven ground motion experts was assembled to provide assessments of the appropriate ground motion models for the Basin and

Range region of southern Nevada. In that study, two basic approaches were used to develop ground motion attenuation relationships, one based on modifications to empirical California strong motion attenuation relationships and one based on numerical modeling. For this study, we utilize the results of the Yucca mountain study to modify California empirical ground motions to the conditions at Skull Valley, Utah. These modifications account for the effects of the characteristics of the earthquake source, the crustal wave propagation path, and the local site geology.

Appendix F describes the analysis of appropriate empirical attenuation models. The Yucca Mountain Ground Motion Expert Panel selected seven empirical ground motion attenuation relationships for modeling rock site motions from normal faulting earthquakes. As discussed in Appendix F, five of these have companion soil site relationships that can be used to assess horizontal ground motions on alluvial soils. These are: Abrahamson and Silva (1997), Boore and others (1997), Campbell (1997), Sadigh and others (1997), and Spudich and others (1997). The relationships developed by Abrahamson and Silva (1997) and Campbell (1997) can also be used to assess vertical ground motions on soil sites.

With the exception of the Spudich and others (1997) model, the selected empirical attenuation relationships were developed primarily from California strike-slip and reverse faulting earthquake data. The Yucca Mountain Ground Motion Expert Panel developed five alternative sets of scaling factors to adjust these relationships to normal faulting conditions. For this study we adopted these scaling factors, resulting in seventeen alternative attenuation relationships for horizontal motions and seven for vertical motions. We also adopt the relative weights assigned to these as averaged over the seven panel members.

Following the approach used by the Yucca Mountain Ground Motion Expert Panel, we also adjust the selected attenuation relationships for the lower rate of ground motion attenuation (higher Q) in north-central Utah as compared to California, and for the expected difference in the response of the Skull Valley sediments compared to the California alluvial soils represented in the empirical data used to derive the attenuation relationships. These adjustments are described in Appendix F.

Figure 6-9 compares the resulting attenuation relationships for horizontal ground motions. Shown on the plots are the estimated ground motions for peak ground acceleration and 5%-damped spectral acceleration at a period of 1.0 second. Each of the five attenuation

relationships is shown with the multiple scaling factors for seismic source effects. Figure 6-10 presents similar comparisons for the vertical attenuation relationships.

6.4   PROBABILISTIC SEISMIC HAZARD RESULTS FOR GROUND SHAKING HAZARD

Seismic hazard calculations were made for peak ground acceleration and 5%-damped response spectral accelerations at periods of 0.075, 0.1, 0.2, 0.3, 0.5, 1.0, 2.0, and 4.0 seconds for horizontal and vertical motions. For hazard computations, the fault-specific sources were modeled as segmented planar surfaces. The areal source zones were modeled as a set of closely spaced parallel fault planes occupying the source regions outlined in Figure 6-7. The probability density function for distance to earthquake rupture for each source was computed assuming earthquake ruptures were uniformly distributed along the length of the fault plane. The depth distribution for earthquakes was based on the observed depth distribution for well located earthquakes shown on Figure 6-4. The distance density functions were computed consistent with the distance measure used in each of the attenuation relationships. A rectangular rupture area for a given size earthquake is located at a random point on the fault plane. The closest distance to this rectangle was used as the distance measure in the Abrahamson and Silva (1997) and Sadigh and others (1997) models. The same distance was used in the Campbell (1997) model, except that the rupture was not allowed to come shallower than two km. For the Boore and others (1997) and Spudich and others (1997) relationships, the rectangular rupture area on the fault was projected vertically to the surface and the closest distance to this surface projection was used.

The rupture size of an event was specified by the relationship $\ln(\text{area}) = 2.095\text{M} - 7.88$ developed from the results presented in Wells and Coppersmith (1994). The specified relationship gives the mean rupture area for a specific magnitude rather than the median (mean log) rupture area. Studies by Bender (1984) have shown that the use of mean estimates of rupture size in the computation of hazard yields results nearly equal to those obtained when the statistical uncertainty in the size of individual ruptures is incorporated in the analysis. The hazard was computed with the distribution in peak ground motion about the median attenuation relationships truncated at three standard deviations.

Distributions for the annual frequency of exceeding various levels of peak ground acceleration and spectral acceleration were developed by performing hazard computations using Equation **(6-2)** with the input parameters defined by each end branch of the logic trees. The hazard was computed considering the contributions of earthquakes of magnitude **M** 5 and larger ($m^0 = 5$). At each ground motion level, the complete set of results forms a discrete distribution for frequency of exceedance, $v(z)$. The computed distributions were used to obtain the mean frequency of exceeding various

levels of peak ground motion (mean hazard curve) as well as hazard curves representing various percentiles of the distributions. The logic trees represent our best judgement as to the uncertainty in defining the input parameters and thus the computed distributions represent our confidence in the estimated hazard.

6.4.1 Computed Hazard for Horizontal Ground Motions

Figure 6-11 presents the computed mean peak hazard and the 5th- to 95th-percentile hazard curves for peak horizontal acceleration and 5%-damped horizontal spectral acceleration at a period of 1.0 second at the CTB site. The uncertainty band is about ¾ of an order of magnitude in frequency of exceedance at low ground motion levels to an order of magnitude at large ground motion levels. The uncertainty in the computed hazard also increases as one considers longer period ground motions. The distribution in computed frequency of exceedance is somewhat skewed with the mean frequency of exceedance lying above the median.

Figure 6-12 shows the contributions of the various seismic sources to the total hazard. The dominating sources are the Stansbury and the East-Springline faults. The relative contribution of the Stansbury fault increases for long period ground motions because of the potential for the occurrence of larger earthquakes than on the Skull Valley faults (see Figure 6-6).

Figure 6-13 shows the relative contribution of events in different magnitude intervals to the computed mean hazard. Each plot in the figure presents a histogram of the percent contributions of events in 0.25 magnitude unit-wide intervals separated by distance from the site. Histograms are presented for peak acceleration and spectral acceleration at a period 1.0 seconds for mean annual frequencies of exceedance of 2×10^{-3}, 5×10^{-4}, and 10^{-4} (return periods of 500, 2,000 and 10,000 years, respectively). The hazard is dominated by ground motions from nearby M 6 to 7 events, consistent with the dominance of the Stansbury and East-Springline faults.

The distributions in the computed hazard shown on Figure 6-11 represent the cumulative effect of all levels of parameter uncertainty included in the hazard model logic trees. The relative contribution of various components of the model to the overall uncertainty can be readily identified from the logic tree formulation. This is accomplished by selecting the node for the parameter to be examined and then computing the hazard, giving each branch in succession a weight of unity and all other branches at that node zero weight. For example, the contribution of uncertainty in selecting the appropriate attenuation relationship can be obtained by computing the mean hazard assuming each of the five attenuation relationships is, in turn, the "correct" relationship, with weight of 1.0, and the other four have zero weight. The resulting hazard curves

are shown on Figure 6-14. In the plots, the heavy solid curve corresponds to the mean hazard and the light solid curves the 5th- and 95th-percentiles of the distribution in exceedance frequency from Figure 6-11. The five labeled curves are the resulting conditional mean hazard for each of the attenuation relationships. These are then mean results over the alternative source scaling relationships applied to each attenuation relationship (see Appendix F, Table F-1). The difference between the conditional means represent the uncertainty in the computed hazard due to uncertainty in selecting the appropriate attenuation relationship. The results shown on Figure 6-14 indicate that the choice of attenuation relationship is a major contributor to uncertainty in the hazard, particularly for long period ground motions.

Figures 6-15, 6-16, and 6-17 show the effect of the alternative modeling of the Skull Valley faults (see Figure 6-5) on the hazard computed from these sources alone. Figure 6-15 shows the effect of the alternative models for the geometry and extent of the West fault. As can be seen from the figure, the alternative models have little effect on the hazard. This is because the East fault dominates the hazard from the Skull Valley faults due to its higher assessed slip rate (see Figure 6-12) and the alternative models for the West fault have only a minor effect on the parameters for the East fault. Similarly, Figure 6-16 shows that consideration of the West fault as an independent source or as a secondary feature for the west fault has a minimal impact on the hazard. Figure 6-17 shows the effect of considering the East and Springline faults to be separate segments or to be linked into a single fault. Considering them to be combined into a single fault produces slightly higher hazard at low probabilities of exceedance and for longer period motions because of the potential for large magnitude earthquakes to occur on the combined source than when they are considered to be separate segments.

Figure 6-18 compares the computed hazard in the western portion of the site area to the hazard at the CTB building. The hazard at the two locations is nearly identical.

6.4.2 Computed Hazard for Vertical Ground Motions

Figure 6-19 presents the computed mean peak hazard and the 5th- to 95th-percentile hazard curves for peak vertical acceleration and 5%-damped vertical spectral acceleration at a period of 1.0 second at the CTB site. The uncertainty band is for vertical peak acceleration hazard is similar to that obtained for horizontal peak acceleration, while the uncertainty for vertical spectral acceleration hazard is somewhat smaller that that obtained for horizontal spectral accelerations.

Figure 6-20 shows the contributions of the various seismic sources to the total hazard for vertical motions. The dominating sources are the Stansbury and the East-Springline faults.

Figure 6-21 shows the effect of the alternative attenuation relationships on the mean hazard for vertical motions. There is greater spread in the hazard results for peak vertical acceleration than for vertical spectral acceleration because the vertical spectral acceleration attenuation relationships produce more similar estimates than the vertical peak acceleration attenuation relationships at close distances (see Figure 6-10).

6.4.3 Contributions to Uncertainty

Figure 6-22 summarizes the contributions to the uncertainty in the total hazard at the CTB site. The plots present histograms showing the relative contribution of the various components of the uncertainty model (logic trees) to the uncertainty in the total hazard at ground motion levels corresponding to a return period of 2,000 years. The components are listed across the bottom and are in order: empirical attenuation model, earthquake source scaling factor (California to normal faulting), maximum seismogenic depth of faulting, alternative models for the West fault geometry, independence of the West fault, fault segmentation, fault activity, fault dip, maximum magnitude, seismic source recurrence rate, b-value of exponential portions of recurrence relationships, and magnitude distribution model. The major contributors to the uncertainty in the hazard are the selection of the alternative attenuation relationships, and assessment of maximum magnitude, recurrence rate and form of the magnitude distribution for the faults.

6.4.4 Comparison of 2,000-yr Equal-hazard spectrum with Design Basis Ground Motions

Figure 6-23 shows the mean hazard curves for peak ground acceleration and 5%-damped spectral acceleration at eight spectral periods for horizontal and vertical motions. These hazard curves were interpolated to obtain ground motions with a return period of 2,000 years (annual frequency of exceedance of 5×10^{-4}). Figure 6-24 compares the resulting equal-hazard spectra with the design-basis response spectra. The design-basis ground motions envelop the 2,000-yr return period equal-hazard spectrum at all spectral periods. The design basis motions correspond to ground motion levels with return periods in the range of 3,000 to 5,000 years for spectral periods less than about 0.5 seconds and to ground motion levels with return periods in the range of 15,000 to 20,000 years for spectral periods larger than 1.0 second.

7.0   FAULT DISPLACEMENT HAZARD ASSESSMENT

The fault evaluation studies documented in this report have shown that capable faults have been identified in the site vicinity. Consistent with the requirements of Part 72 and Part 100.23 (as described in Reg. Guide 1.165), a comprehensive, integrated program was conducted to evaluate the faults. The fault evaluation was focused on identifying the location, geometry, recency, slip history, and associated uncertainties. All of this information, including the uncertainties, was quantified in the logic trees for each fault described previously. In order to quantify the hazard associated with coseismic fault displacement, a probabilistic fault displacement hazard analysis (PDHA) was conducted. As discussed in detail below, the PDHA methodology used is consistent with the methodology developed for the Yucca Mountain potential repository (USDOE Topical Report YMP/TR-003-NP, Rev. 2 Preclosure Seismic Design Methodology for a Geologic Repository at Yucca Mountain).

Analogous to vibratory ground motion analyses, the results of a PDHA are expressed as "hazard curves" that express the probability (or annual frequency) of exceeding various levels of displacement. Because fault displacement hazard varies spatially, the hazard curves are developed for particular locations within the PFSFsite. As discussed further below in the methodology section, the PDHA takes into account the potential for displacement on both principal faults and on secondary faults.

Probability Level of Interest

In the same manner as for ground motion hazard, a probability level of interest must be considered. As discussed in Section 6, the approach that we have taken to arrive at the probability level for ground motions is consistent with the NRC staff's desire for a risk-informed graded approach. Such an approach takes into consideration the consequences associated with the possible failure of a system in arriving at the probability level of interest. As such, the hazard probability levels associated with a dry cask storage system are deemed to be higher than those considered appropriate for a nuclear power plant. In considering the consequences of possible failure of a dry cask storage system, the consequences associated with fault displacement (i.e., cask tip-over) are comparable to those associated with vibratory ground motions. Therefore, an equivalent probability level of interest (5×10^{-4} per year, or 2,000-yr return period) is judged to be appropriate for fault displacement hazard as well as ground motion hazard. This is the probability level that is entered on hazard curves for locations within the site.

The displacements associated with the 5×10^{-4} per year probability level are less than 0.1 cm. In terms of the effects on the facility, the hazard from fault displacement is less than the displacements that have been assumed as being possible from soil settlement. As discussed in SAR Section 4.2.3.5.3, settlement analyses have been based on settlements of about 3 inches (7 cm).

7.1 METHODOLOGY FOR PROBABILISITIC ASSESSMENT OF FAULT DISPLACEMENT

At the present time, methodologies for the probabilistic assessment of fault displacement hazard. The most comprehensive probabilistic seismic hazard analysis for fault displacement hazard was recently completed for the proposed nuclear waste repository at Yucca Mountain, Nevada (CRWMS M&O, 1998). The approach used to conduct the PSHA fault displacement hazard assessment at the Skull Valley site is based primarily on the extensive methodology development presented in CRWMS M&O (1998).

7.1.1 Principal and Distributed Fault Displacement

The potential for fault rupture within the site area can be described in terms of two types of fault rupture: *principal faulting* and *distributed faulting*. These are illustrated on Figure 7-1, which shows the surface rupture pattern for the 1959, M 7.4 Hebgen Lake earthquake. Principal faulting is faulting along the main plane (or planes) of crustal weakness responsible for the release of seismic energy during the earthquake. Where the principal fault rupture extends to the surface, it may be represented by displacement along a single narrow trace or over a zone that is a few to many meters wide. The faults of concern are those that may produce earthquakes (i.e., are directly related to the primary source of energy release).

Distributed faulting is defined as rupture that occurs on other faults, shears, or fractures in the vicinity of the principal rupture in response to the principal displacement. It is expected that distributed faulting will be discontinuous in nature and occur over a zone that may extend outward several tens of meters to many kilometers from the principal rupture. A fault that can produce principal rupture may also undergo distributed faulting in response to principal rupture on other faults. The extent to which faults that can undergo distributed rupture can be identified depends on the level of detailed mapping. It is a matter of interpretation and is, therefore, less certain than for principal faulting. The resulting of the detailed studies of faulting in the site area (Section 5.2) indicate that there are no principal faulting sources extending through the

location of the proposed storage facility. Therefore, only distributed faulting hazard will be considered here.

7.1.2 Basic Formulation

The formulation for probabilistic evaluation of the hazard from fault displacement is analogous to that developed for the hazard from ground shaking. The fault displacement PSHA addresses how frequently it occurs and how large the displacements are. The hazard can be represented probabilistically by a displacement hazard curve, Figure 7-2, that is analogous to ground motion hazard curves. The hazard curve shown on Figure 7-2 represents the hazard at a point within the site area. It relates the amount of displacement in a *single* event to how often larger displacements occur (i.e., the frequency of exceeding a specified amount of displacement). Reading from the example hazard curve shown on Figure 7-2, single event displacements larger than 10 cm occur with a frequency of 10^{-4} per year (a return period of 10,000 years); single event displacements larger than 50 cm occur with a frequency of 10^{-5} per year (a return period of 100,000 years). Thus, the hazard curve is a plot of the frequency of events exceeding fault displacement value d, designated by $v(d)$. This frequency can be computed by the expression:

$$v(d) = \lambda_{DE} \cdot P(D > d) \tag{7-1}$$

where λ_{DE} is the frequency at which displacement events occur on the structure located at the point of interest, and $P(D > d)$ is the conditional probability that the displacement in a single event will exceed value d.

As with ground motion PSHA methodology, the formulation given by Equation (7-1) represents the randomness in the natural phenomena of earthquake-induced fault displacement (termed aleatory uncertainty). The scientific (epistemic) uncertainty is represented in the process of selecting the appropriate models and model parameters for the fault displacement hazard characterization. The logic tree methodology described in Section 3 was utilized to characterize the uncertainty in the fault displacement PSHA.

7.1.3 Estimation of Frequency of Displacement Events

The approaches for estimating the frequency of displacement events can be divided into two categories. The first, designated the *displacement approach*, provides an estimate of the frequency of displacement events directly from feature-specific or point-specific data. The second, designated the *earthquake approach*, involves relating the frequency of slip events to the

frequency of earthquakes on the various seismic sources. Both approaches are used for assessing the fault displacement hazard for principal faulting and distributed faulting.

7.1.3.1 Displacement Approach

The displacement approach estimates the frequency of displacement events, λ_{DE}, from the information available for the specific feature (point) in question. There are two techniques for direct estimation of λ_{DE}: the estimation of recurrence intervals and the use of slip rate.

Recurrence Interval Technique

An example of the recurrence interval technique is the assessment of the frequency of displacement events on a source of principal faulting using paleoearthquake data. This assessment can be used directly in assessing the frequency of faulting events.

Slip Rate Technique

Fault slip rate, SR, is a measure of the amount of slip averaged over a time period that encompasses multiple ruptures. If the slip rate and the average slip in a faulting event, $\bar{D}_E$, are known, then λ_{DE} can be estimated by:

$$\lambda_{DE} = SR / \bar{D}_E \tag{7-2}$$

Given SR, the use of Equation (7-2) requires an estimate of the average slip in an event, $\bar{D}_E$. For some features (typically those that may be locations of principal faulting), this may be assessed directly from trenching data. For other features, scaling relationships that relate $\bar{D}_E$ to fault length, L, or cumulative fault displacement, D_{cum} must be used.

The displacement approach does not tie slip events to specific earthquakes, it only evaluates the frequency of slip events. Thus, the displacement approach does not explicitly distinguish between principal and distributed ruptures on a feature.

7.1.3.2 Earthquake Approach

The earthquake approach utilizes the earthquake recurrence models developed for the ground shaking hazard assessment. A model for assessing the frequency of earthquakes on each seismic source is presented in Section 6. The occurrence of an earthquake on source j may induce slip on the feature of interest, point i. The probability that slip will occur given an event

on source j, P_i(Slip|Event on j), can range from 0 to 1.0. The frequency of displacement events, λ_{DE}, is obtained by summing the contributions from all of the seismic sources:

$$\lambda_{DE} = \sum_{j=1}^{n} \lambda_j \text{(Events on source } j\text{)} \times P_i \text{(Slip|Event on source } j\text{)} \qquad (7\text{-}3)$$

As defined by Equation **(7-3)**, the earthquake approach for assessing the frequency of displacement events consists of two parts, an evaluation of the opportunity frequency, the frequency of earthquakes, and an evaluation of the probability each opportunity will result in fault slip. Because the earthquake approach is tied directly to the occurrence of earthquakes on various sources, the distinction between principal and distributed faulting events is maintained. The methods used to evaluate P_i(Slip|Event on j) depend on whether one is considering principal ($j = i$) or distributed ($j \neq i$) faulting.

For distributed faulting, P_i(Slip|Event on j) expresses the likelihood that slip on an earthquake source some distance r from the feature of interest will trigger slip locally. Pezzopane and Dawson (1996) developed a data base of distributed ruptures resulting from historical earthquakes in the western United States. These data were used to assess the density of distributed ruptures as a function of distance from the principal rupture. The process used was to place a 0.5 km × 0.5 km grid on each map of surface ruptures. The number of grid cells that contain a secondary rupture divided by the total number of grid cells at a given distance from the principal rupture provides a measure of the frequency or likelihood that a distributed rupture will occur. Figure 7-3 shows a plot of these data segregated by magnitude and by location in the hanging wall block and foot wall block of the rupture. The data show a decrease in the likelihood of experiencing distributed rupture with increasing distance from the principal rupture. The data also show clear differences between the hanging wall and foot wall sides of the rupture. The size (magnitude) of the earthquake magnitude appears to provide some control on the maximum distance distributed rupture has been observed from the principal faulting.

The probability of occurrence of distributed faulting on a feature located r km from a magnitude m earthquake can be determined from these data using the logistic model.

$$P_i \text{(Slip} \mid \text{Event on } j\text{)} = \frac{e^{f(m,r)}}{1 + e^{f(m,r)}} \qquad (7\text{-}4)$$

where $f(m,r)$ represents a suitable function of distance and magnitude. The data shown on Figure 7-3 indicate that $f(m,r)$ should account for the effect of being on the hanging wall or foot wall sides of the principal rupture. Appendix H of CRWMS M&O (1998) presents models fit to these data. The model used in this study, shown by the curves on Figure 7-3, is based on an updated analysis of these data conducted for the Los Alamos National Laboratory (Olig and others, 1998). The relationship is

$$f(m,r,h,\tau) = 3.27 + (-8.28 + 0.577m + 0.629h) \cdot \ln(r + 4.14) + 0.611\tau \qquad (7\text{-}5)$$

where h is 1.0 if the site lies in the hanging wall of the rupture and 0.0 is the site lies in the foot wall, and τ is a random variate with 0 mean that accounts for variability from earthquake to earthquake..

This probability is considered an aleatory probability because it defines the likelihood of the occurrence of distributed faulting at a point in a single earthquake.

7.1.4   Conditional Probability of Exceedance

The conditional probability of exceedance, $P(D > d)$, in Equation (7-1) defines the probability that the amount of displacement occurring at a point during a single displacement event will exceed a specified amount d. The probability can be considered to contain two parts, the variability of slip from event to event, and the variability of slip along strike during a single event. The first part represents a distribution for the "size" of faulting events and is analogous to an earthquake magnitude distribution model used in the ground shaking hazard analysis. The second part represents the variation of the displacement from point-to-point along a rupture of a given size. This might be considered analogous to the lognormal distribution for peak ground motion about the median value predicted by an attenuation law for a specific magnitude and distance.

A variety of approaches for evaluating the distribution for slip at a point in an individual event were developed in CRWMS M&O (1998). Some methods utilize the two part representation of displacement variability; others combine them into a single distribution function. The various methods are described below as they are applied to principal and distributed faulting. The approaches also differ depending on whether the earthquake or displacement approaches are being used for the assessment.

7.1.4.1 Two Step Approach for Conditional Probability of Exceedance

The two step approach for assessing the conditional probability of exceedance was used to define the distribution for the amount of distributed displacement occurring on a secondary fault in the earthquake approach. The SDO expert team for the Yucca Mountain PSHA (CRWMS M&O, 1998) developed an estimate of the largest distributed displacements likely to occur on secondary faults expressed as a fraction of the maximum displacement that occurs on the principal rupture, MD. Figure 7-4 shows the empirical relationship between $D_{distributed}$ /$MD_{principal}$ and distance from the principal rupture developed by the SDO expert team. This curve is assumed to represent an upper percentile of the distribution for $D_{distributed}$/$MD_{principal}$, which is assumed to be a gamma distribution with a shape parameter, a, equal to 2.5. For example, the 95th percentile of a gamma distribution with a equal to 2.5 occurs at x/b equal to 5.535. Setting x equal to $D_{distributed}$/$MD_{principal}$, the value of parameter b at a given distance from the principal rupture is found by dividing the value of $D_{distributed}$/$MD_{principal}$ shown on Figure 7-4 by 5.535. The conditional probability of exceedance, $P(D>d)$, is then obtained by convolving the gamma distribution for $D_{distributed}$/$MD_{principal}$ with the lognormal distribution for MD.

7.1.4.2 Single Step for Conditional Probability of Exceedance

The single step approach for assessing $P(D>d)$ is used in the displacement approach. The method involves developing a distribution for D/D_{norm}, where D_{norm} represents a representative measure of the amount of displacement at the location of interest. A logical choice for D_{norm} is the average displacement per event, $\bar{D}_E$. The distribution of $D/\bar{D}_E$ represents the variability in the displacement at a point in a single event about the average displacement over multiple events. This distribution is not the same as the distribution for D/AD defined above. The latter represents the variability in displacement along the length of a rupture about the average value of displacement for that rupture.

Figure 7-5 shows three distributions for $D/\bar{D}_E$ developed as part of the assessments for Yucca Mountain (CRWMS M&O, 1998). The distribution labeled DFS was developed by normalizing individual event displacements from a single trench location by their average and then pooling all of the data for trench sites containing three or more events. The distribution labeled SBK_{paleo} was developed by normalizing individual event displacements from a fault by the estimated average displacement for the fault over all events. The distribution labeled SBK_{(W&C)} was developed by normalizing individual event displacements from a fault by the estimated average displacement for the fault based on the Wells and Coppersmith (1994) empirical relationship between average displacement and fault length. All three empirical

distributions were fit by gamma distributions, shown by the solid curves on Figure 7-5. The conditional probability of exceedance, $P(D>d)$, is computed using the cumulative density function for a gamma distribution.

7.2 FAULT DISPLACEMENT HAZARD CHARACTERIZATION

Quaternary faults in the vicinity of the site that could pose a fault displacement hazard include:

- Fault D1 and the F faults, which are small intrablock faults on the down-thrown side of the East fault that are imaged on the high-resolution seismic survey as displacing the unconformity between the Promontory soil and the base of the Bonneville alloformation (i.e., the Qp unconformity).

- Faults C1 and C3, which are small intrablock faults on the down-thrown side of the East fault that are imaged on the high-resolution seismic survey as displacing the unconformity at the top of the Tertiary Salt Lake Group (i.e., the T/Q unconformity) but do not appear to offset the Qp unconformity.

In addition to the potential for displacement on these mapped faults, the potential for deformation in the areas between the mapped Quaternary faults also is evaluated (e.g., the occurrence of broad zones of distributed faulting and/or movements on faults too small to map completely).

The displacement hazard model logic tree is shown on Figure 7-6. Consistent with the displacement hazard assessment performed for the Yucca Mountain site, we use both the earthquake approach and the displacement approach to assess the hazard. The relative weights assigned to these two approaches are 0.63 for the displacement approach and 0.37 for the earthquake approach. These weights represent the average across the six Yucca Mountain Source Characterization Expert Teams.

As discussed above in Section 7.1.4.2, the distribution for the amount of displacement on a distributed rupture uses the curve shown on Figure 7-4 as the 95th percentile of a gamma distribution for $D_{distributed}/MD_{principal}$. As discussed in Olig and others (1998), there is uncertainty about whether there is sufficient data to imply that the curve shown on Figure 7-4 is a 95th percentile. Therefore, we also considered the curve to represent an 85th percentile as an alternative approach.

The remaining source characterization parameters for the earthquake approach are identical to those used for the ground motion hazard assessment presented in Section 6.

For the displacement approach, the required parameters are the distribution for $D/\bar{D}_E$ and for each fault the average displacement per event and the fault slip rate. We utilize the three alternative distributions for $D/\bar{D}_E$ shown on Figure 7-5 and give them equal weight, having no preference for one over the other. The fault-specific parameters are described below.

Displacement and slip rate data at specific locations are presented in Section 5. Based on these data, slip-rate and slip-per-event distributions are developed that characterize the overall uncertainty in these parameters. In addition to uncertainties related to the age of the displaced datum and the amount of cumulative displacement, which were discussed previously, the slip-rate distributions should also include uncertainties related to the limited sample size and the relation between the measured values at specific locations to the average value along the section of fault of concern. The range of values and probability weights used to characterize the faults in the probabilistic analysis are described in the following sections.

7.2.1 Fault D1

Fault D1 is a small, down-on-the-west, intrablock normal fault. It displaces the Qp reflector on seismic line 98-C across the northern boundary of the site and on seismic line 98-A, which passes through the center of the site. On line 98-C the estimated displacement is 1.7 m. On line 98-A it is 0.8 m and on the lines to the south the displacement is barely detectable. The vertical stratigraphic separation of the Promontory soil based on boreholes across the fault where it is imaged on seismic line 98-A is 0.7 m (i.e., between boreholes C-18 and C-30). Displacements observed in Trench T-1, which may cross the southern projection of fault D1, range from < 4 cm to about 15 cm. The maximum vertical stratigraphic separation on the base of Post-Little Valley sand ramp deposits (unit Q2b in Trench T-1) across the zone of closely spaced fractures is 0.5 to 0.7 m.

Slip Rate

Table 5-5 presents estimates of the slip rate on fault D-1 based on the displacement of the Qp reflector. The Qp reflector is interpreted to correspond to the Promontory soil, which is estimated to be 55 ±5 ka and this age range is used to calculate the slip rates presented on Table 5-5. The Promontory soil is overlain by Bonneville Lake sediments that are only 28ka and appear to be displaced the same amount as the Promontory soil. This suggests a long interval (approximately 55 ka to 28 ka) with no displacement on fault D-1. Alternatively, some displacement could have occurred during this interval, but the scarps were eroded during the transgression of Lake Bonneville. This is very unlikely because the Promontory soil is

preserved on the upthrown side of the fault. To account for this uncertainty, slip rates for fault D-1 are estimated using two approaches.

The first approach assumes that values presented in Table 5-5, which are based on the cumulative displacement of the Promontory soil, are an accurate measure of the average late Pleistocene slip rate. Because the Promontory soil is preserved on both sides of the fault, this is the preferred interpretation, and this approach is assigned a probability weight of 0.8. The calculated slip rates (Table 5-5) ranges from 0.032 ± 0.003 mm/yr at the northern border of the site to less than 0.012 mm/yr south of the site. The average slip rate is therefore likely to be in the range of 0.01 mm/yr to 0.04 mm/yr. Values in the central part of this range are assigned slightly higher weight than the end values. Given this approach, the range of slip-rate values for Fault D1 considered in the fault displacement analysis and the assigned probability weights are: 0.01 mm/yr [0.2]; 0.02 mm/yr [0.3]; 0.03 mm/yr [0.3]; and 0.04 mm/yr [0.2].

In the second approach, which is assigned a weight of [0.2], the displacement is averaged over 28 ka and the slip rates are assumed to be twice the rates given above for the first approach. Accordingly, the slip rate values and assigned probability weights given the second approach are: 0.02 mm/yr [0.2]; 0.04 mm/yr [0.3]; 0.06 mm/yr [0.3]; and 0.08 mm/yr [0.2].

Average Slip Per Event

The average displacement on the Qp reflector along fault D1 at the site is less than 1 m. The stratigraphic relations indicate that the 0.7 m cumulative displacement on the Promontory soil measured between boreholes C-18 and C-30 was probably produced by more than one event and the deformation may be distributed across a 30- to 45-m-wide zone as evidenced by apparent displacements in the top of the Pre-Stansbury trangressive facies (Plate 4). The average slip per event is probably less than 0.7 m (assuming more than one event) and greater than 0.1, which would suggest there have been several events (about 7, which is considered very unlikely). The range of values considered in the fault displacement analysis for the average slip per event on Fault D1 is: 0.7 m [0.05]; 0.4 m [0.4]; 0.2 m [0.4]; and 0.1 m [0.15].

7.2.2   Faults F1/F3 and F2/F4

The F faults are a series of small down-to-the east and down-to-the west normal faults. imaged in the Qp reflector to the west of the site (See Section 5.2 and Plate 4). The F faults do not extend under the site and, therefore, do not pose a threat to the proposed PFSF. The well-constrained displacement data on the F faults (Table 5-4) provide a useful basis for constraining the potential for displacement on other intrablock faults in the site vicinity. The F faults have

larger Quaternary displacement than the other intrablock faults. Therefore, the potential for fault-rupture on the other faults is expected to be less than the F faults.

On seismic line 98-A, the F faults define a small graben (faults F1 and F3) and a narrow horst (faults F2 and F4). They can be traced to the north to seismic line GSI-UT-34 (at shotpoint 227) and to the south to seismic line 98-D. Due to poor data quality, they are not imaged on seismic line 98-B. To the south, the faults project through the eastern end of the Stansbury gravel bar.

Average Slip Rate

Based on the amount of offset of the Qp reflector, calculated slip rates on the F faults range from 0.005 mm/yr to almost 0.04 mm/yr (Table 5-4). Based on closely spaced boreholes (Figure 5-4), the average slip rate (post Promontory soil) across the F1/F3 graben is 0.016 ±0.001 mm/yr. If all the post-Promontory soil displacement occurred during the past 28 ka, it suggests the shorter-term slip rate could be as high as 0.04 mm/yr. The survey of the Stansbury bar suggests the gravel bar may be displaced about 0.6 m down-on-the-west across the projected southern extension the F faults. This suggests a slip rate of about 0.03 mm/yr. Based on these data, the slip rate is well constrained between about 0.01 mm/yr and 0.04 mm/yr, with the preferred rate in the range of 0.2 to 0.3 mm/yr. The range of slip-rate values for the F faults considered in the fault displacement analysis and the assigned probability weights are: 0.04 mm/yr [0.1]; 0.03 mm/yr [0.3]; 0.02 mm/yr [0.5]; and 0.01 mm/yr [0.1].

Average Slip Per Event

The most reliable displacement data on the F faults are from the series of closely spaced boreholes across the F1/F3 graben (Figure 5-4). The net vertical stratigraphic separation on the Qp unconformity across the F1/F3 graben is 0.9 m and the displacement across individual traces, based on the borehole data, range from about 0.5 m to 1.4 m. The displacement decreases upwards within the Bonneville alloformation indicating the cumulative displacement of the Qp unconformity was produced by multiple events.

The average slip per event on the F faults is probably significantly less than largest cumulative offset reported on a single trace (1.4 m), which is interpreted to have been produced by multiple events. A displacement of 30 to 45 cm during a single event is considered a likely upper limit for the net slip during a single event (i.e., assuming the 0.9-m cumulative displacements across the F1/F3 graben and the F/2.F4 horst were produced by at least 2 or 3 events). The average slip per event is probably greater than 5 cm would suggest there have been more than 15

surface faulting events post-Qp and implies a recurrence interval of less than 3,000 to 4,000 years. Displacements on individual traces within a zone containing both down-on-the-west and down-on-the-east movements might be larger than the net slip across the zone. Given the overall uncertainty, a wide range of values is considered for the average slip per event with the greatest weight assigned to values that are consistent with 2 or 3 events post-Qp. The range of values considered in the fault displacement analysis for the average slip per event on the F faults is: 0.9 m [0.05]; 0.6 m [0.43]; 0.3 m [0.42]; and 0.05 m [0.1].

7.2.3 Faults C1 and C2

Faults C1 and C2 are imaged on seismic lines 98-C and 98-A where they displace the Q/T reflector and die out upwards before reaching the Qp reflector (Bay Geophysical Associates, 1999, Table 5-1). Bay Geophysical Associates (1999) estimated the displacement of the Q/T reflector to be 0.7 m or less (based on an average velocity of 1100 ft. per second) (Table 5-1). The actual displacements are uncertain because the shear-wave velocity is not precisely known and the apparent offsets of the Q/T reflector have not been verified with boreholes.

Slip Rate

The Quaternary lacustrine deposits overlying the Tertiary Salt Lake Group at the site are Little Valley in age or older. Therefore, the Q/T unconformity is a minimum of 160 kyr old (Section 3.1 and Table 3-2). Using the calculated displacement of the Q/T reflector (0.7 m) and an age of >160 ka gives a slip rate of <0.004 mm/yr. Given a detection threshold of 0.4 m for displacement of the Qp reflector (Bay Geophysical Associates, 1999) and a minimum age of 50 ka suggests a slip rate of <0.008 mm/yr. Elsewhere, one- to two-foot (0.6-m) displacements were identified in the Qp reflector based on the seismic survey. These displacements were subsequently verified based on borehole data. Therefore, the survey resolution conservatively can be taken as < 0.7 m. This suggests an upper bound of 0.01 mm/yr for the slip rate on faults that do not displace the Qp reflector. Slip rates ranging from 0.001 to 0.02 mm/yr were included in the probabilistic assessment with most weight given to the low end of this range. The slip-rate distribution used in the analysis is: 0.001 mm/yr [0.3]; 0.005 mm/yr [0.5]; 0.01 mm/yr [0.1]; and 0.02 mm/yr [0.1].

Average Slip Per Event

Faults C1 and C2 do not appear to displace the Qp reflector. Presumably, the potential for slip on these faults is less than the potential for slip on the F faults, which have had at least two events that post-date the Qp reflector. The post Q/T displacements on the C and the F faults are similar (less than 5 milliseconds), which suggests their long-term behavior may be similar. The

range of values used to characterize the average slip per event on the C faults is similar to the one used to characterize the F faults except that the maximum value considered was assumed to be 0.7 m (the detection resolution for displacement on the Qp reflector) and more weight is given to smaller displacements. Smaller displacements are considered more likely because of the absence of evidence for discrete breaks in the Qp reflector. If there has been post-Qp deformation, it is probably distributed over a zone of warping and/or multiple small offsets. The distribution for the average slip per event used in the probabilistic analysis is: 0.02 m [0.25]; 0.1 m [0.3]; 0.2 m [0.3]; 0.4 m [0.1]; and 0.7 m [0.05].

7.2.4   Distributed Faulting Between Mapped Faults

The high-resolution seismic survey successfully imaged faults having very small (less than 0.6 m) cumulative offset in the Promontory soil (i.e., the Qp reflector). The potential for displacement in the areas between the mapped faults is very low, but this potential for small displacements is included in the displacement hazard analysis.

Fractures in the Bonneville deep-water facies were observed in several of the test pits and in Trench T-2. Careful mapping of the fractures (Plate 3) shows that (1) the general north-south trend of the fractures is compatible with the regional pattern of east-west Basin and Range extension, (2) the fractures die out downwards and do not cut the thin marker beds within underlying sandy Bonneville trangressive facies, and (3) there is no vertical displacement across most of the fractures indicating that the cumulative deformation during the past 15ka to 20ka is very small. Nontectonic mechanisms for these fractures are viable. Sixty four fractures were mapped in the 88-m-long trench. Of these, only 11 had measurable displacement. The amount of displacement on the mapped fractures is listed below.

Number of Fractures	Vertical Displacement	Percentage of Total
53	0	83 %
3	1.0 cm	5 %
6	2.0 cm	9 %
2	2.5 cm	3 %
Total 64		100 %

Based on the trench wall mapping, the average fracture spacing is between 1 to 1.5 m per fracture. These displacements are all smaller than the amount of settlement considered in the design.

7.3 PROBABILISTIC SEISMIC HAZARD RESULTS FOR FAULT DISPLACEMENT HAZARD

The computational scheme used to compute the displacement hazard is essentially the same as that used to compute the ground shaking hazard (Section 6). The probabilistic assessment of ground shaking hazard consists of three basic components: a characterization of the frequency of occurrence of earthquakes of various magnitudes on each of the seismic sources; a characterization of the distribution of the distance from the site to earthquakes on each seismic source, and a characterization of the distribution of the level of ground motion for a given magnitude and source-to-site distance. These same three components are used in the "earthquake approach" for the probabilistic assessment of fault displacement hazard. The frequency of earthquakes on each of the seismic sources is computed in an identical manner to that used in the ground motion assessment (Section 6). In the assessment of ground shaking hazard, it is assumed that every earthquake produces some level of ground shaking, thus the frequency of shaking events is equal to the frequency of earthquakes. However, in the assessment of fault displacement hazard, not every earthquake is assumed to produce surface rupture. Therefore, the frequency of displacement events is equal to the frequency of earthquakes times the probability that an individual earthquake will produce surface rupture [Equation (7-5)]. For distributed faulting, the distance measure is of the same type as that used in the ground motion assessment and the same computational scheme is used.

The third component of ground shaking hazard assessment consists of a ground motion attenuation relationship defining the probability that a specific ground motion level will be exceeded, given the earthquake magnitude and the source to site distance. The equivalent "attenuation" relationships in the assessment of fault displacement hazard are the various distributions for the amount of displacement defined in Section 7.1.4.1.

The computation of fault displacement hazard using the "displacement approach" is a simpler process. The frequency of displacement events is defined directly by the use of Equation (7-2). There is no distance distribution function because it is assumed that these events occur at the site of interest. The "attenuation" relationship is an assessment of the variability of displacements in individual events about an average value for all events at the site of interest (Figure 7-5).

Fault displacement hazard analyses were conducted for three locations: at Faults C, D, and F. Figure 7-7 shows the fault displacement hazard results for the three locations. Each plot shows the mean hazard curve and curves tracing various percentiles of the distribution for the

frequency of exceeding specific displacement values. The displacement hazard curves display a characteristic shape that is different from that of a typical ground motion hazard curve. In the earthquake approach, the primary contributors to displacement hazard are the larger events occurring within a few kilometers of the site, due to the displacement hazard associated with distributed faulting.. Therefore, the larger number of smaller and/or distant events that contribute to ground shaking hazard at low ground motion levels have no contribution to displacement hazard. Thus, the frequency of exceedance is limited by the frequency of these large events occurring at or in the immediate vicinity of the site. In the displacement approach, the frequency of all displacement events occurring at the site is specified directly and the frequency of exceedance of a specific displacement value must be less than or equal to the frequency of displacement events.

The uncertainty in the hazard results are represented by the percentile curves and the distribution is skewed, with the mean hazard lying near the 75th percentile of the distribution.

Figure 7-8 shows the contribution of the various seismic sources to the hazard computed using the earthquake approach. The hazard is dominated by contributions from the East fault with a minor contribution from the Stansbury fault.

Figure 7-9 compares the mean hazard results for the earthquake and displacement approaches at the three sites. Each plot also shows the mean hazard and the 5th and 95th percentile hazard curves from Figure 7-7. The earthquake approach produces similar hazard as the displacement approach at Fault C and significantly lower hazard than the displacement approach at the other two sites. The earthquake approach estimates are similar at all three sites and show a gradual decrease in frequency of exceedance as one moves away from the East fault (from Fault C to Fault F).

Figure 7-10 summarizes the contributions to the uncertainty in the total hazard at the three sites. The plots are similar to those shown on Figure 6-22 and list the common components of the ground motion and displacement hazard models plus those additional components used for the displacement hazard assessment. The relative contributions to uncertainty were evaluated for the frequency of exceeding a displacement of 10 cm. The major contributors to the uncertainty in the displacement hazard are the approach for hazard assessment and assessment of slip rate and average displacement per event for each fault.

7.4   SUMMARY OF RESULTS

The probability level of interest for displacement hazard is a return period of 2,000 years (annual frequency of exceedance of 5×10^{-4}). The hazard curves at the three sites all fall below this level, even for the smallest displacement considered. Thus, the 2,000-yr return period displacement due to faulting at the three locations is less than 0.1 cm. For sites between these three locations, the hazard level is less.

8.0 REFERENCES

Anderson, J.G., 1979, Estimating the seismicity from geological structure for seismic risk studies: Bulletin of the Seismological Society of America, v. 69, p. 135-158.

Anderson, J.G., Wesnousky, S.G., and Stirling, M.W., 1996, Earthquake size as a function of fault slip rate, Bulletin of the Seismological Society of America, v. 86, 3, p 683-690.

Anderson, L.W., and Miller, D.G., 1979, Quaternary fault map of Utah: Long Beach, California, Fugro, Inc., 35 p., scale 1:500,000.

Anderson, N.A., and Silva, W.J., 1997, Empirical response spectral attenuation relations for shallow crustal earthquakes: Seismological Research Letters, v. 68, p. 94-127.

Arabasz, W.J., Pechmann, J.C., and Brown, E.D., 1989, Evaluation of seismicity relevant to the proposed siting of a Superconducting Supercollider (SSC) in Tooele County, Utah: Utah Geological and Mineral Survey Miscellaneous Publication 89-1, 107 p.

Arabasz, W.J., Nava, S.J., and Phelps, W.T., 1997, Mining seismicity in the Wasatch Plateau and Book Cliffs coal mining districts, Utah, USA, in Gibowicz, S.J., and Lasocki, S. (eds.), Rockbursts and Seismicity in Mines: Proceedings of the 4th International Symposium on Rockbursts and Seismicity in Mines/Krakow/Poland, August 11-14.

Barnhard, T.P., and Dodge, R.L., 1988, Map of fault scarps formed on unconsolidated sediments, Tooele 1° x 2° quadrangle, northwestern Utah: U. S. Geological Survey Miscellaneous Field Studies Map MF-1990, scale 1:250,000.

Birkeland, P.W., 1984, Soils and Geomorphology: Oxford University Press, New York, 372 p.

Bishop, K.M., 1997, Miocene rock-avalanche deposits, Halloran/Silurian Hills area, southeastern California: Environmental & Engineering Geoscience, v. III, no. 4, p. 501-512.

Bonilla, M.G., 1988, Minimum earthquake magnitude associated with coseismic surface faulting: Bulletin of the Association of Engineering Geologist, v. 25, p. 17-29.

Bonilla, M.G., Mark, R.K., and Lienkaemper, J.J., 1984, Statistical relations among earthquake magnitude, surface rupture length, and surface fault displacement: Bulletin of the Seismological Society of America, v. 74, no. 6, p. 2379-2411.

Boore, D.M., Joyner, W.B., and Fumal, T.E., 1997, Equations for estimating horizontal response spectra and peak acceleration from western North American earthquakes–A summary of recent work: Seismological Research Letters, v. 68, p. 128-153.

Brimhall, W.H., and Merritt, L.B., 1981, The geology of Utah Lake, implications for resource management: Great Basin Naturalist Memoirs Number 5, p. 24-42, scale 1:250,000.

Bucknam, R.C., 1977, Map of suspected fault scarps in unconsolidated deposits, Tooele 1° x 2° sheet, Utah: U. S. Geological Survey Open-File Report 77-495.

Bucknam, R.C., and Anderson, R.E., 1979, Map of fault scarps on unconsolidated sediments, Delta 1° x 2° quadrangle, Utah: U.S. Geological Survey Open-File Report 79-366, 21 p., scale 1;250,000.

Campbell, K.W., 1997, Empirical near-source attenuation relationships for horizontal and vertical components of peak ground acceleration, peak ground velocity, and pseudo-absolute acceleration response spectra: Seismological Research Letters, v. 68, p. 154-179.

Civilian Radioactive Waste Management System Management and Operating Contractor (CRWMS M&O), 1998, Probabilistic seismic hazard analyses for fault displacement and vibratory ground motion at Yucca Mountain, Nevada: U.S. Department of Energy DE-AC04-94AL85000, Prepared for the U.S. Geological Survey, February 23.

Cook, K.L., Bankey, V., Mabey, D.R., and DePangher, M., 1989, Complete Bouguer gravity anomaly map of Utah: Utah Geological and Mineral Survey Map 122, scale 1:500,000.

Cook, K.L., Gray, E.F., Iverson, R.M., and Strohmeier, M.T., 1980, Bottom gravity meter regional survey of the Great Salt Lake, Utah: in Gwynn, J.W. (ed.), Great Salt Lake, a scientific, historical and economic overview: Utah Geological and Mineralogical Survey Bulletin 116, p. 125-143.

Cook, K.L., Montgomery, J.R., Smith, J.T., and Gray, E.F., 1975, Simple Bouguer gravity anomaly map of Utah: Utah Geological and Mineral Survey Map 37, scale 1:1,000,000.

Coppersmith, K.J., and Youngs, R.R., 1986, Capturing uncertainty in probabilistic seismic hazard assessment within intraplate tectonic environments, in Proceedings, Third U.S. National Conference on Earthquake Engineering: Earthquake Engineering Research Institute, v. 1, p. 301-312.

Cornell, C.A., 1968, Engineering seismic risk analysis: Bulletin of the Seismological Society of America, v. 58, p. 1583-1606.

Cornell, C.A., 1971, Probabilistic analysis of damage to structures under seismic loads, in D.A. Howells, Haigh, I.P., and Taylor, C. (eds.), Dynamic waves in civil engineering: John Wiley, London.

Crone, A.J., 1983, Amount of displacement and estimated age of a Holocene surface faulting event, eastern Great Basin, Millard County, Utah, in Gurgel, K.D., (ed.), Geologic excursion in neotectonics and engineering geology in Utah: Utah Geological and Mineral Survey Special Studies, v. 62, p. 49-55.

Currey, D.R., 1980, Coastal geomorphology of Great Salt Lake and vicinity, in Gwynn, J.W., (ed.), Great Salt Lake–A scientific, historical, and economic overview: Utah Geological and Mineral Survey Bulletin, v. 116, p. 69-82.

Currey, D.R., 1982, Lake Bonneville–selected features of relevance to neotectonic analysis: U. S. Geological Survey Open-File Report 82-1070.

Currey, D.R., Atwood, G., and D.R. Mabey, 1983, Major levels of Great Salt Lake and Lake Bonneville; Utah Geological Survey Map 73, 1:750,000-scale plate.

Currey, E.R., Oviatt, C.G., and Plyler, G.B., 1983, Lake Bonneville stratigraphy, geomorphology, and isostatic deformation in west-central Utah: Utah Geological and Mineral Survey Special Studies 62.

Dobrin, M.B., 1976, Introduction to Geophysical Prospecting (third edition): McGraw-Hill, Inc., New York, 630 p.

Dunne, G.C., 1977, Geology and structural evolution of Old Dad Mountain, Mojave Desert, California: Geological Society of America Bulletin, v. 88, p. 737-748.

Eardley, A.J., and Gvosdetsky, V., 1960, Analysis of Pleistocene core from Great Salt Lake, Utah: Geological Society of America Bulletin, v. 71, p. 1323-1344.

Eardley, A.J., Shuey, R.T., Gvosdetsky, V., Nash, W.P., Picard, M.D., Grey, D.C., and Kukla, G.J., 1973, Lake cycles in the Bonneville basin, Utah: Geological Society of America Bulletin, v. 84, p. 211-216.

Electric Power Research Institute (EPRI), 1988, Seismic hazard methodology for the Central and Eastern United States: NP-4726-A (revised), v. 1-10.

Electric Power Research Institute (EPRI), 1993, Guidelines for determining design basis ground motions: EPRI TR-102293, v. 1-5.

Everitt, B.L., and Kaliser, B.N., 1980, Geology for assessment of seismic risk in the Tooele and Rush Valleys, Tooele County, Utah: Utah Geological Survey Special Studies 51, 33 p.

Grose, L.T., 1959, Structure and petrology of the northeast part of the Soda Mountains, San Bernardino County, California: Geological Society of America Bulletin, v. 70, p. 1509-1547.

Gutenberg, B., and Richter, C.F., 1954, Seismicity of the earth and associated phenomena: Princeton, New Jersey, Princeton University Press, 310 p.

Hanks, T.C., Buchnam, R.C., Jajoie, K.R., and Wallace, R.E., 1984, Modifications of wave-cut and faulting-controlled landforms: Journal of Geophysical Research, v. 89, no. B7, p. 5771-5790.

Hecker, S., 1993, Quaternary tectonics of Utah with emphasis on earthquake-hazard characterization: Utah Geological Survey Bulletin 127, 157 p., 2 plates.

Helm, J.M., 1995, Quaternary faulting in the Stansbury fault zone, Tooele County, Utah, in Lund, W.R., (ed.), Environmental and Engineering Geology of the Wasatch Front Region: Utah Geological Association Publication 24, p. 31-44.

Hintze, L.F., (compiler), 1988, Geologic map of Utah (scale 1:500,000): Utah Geological and Mineral Survey, Salt Lake City, Utah.

Hood, J.W., and Waddell, K.M., 1968, Hydrologic reconnaissance of Skull Valley, Tooele County, Utah: Utah Department of Natural Resources, Technical Publication No. 18, 57 p.

Jackson, M.E., 1991, Paleoseismology of Utah, volume 3 – the number and timing of Holocene Paleoseismic events on the Nephi and Levan segments, Wasatch fault zone, Utah: Utah Geological Survey Special Studies 78, 23 pp.

Johnson, J.B., and Cook, K.L., 1957, Regional gravity survey of parts of Tooele, Juab, and Millard Counties, Utah: Geophysics, v. 22, p. 48-61.

Hood, J. W., and Waddell, K.M., 1968, Hydrologic reconnaissance of Skull Valley, Tooele County, Utah: Utah Department of Natural Resources, Technical Publication No. 18, 57 p.

Keaton, J.R., Currey, D.R., and Olig, S.J., 1987, Paleoseismicity and earthquake hazards evaluation of the West Valley fault zone, Salt Lake City, Dames and Moore, Final Technical Report for U. S Geological Survey, Contract No. 14-08-0001-22048, 55 p.

Keefer, D.L., and Bodily, S.E., 1983, Three-point approximations for continuous random variables: Management Science, v. 29, p. 595-609.

Krinitzsky, E.L., 1989, Empirical earthquake ground motions for an engineering site with fault sources—Tooele Army Depot, Utah: Bulletin of the Association of Engineering Geologists, v. 26, no. 3, p. 283-308.

Kulkarni, R.B., Youngs, R.R., and Coppersmith, K.J., 1984, Assessment of confidence intervals for results of seismic hazard analysis: Proceedings of the Eighth World Conference on Earthquake Engineering, San Francisco, California, v. 1, p. 263-270.

Light, A., and Kaufman, D., 1997, Amino acid paleotemperature reconstruction and radiocarbon shoreline chronology of the Lake Bonneville Basin, USA: Geological Society of America Abstracts with Programs, v. 29, no. 6, p. A-253.

Ludwig, W.J., Nafe, J.E., and Drake, C.L., 1970, Part 1, Regional observations, in Maxwell, A.E., (ed.), New Concepts of Sea Floor Evolution: Wiley Interscience, New York, p. 53-84.

Machette, M.N., and Scott, W.E., 1988, Field trip introduction–A brief review of research on lake cycles and neotectonics of the eastern basin and range province: Utah Geological and Mineral Survey Miscellaneous Publication 88-1, p. 7-14.

Machette, M.N., 1989, Preliminary surficial geologic map of the Wasatch fault zone, eastern part of Utah Valley, Utah County, and parts of Salt Lake and Juab Counties, Utah: U.S. Geological Survey Miscellaneous Field Studies Map MF-2109, scale 1:50,000.

Machette, M.N., Personious, S.F., Nelson, A.R., Schwartz, D.P., and Lund, W.R., 1991, The Wasatch fault zone, Utah-segmentation and history of Holocene earthquakes: Journal of Structural Geology, v. 13, p. 137-149.

Mason, D.B., 1996, Earthquake magnitude potential of the Intermountain seismic belt, USA, from surface-parameter scaling of late Quaternary faults: Bulletin of the Seismological Society of America, v. 86, p. 1487-1506.

Maurer, R.E., 1970, Geology of the Cedar Mountains, Tooele County, Utah: Ph.D. dissertation, University of Utah, Salt Lake City, 184 p., plus maps.

McCalpin, J.P., and Nishenko, S.P., 1996, Holocene paleoseismicity, temporal clustering, and probabilities of future large (M>7) earthquakes on the Wasatch fault zone, Utah: Journal of Geophysical Research, v. 101, no. B3, p. 6233-6253.

Miller, A., and Rice, T., 1983, Discrete approximations to probability distributions: Management Science, v. 29, p. 352-362.

Mohapatra, G.K., and Johnson, R.A., 1998, Localization of listric faults at thrust fault ramps beneath the Great Salt Lake Basin, Utah – evidence from seismic imaging and finite element modeling: Journal of Geophysical Research, v. 103, p. 10,047-10,063.

Mohapatra, G., Petropoulos, G., and Johnson, R.A., 1993, Extension and structural evolution beneath the Great Salt Lake, Utah: Results from reflection seismic imaging (abs): EOS Transactions, v. 74, p. 412.

Moore, W.J., and Sorenson, M.L., 1979, Geologic map of the Tooele 1¡ by 2¡ Quadrangle, Utah: U.S. Geological Survey Miscellaneous Investigations Series Map I-1132, scale 1:100,000.

Morris, H.T., 1987, Preliminary geologic map of the Delta 2° quadrangle, Tooele, Juab, Millard, and Utah Counties, Utah: U.S. Geological Survey Open-File Report 87-185, 18 p., scale 1:250,000.

Mukulich, M., and Smith, R.B., 1974, Seismic reflection and aeromagnetic surveys of the Great Salt Lake, Utah: Geological Society of America Bulletin, v. 85, p. 991-1002.

National Research Council, 1988, Probabilistic seismic hazard analysis: National Academy Press, Washington, D.C., 97 p.

Olig, S.S., Youngs, R.R., and Wong, I., 1998, Preliminary probabilistic seismic hazard analysis for surface fault displacement at TA-3 Los Alamos National Laboratory: Prepared for Los Alamos National Laboratory, University of California, Los Alamos, NM.

Olig, S.S., Lund, W.R., and Black, B.D., 1994, Large mid-Holocene and late Pleistocene earthquakes on the Oquirrh fault zone, Utah: Geomorphology, v. 10, p. 285-315.

Oviatt, C.G., and Currey, D.R., 1987, Pre-Bonneville Quaternary lakes in the Bonneville basin, Utah, in Kopp, R.S., and Cohenour, R.E., (eds.), Cenozoic geology of western Utah–sites for precious metal and hydrocarbon accumulations: Utah Geological Association Publication 16, p. 257-263.

Oviatt, C.G., 1997, Lake Bonneville fluctuations and global climate change: Geology, v. 25, p. 155-158.

Oviatt, C.G., Currey, D.R., and Miller, D.M., 1990, Age and paleoclimatic significance of the Stansbury shoreline of Lake Bonneville, northeastern Great Basin: Quaternary Research, v. 33, p 291-305.

Oviatt, C.G., Currey, D.R., and Sack, D., 1992, Radiocarbon chronology of Lake Bonneville, eastern Great Basin, USA: Palaeogeography, Palaeoclimatology, Palaeoecology, v. 99, p. 225-241.

Oviatt, C.G., and Miller, D.M., 1997, New explorations along the northern shores of Lake Bonneville: Brigham Young University Geology Studies 1997, v. 42, Part II, p. 345-371.

Peacock, D.C.P., and Sanderson, D.J., 1991, Displacements, segment linkage, and relay ramps in normal fault zones: Journal of Structural Geology, v. 13, no. 6, p. 721-733.

Pechmann, J.C., Nash, W.P., Vivieros, J.J., and Smith, R.B., 1987, Slip rate and earthquake potential of the East Great Salt Lake faults, Utah (abs.): EOS Transaction, v. 68, p. 1369.

Perkins, M.E., Brown, F.H., Nash, W.P., McIntosh, W., and William, S.K., 1998, Sequence, age, and source of silicic fallout tuffs in middle to late Miocene basins of the northern basin and range province: Geological Society of America Bulletin, v. 110, no. 3, p. 344-360.

Personius, S.F., 1990, Surficial geologic map of the Brigham City segment and adjacent parts of the Weber and Collinston segments, Wasatch fault zone, Box Elder and Weber counties, Utah: Utah Geological Survey Miscellaneous Investigations Series Map I-1979, scale 1:50,000.

Pezzopane, S.K., and Dawson, T.E., 1996, Fault displacement hazard: A summary of issues and information, in Seismotectonic framework and characterization of faulting at Yucca

Mountain, Nevada: U.S. Geological Survey Administrative Report prepared for the U.S. Department of Energy, Chapter 9, 160 p.

Pierce, K.L., and Colman, S.M., 1986, Effect of height and orientation (microclimate) on geomorphic degradation rates and processes, late-glacial terrace scarps in central Idaho: Geological Society of America Bulletin, v. 97, p. 869-885.

Rigby, J.K., 1958, Geology of the Stansbury Mountains, Toole County, Utah: Utah Geological Society Guidebook 13, 168 p.

Rigby, J.K., 1958, Geology of the Stansbury Mountains, Toole County, Utah, in Guidebook to the Geology of Utah: Utah Geological Society, no. 13, 175 p.

Sabetta, F., and Pugliese, A., 1996, Estimation of response spectra and simulation of nonstationary earthquake ground motions: Bulletin of the Seismological Society of America, v. 86, p. 337-352.

Sack, D., 1993, Quaternary geologic map of Skull Valley, Tooele County, Utah: Utah Geological Survey Map 150, Scale 1:100,000.

Sadigh, K., Chang, C.-Y., Egan, J.A., Makdisi, F., and Youngs, R.R., 1997, Attenuation relationships for shallow crustal earthquakes based on California strong motion data: Seismological Research Letters, v. 68, p. 180-189.

Schwartz, D.P., 1987, Earthquakes of the Holocene: Reviews of Geophysics, v. 25, p. 1197-1202.

Senior Seismic Hazard Analysis Committee (SSHAC), 1997, Recommendations for probabilistic seismic hazard analysis – Guidance on uncertainty and use of experts: U.S. Nuclear Regulatory Commission (NRC) NUREG/CR-6372, Washington, D.C.

Shackleton, N.J., and Opdyke, N.D., 1973, Oxygen isotope and paleomagnetic stratigraphy of equatorial Pacific core V28-238–Oxygen isotope temperatures and ice volumes on a 10^5 year and 10^6 year scale: Quaternary Research, v. 3, p. 39-55.

Smith, R.B., and Arabasz, W.J., 1991, Seismicity in the Intermountain Seismic Belt, in Slemmons, D.B., Engdahl, E.R., Zoback, M.D., and Blackwell, D.D., (eds.), Neotectonics of North America: Geological Society of America, Decade Map Volume 1, Boulder, Colorado, p. 185-228.

Smith, R.B., and Bruhn, R.L., 1984, Intraplate extensional tectonics of the eastern Basin-Range; inferences on structural style from seismic reflection data, regional tectonics, and thermal-mechanical models of brittle/ductile deformation: Journal of Geophysical Research, v. 89, p. 5733-5762.

Smith, R.B., Richins, W.D., and Doser, D.I., 1985, The 1983 Borah Peak, Idaho earthquake - regional seismicity, kinematics of faulting, and tectonic mechanism: Proceedings of

Workshop XXVIII on the Borah Peak, Idaho, Earthquake, v. A, U.S. Geological Survey Open-File Report 85-290, p. 236-263.

Solomon, B.J., 1993, Quaternary geologic maps of Tooele Valley and the West Desert Hazardous Industry Area, Tooele County, Utah: Utah Geological Survey Open-File Report 296, 48 p. 1:24,000 scale.

Spudich, P., Fletcher, J.B., Hellweg, M., Boatwright, J., Sullivan, C., Joyner, W.B., Hanks, T.C., Boore, D.M., McGarr, A., Baker, L.M., and Lindh, A.G., 1997, SEA96 – a new predictive relation for earthquake ground motions in extensional tectonic regimes: Seismological Research Letters, v. 68, p. 190-198.

Stepp, J.C., 1972, Analysis of completeness of the earthquake sample in the Puget Sound area an its effect on statistical estimates of earthquake hazard: Proceedings of the International Conference on Microzonation, v. 2, p. 897-910.

Stone & Webster Engineering Corporation (SWEC), 1997, SAR Chapter 2 – Site characteristics (with Appendices); submitted to Nuclear Regulatory Commission, June 25, 1997.

Suppe, J., 1983, Geometry and kinematics of fault-bend folding: American Journal of Science, v. 283, p. 684-721.

Swan, F.H., III, Schwartz, D.P., and Cluff, L.S., 1980, Recurrence of moderate to large magnitude earthquakes produced by surface faulting on the Wasatch Fault Zone, Utah: Bulletin of the Seismological Society of America, v. 70, no. 5, p. 1431-1462.

Teichert, J.A., 1959, Geology of the southern Stansbury range, Tooele County, Utah: Utah Geological and Mineral Society, Bulletin 65, May.

Tocher, D., 1958, Earthquake energy and ground breakage: Bulletin of the Seismological Society of America, v. 48, no. 2, p. 147-153.

Todd, V.R., 1983, Late Miocene displacement of Pre-Tertiary and Tertiary rocks in the Matline Mountains, northwestern Utah: Geological Society of America Memoir 157, p. 239.

Tooker, E.W., and Roberts, R.J., 1971, Structures related to thrust faults in the Stansbury Mountains, Utah: U.S. Geological Survey Professional Paper 750-B, p. B1-B12.

Topping, D.J., 1993, Paleogeographic reconstruction of the Death Valley extended region– Evidence from Miocene large rock-avalanche deposits in the Amargosa Chaos Basin, California: Geological Society of America Bulletin, v. 105, p. 1190-1213.

U.S. Department of Energy (USDOE), 1997, Topical report YMP/TR-002-NP – Methodology to assess fault displacement and vibratory ground motion hazards at Yucca Mountain, Revision 1: Civilian Radioactive Waste Management System Management and Operating Contractor.

Viveiros, J.J., 1986, Cenozoic tectonics of the Great Salt Lake from seismic reflection data: M.S. thesis, University of Utah, Salt Lake City, Utah, 81 p.

Weichert, D.H., 1980, Estimation of the earthquake recurrence parameters for unequal observation periods for different magnitudes: Bulletin of the Seismological Society of America, v. 70, p. 1337-1346.

Wells, D.L., and Coppersmith, K.J., 1993, Likelihood of surface rupture as a function of magnitude (abs.): Seismological Research Letters, v. 64, no. 1 p. 54.

Wells, D.W., and Coppersmith, K.J., 1994, New empirical relationships among magnitude, rupture length, rupture width, rupture area, and surface displacement, Bulletin of the Seismological Society of America, v. 84, p. 974-1002.

Wesnousky, S.G., 1986, Earthquakes, Quaternary faults, and seismic hazards in California: Journal of Geophysical Research, v. 91, no. B12, p. 12,587-12,631.

Wong, I., Olig, S., Green, R., Moriwaki, Y., Abrahamson, N., Baures, D., Silva, W., Somerville, P., Davidson, D., Pilz, J., and Dunne, B., 1995, Seismic hazard evaluation of the Magna tailings impoundment: Environmental and Engineering Geology of the Wasatch Front Region, Utah Geological Association Publication 24, p. 95-110.

Woodward, N.B., Boyer, S.B., and Suppe, J., 1989, Balanced geological cross-sections: an essential technique in geological research and exploration: American Geophysical Union Short Course in Geology, v. 6, 132 p.

Youngs, R.R., and Coppersmith, K.J., 1985, Implications of fault slip rates and earthquake recurrence models for probabilistic seismic hazard estimates: Bulletin of the Seismological Society of America, v. 75, p. 939-964.

Youngs, R.R., Swan, F.H., III, Power, M.P., Schwartz, D. P., and Green, R.K., 1987, Analysis of earthquake ground shaking hazard along the Wasatch Front, Utah: in Gori, P.L., and Hays, W.W. (eds.), Assessment of regional earthquake hazards and risk along the Wasatch Front, Utah, volume II: U.S. Geological Survey Open-File Report 87-585, p. M-1-110.

Zoback, M.L., 1983, Structure and cenozoic tectonism along the Wasatch fault zone, Utah; in Miller D.M., Todd, V.R., and Howard, K.A., (eds.), Tectonic and Stratigraphic Studies in the Eastern Great Basin: Geological Society of America Memoir 157, p. 3-37.

ERRATA[*]

OMISSIONS

References

Abrahamson, N.A., and Silva, W.J., 1997, Empirical response spectral attenuation relations for shallow crustal earthquakes: Seismological Research Letters, v. 68, p. 94-127.

Anderson, J.G., and Hough, S.E., 1984, A model for the shape of the Fourier amplitude spectrum of acceleration at high frequencies: Bulletin of the Seismological Society of America, v. 74, p. 1969-1994.

Bender, B., 1984, Seismic hazard estimation using a finite fault rupture model: Bulletin of the Seismological Society of America, v. 74, p. 1899-1923.

Boore, D.M., 1983, Stochastic simulation of high-frequency ground motions based on seismological models of the radiated spectra: Bulletin of the Seismological Society of America, v. 73, p. 1865-1894.

Boore, D.M., 1986, Short period P- and S-wave radiation from large earthquakes: Implications for spectral scaling relations: Bulletin of the Seismological Society of America, v. 76, p. 43-64.

Geosphere Midwest, 1997, Seismic survey of the Private Fuel Storage Facility, Skull Valley, Utah: report prepared for Stone & Webster Engineering Corporation.

Hanks, T.C., 1979, b values and ω^{-2} seismic source models: Implications for tectonic stress variations along active crustal fault zones and the estimation of high-frequency strong ground motion: Journal of Geophysical Research, V. 84, p. 2235-2242.

Hanks, T.C., and McGuire, R.K., 1981, The character of high frequency strong ground motion: Bulletin of the Seismological Society of America, v. 71, p. 2071-2095.

Magistrale, H., H. Kanamori, and C. Jones, 1992, Forward and inverse three-dimensional P-wave velocity models of the southern California crust: Journal of Geophysical Research, v. 97, p. 14,115-14, 135.

Schnabel, P.B., J. Lysmer, and H.B. Seed, 1972, SHAKE: a computer program for earthquake response analysis of horizontally layered sites: Earthquake Engineering Research Institute, University of California, Berkeley, Report EERC 72-12.

Silva, W., 1986, Soil response to earthquake ground motion: Report prepared for the Electric Power Research Institute, Research Project RP2556-07, September.

Silva, W.J. and R.B. Darragh, 1996, Engineering characterization of strong ground motion recorded at rock sites: Report submitted to the Electric Power Research Institute, EPRI RP 2556-48.

---

[*] Specific text revisions appear in bold print.

Silva, W.C., Abrahamson, N., Toro, G., and Costantino, C., 1998, Description and validation of the stochastic ground motion model: Report submitted to Brookhaven National Laboratory, Associated Universities, Inc., New York.

Singh, S., and Herrmann, R.B., 1983, Regionalization of crustal coda Q in the continental U.S.: Journal of Geophysical Research, v. 88, p. 527-538.

Tinsley, J.C., King, K.W., Trumm, D.A., Carver, D.L., and Williams, R., 1991, Geologic aspects of shear-wave velocity and relative ground response in the Salt Lake Valley, Utah: Proceedings of the 27th Symposium on Engineering Geology and Geotechnical Engineering, p. 25-1-9.

Wald, D.J., D.V. Helmberger, and R.H. Heaton, 1991, Rupture model of the 1989 Loma Prieta earthquake from the inversion of strong-motion and broadband teleseismic data: Bulletin of the Seismological Society of America, v. 81, p. 1540-1572.

Williams, R.A., King, K.W., and Tinsley, J.C., 1993, Site response estimates in Salt Lake Valley, Utah, from borehole seismic velocities: Bulletin of the Seismological Society of America, v. 83, p. 862-889.

Wong, I., and Silva, W.J., 1993, Site-specific strong ground motion estimates for the Salt Lake Valley, Utah: Utah Geological Survey Miscellaneous Publication 93-9, 34 p.

Figures

Figure 6-6, pp. 2 & 3	Maximum magnitude distributions for fault sources.
Figure 6-9, p. 2	Comparison of horizontal motion attenuation relationships used in the hazard analysis.
Figure 6-10, p. 1	Comparison of vertical motion attenuation relationships used in the hazard analysis.

REVISIONS

Text Revisions

Page 3, paragraph 1 — line 4 should read: "...sources that might affect the site. The hazard results are in the form..." (change "effect" to "affect")

Line 9 should read: "...attenuation, including earthquake source, wave propagation path, and side effects; and (3) the..." (change "pate" to "path")

Page 5, Section 1.1.1 — Line 5 – insert "Dr. Donald Currey (Limneotectonics Laboratory, University of Utah); before "Ms. Jennifer M. Helm (currently employed by AGRA Earth & Environmental, Inc.); ..."

Page 19, Section 2.3.2   Add following sentence to end of opening paragraph: "Secondary faults also are present in the block between the East and West faults. One of the more prominent of these structures, Fault "F" is shown on the northern cross section (Figure 2-1) and described below."

Page 25, paragraph 2   line 4 should read: "...9 m (28 to 30 **ft**) (replace "m" with "ft")

Page 28, paragraph 3   <u>Post-Provo Eolian, Reworked Eolian, and Playa Deposits</u>
line 2: change "2.5" to "0.8"

<u>Post-Provo Sand-ramp</u>
line 4: change "faction" to "fraction"

Page 30, paragraph 3   Lines 6 & 8: change "southwest" to "southeast"

Page 31, 2nd paragraph   Line 5: change "upper" to "late" ("...considered middle to **late** Ordovician in age...)

Page 32, 1st paragraph   last sentence should read:
Many of the layers exhibit strongly developed asymmetric shear structures including shear bands, reidel shears and pinch-and-swell structures that all indicate down-to-the-**east** extensional displacement.

Page 34, Section 4.4   1st paragraph, 3rd line: change "late" to "upper"

Page 35, last paragraph   Paragraph should end as follows: "... discussed in Section 5.2.4." **New paragraph header: Nontectonic Deformation**

Page 38   last sentence (line 5): delete comma after "Although"

Page 39, Section 5.1   2nd sentence, lines 2 – 3:   At its closest location, the main scarp is 9 km **east** of the east border of the proposed PFSF site.

Page 53   line 5 should read: "...little or **no** deformation across discrete fault traces..."

Page 68, 2nd paragraph   **Stansbury Fault** section, 1st sentence: change "east" to "west"

Page 80	2nd full paragraph, line 1
	Following Pechmann **and others** (1987)...
Page 91, Section 6.4.1	3rd Paragraph, line 4
	Sentence should read: Histograms are presented for peak acceleration and spectral acceleration at a period **of** 1.0 second for mean annual frequencies of exceedance of 2×10^{-3}, 5×10^{-4}, and 10^{-4} (return periods of 500, 2,000, and 10,000 years, respectively.
Page 92	Paragraph 2, line 8 – Sentence should read:
	Similarly, Figure 6-16 shows that consideration of the West fault as an independent source or as a secondary feature **of** the **East** fault has a minimal impact on the hazard.
Page 95	1st Sentence should read: At the present time, methodologies for the probabilistic assessment of fault displacement hazard **are not as well developed as those for ground motion hazard**.
Page 96	Paragraph before Section 7.1.3
	The logic tree methodology described in Section **6** was utilized to characterize the uncertainty in the fault displacement PSHA.
Page 99	1st sentence after equation (7-5) should read: "where h is 1.0 if the site lies in the hanging wall of the rupture and 0.0 if the site lies in the foot wall,..." (change "is" to "if").
	last paragraph, line 3 – Sentence should read:
	The various methods are described below as they are applied to distributed faulting (strike "principal and").
Page 100	Section 7.1.4.1, line 3 – Sentence should read:
	The **Smith-DePolo-O'Leary (SDO)** expert team..."
	Section 7.1.4.1, 1st paragraph, last line – *MD* should read $MD_{principal}$
	Section 7.1.4.2 – delete last two sentences of 1st paragraph

Section 7.1.4.2, 2nd paragraph (last paragraph on page)
DFS refers to Doser-Fredrick-Swan expert team
SBK refers to Smith-Bruhn-Knuepfer expert team

Page 101

Section 7.2, 3rd paragraph, last sentence should read:
These weights represent the average across the six Yucca Mountain **Seismic** Source
Characterization Expert Teams.

Page 104

2nd full paragraph (**Average Slip Rate**), line 9
Based on these data, the slip rate is well constrained between about 0.01 mm/yr and
0.04 mm/yr, with the preferred rate in the range of **0.02** to **0.03** mm/yr.

Page 118

Reference: Wells, D.W., and Coppersmith, K.J... should read Wells, D.L., and
Coppersmith, K.J...

Page F-3

2nd full paragraph, last sentence should read:
As a result, nine alternative attenuation relationships were used to evaluate
vertical ground motions.

Modifications for Crustal Path Effects, 2nd paragraph, line 3
Delete punctuation mark after reference citation (...Boore, 1983, 1986)

Page F-4

1st paragraph, line 3
Missing parenthesis after "...hazard at the site)."

Modifications for Local Site Conditions, 1st paragraph, line 7 – Sentence should
read: These velocities are consistent with the average velocities estimated by
Bay **Geophysical Associates** (1999) of 800 ft/sec for the soil above a depth of 45
feet and 1,100 ft/sec for soil above the Tertiary boundary.

Page F-7

1st full paragraph: change "Schnable" to "Schnabel"

2nd full paragraph should read as follows:
The material damping in the rock below a depth of 50 ft was estimated using the
observed high frequency attenuation at rock site recording stations. Anderson
and Hough (1984) have show that the high frequency attenuation of ground motions
in the near surface can be modeled by the attenuation parameter κ. Silva and

Darragh (1996) indicate that κ is related to the near surface shear wave quality factor, Q_s by the expression:

Page F-9

Relative Site Response, 1st paragraph, line 10
"...velocities **on** the three-layer crustal model..."

Relative Site Response, 2nd paragraph
line 2: missing quotation mark – "So. CA crust, Set A"
line 3: delete "curves"

Page F-10

1st paragraph, line 7
"...California sites, we **use** the average relative response over all four..."

3rd paragraph, line 3
"...damping relationships (Figures F-10a and F-10b) and part **(b)** shows the effect of varying the soil velocity..."

Revised Tables

Table 6-2   Downdip Geometry for Wasatch Zone (page T-15, column 5, row 7) should read as follows:

45°W [0.33]
55°W [0.34]
65°W [0.35]

Table F-5   Page 2 of 3 - Three Crustal Layers, κ = 0.03 sec, Midrange Tertiary V_s
Column 3
(λ (%)) – values should be 2.3 (0-0.2 depth range), 1.6 (0.2-1.4 depth range), 0.9 (1.4-2.0 depth range).
Column 4
(Layer κ (sec)) - values should be 0.007 (0-0.2 depth range), 0.020 (0.2-1.4 depth range), 0.003 (1.4-2.0 depth range).

Revised Figures

Figure 1-3   Photogeologic map of site vicinity showing surficial geologic units and landforms. Registration of overlay corrected and a key to the black contact was added to EXPLANATION.

Figure 2-1   EXPLANATION – Cambrian strata, undivided: change "∈q" to "∈"

Paleozoic unconformity in hanging wall of West fault should be at top Dsd as shown on rest of cross-section (not at top of Ocq).

Figure 2-2   EXPLANATION – Cambrian strata, undivided: change "∊q" to "∊"
Paleozoic unconformity in hanging wall of West fault should be at top Dsd as shown on rest of cross-section (not at top of Ocq).

Figure 5-3   Caption: "scrap" should be changed to "scarp."

Figure 6-14   Legend: dashed line (- - - -) should read **AS97**

Figure 6-21   Legend: dashed line (- - - -) should read **AS97**

Figure 6-23   Mean seismic hazard curves for horizontal and vertical motions for the CTB site.

Figure F-13   Figure caption should read as follows:
(a) Effect of choice of soil properties for Skull Valley soils on median relative response. Skull Valley sediment response computed using three-layer crustal model, median sediment velocity, and $\kappa = 0.03$ sec. (b) Effect of velocity of **Pleistocene** soils on relative response. Skull Valley sediment response computed using three-layer crustal model, median Tertiary velocity, $\kappa = 0.03$ sec, and Set A properties. Rock motions scaled to **M** 6.5 for both plots.